

SUPPLEMENTARY INFORMATION

An integrative ENCODE resource for cancer genomics

Preamble

The recent ENCODE data release provides a rich source of information for investigating questions both in basic biology and human disease. In large part, this wealth of information derives from the multiple genomic annotations provided across multiple cell types. An overarching objective of our study is to leverage ENCODE data to provide novel insights and resources for cancer research. We performed large-scale integration of various assays to construct a companion resource to the general encyclopedia focused on top-tier cell lines and their relevance to cancer biology. In particular, we aim to integrate ENCODE and cancer genomic data to gain a more comprehensive understanding of the non-coding elements involved in oncogenesis, their associated linkages to protein-coding genes and the background mutation rates therein, and the global regulatory nature of regulators in the context of matched tumor-normal cell lines.

In addition to providing new opportunities, however, the very richness of this data introduces considerable challenges with respect to data integration and organization. Our analyses rely on an array methodologies, the details for which are difficult to include within the main text of this paper. As such, the purpose of this Supplement is to provide a clear and organized reference to support and explain the datasets, pipelines, and analyses associated with this study. In addition to supplementary text, the supplementary figures and tables provide additional information not included in the main figures.

As reflected in the main text, our study is broadly organized into several main parts: a description of the assays, background mutation rate estimation, construction of compact annotations (for greater statistical power in identifying recurrence), linking genes to non-coding elements to produce models of “extended genes” (for identifying mutationally burdened regions), generalized and cell-type specific network analysis, the workflow for prioritizing key genomic features associated with cancer, and experimental validations. This supplement is presented in roughly a parallel fashion to the main text. It is also connected to the main text through the major results presented in the form of main text figures – captions associated with main text figures point to relevant sub-sections within this supplement. In cases where the related supplementary section wasn't obvious, we said "(see supp. sect xxx) to refer to a specific section. With the aim of presenting data and results (including software packages) in an organized way, we have written

about this study in roughly a hierarchical fashion. The main text lies at the top of this hierarchy and synthesizes everything in a broad manner. It refers to more detailed descriptions of our methods and datasets, as provided in this supplement. Raw data files, which lie at the bottom of the hierarchy (and which are hosted as online resources) form the bedrock from which our results are built.

We note that, in preparing this supplement, we adopt the conventions prescribed in the recent opinion piece by Greenbaum *et al*¹. As such, labels that correspond to sections, sub-sections, figures, tables, and data files are labeled to indicate whether these items directly parallel (||) or do not parallel (#) the main text, as well as whether these items are high-level or technical in nature (designated by “HL” and “TL”, respectively).

Part 1 of this document provides in-depth documentation of the ENCODE data that we use, along with the subsidiary steps in working with these data (including ENCODE data processing, enhancer and enhancer-target predictions, and extended gene definitions). Part 2 provides details on our recurrence analyses and background mutation rate estimation. Part 3 provides an in-depth look at how focused, compact annotations may be used to achieve greater statistical power when evaluating variant recurrence. Part 4 details our expression aggregation analyses. Part 5 is a discussion and in-depth look at our generalized and cell-type specific network analyses (including associated rewiring). Part 6 discusses our workflow for prioritizing key genomic features associated with cancer. Finally, Part 7 provides details on the EN-CODEC resource and how it may be accessed.

Table of Contents

1 S (HL, II) More details about “data summary from ENCODE”	12
1.1 S (HL, II) Summary of the cancer-related encyclopedia companion resource.....	12
1.2 S (TL, II) Detailed annotation of TFs and RBPs.....	13
1.3 S (TL, II) Matching of ENCODE cell types to major cancer types	17
1.3.1 S (HL, II) ENCODE data is suitable for cancer analysis	17
1.3.2 S (HL, II) Rationale for matching cell types.....	18
1.3.3 S (TL, II) Blood cancer cell line matching	20
1.3.4 S (TL, II) Breast cancer cell line matching	21
1.3.5 S (TL, II) Lung cancer cell line matching.....	22
1.4 S (TL, ‡) Normal to tumor cell line matching using replication timing data	23
1.5 S (TL, II) Summary of data from each experimental assay from ENCODE	23
1.5.1 S (TL, II) Collection of RNA-seq data	24
1.5.2 S (TL, II) Preprocessing of Repli-seq data	24
1.5.3 S (TL, II) Deduplication of ChIP-seq data	25
1.5.4 S (TL, II) External data.....	25
1.5.5 S (TL, II) Expression data from external Cohort.....	26
1.5.6 S (TL, ‡) WGS data.....	26
2 S (TL, II) More details about “ENCODE data allows more accurate BMR estimation”	27
2.1 S (TL, II) Variant calling	27
2.1.1 S (TL, II) Liver Germline and somatic variant calling.....	27
2.2 S (TL, II) Local context effect significantly affect local mutation rate.....	28
2.3 S (TL, II) Local mutation rates are highly correlated with many genomic features	29
2.4 S (TL, II) Background mutation rate estimation and P-value calculation.....	32
2.4.1 S (HL, ‡) Covariate data collection	33
2.4.2 S (TL, ‡) Covariate table creation	34
2.5 S (TL, ‡) PCA analysis of the covariate matrix	35
2.6 S (TL, ‡) Training model details	37
2.7 S (HL, ‡) Testing details	40
2.8 S (TL, ‡) BMR estimation using unmatched data	43

3 S (TL, II) More details about “A focused, compact annotation increases power for detecting cancer drivers” and “An extended gene annotation by linking non-coding elements to genes”	44
3.1 S (TL, II) Power analysis	44
3.1.1 S (TL, II) Power of individual burden test	44
3.1.2 S (TL, II) Power of multiple burden tests	45
3.2 S (TL, ‡) An stepwise screening method to predict enhancers and their gene linkages	46
3.2.1 S (TL, ‡) Enhancer prediction Pipeline based on <u>C</u> hrom <u>A</u> tin <u>S</u> hape <u>P</u> att <u>E</u> rn <u>R</u> ecognizer (CASPER)	48
3.2.2 S (TL, ‡) Enhancer prediction by <u>E</u> nhancer <u>S</u> <u>P</u> ea <u>k</u> <u>C</u> alling <u>P</u> ip <u>E</u> line from STARR-seq (ESCAPE)	50
3.2.3 S (TL, ‡) Enhancer Target prediction	56
3.3 S (TL, II) Extended gene neighborhood generation	60
3.4 S (TL, ‡) P-value summaries	60
4 S (TL, II) More details about “Interpreting tumor expression profiles using ENCODE networks identifies key regulators”	63
4.1 S (TL, ‡) Expression pattern of TF and RBPs across cancer types	63
4.2 S (TL, ‡) TCGA expression data processing.....	64
4.3 S (TL, ‡) Probabilistic Regulatory network construction from ChIPSeq and eCLIP data	64
5 S (TL,II) More details about “Cell-type specific regulatory networks highlight extensive rewiring events during oncogenesis”	70
5.1 S (TL, ‡) Regulatory network	70
5.1.1 S (TL, ‡) TF network	70
5.1.2 S (TL, ‡) RBP network.....	70
5.2 S (TL, ‡) Reconcile with the main ENCODE encyclopedia.....	70
5.3 S (TL, II) Rewiring analysis based on direct counts	71
5.3.1 S (HL, II) TF-gene linkage	71
5.3.2 S (HL, II) Full regulatory network, merged network, and network rewiring	72
5.3.3 S (TL, II) Rewiring score	72
5.3.4 S (TL, II) Clustering of rewired TFs.....	74

5.4 S (TL, II) Rewiring analysis based on mixed membership algorithm.....	75
5.5 S (TL, II) Rewiring analysis associated with H1-hESC	77
5.6 S (TL, II) Rewiring of TF across tumor types.....	78
5.7 S (TL, II) Patient survival analysis based on TF activities.....	80
5.7.1 S (TL, II) Systematic survival analysis of TFs on AML cohorts	80
5.7.2 S (HL, II) TF specific survival analysis	81
5.7.3 S (TL, II) Survival analysis of MYC in breast cancer cohort:	82
5.7.4 S (TL, II) Association of MYC and patient severity in chronic myeloid leukemia	85
5.8 S (TL, II) Target gene analysis.....	86
5.9 S (TL, ‡) Co-binding analysis	86
6 S (TL, II) More details about “Step-wise prioritization scheme pinpoints deleterious SNVs in cancer” and “Small-scale validation experiments on prioritized genomic elements and variants”	89
6.1 S (TL, ‡) Motif analysis using MotifTools (D-score)	89
6.2 S (TL, II) Experiment Details about SNV validation	92
6.3 S (TL, II) Details about siRNA RNA-Seq experiments	94
7 S (TL, ‡) EN-CODEC resource accessibility	95
7.1 S (TL, ‡) Data Provision.....	96
7.1.1 S (TL, ‡) Deduplicated ENCODE assays	96
7.1.2 S (TL, ‡) Variant calls of liver cancer patients	97
7.1.3 S (TL, ‡) Normalized cancer patient expression data.....	97
7.2 S (TL, ‡) Annotation.....	97
7.2.1 S (TL, ‡) ENCODE cancer annotations	97
7.2.2 S (TL, ‡) TF and RBP annotations	97
7.2.3 S (TL, ‡) Extended Gene	97
7.3 S (TL, ‡) Processed Data (Analysis).....	98
7.3.1 S (TL, ‡) Cis-regulatory element related	98
7.3.2 S (TL, ‡) BMR related	100
7.3.3 S (TL, ‡) Network related	101
7.3.4 S (TL, ‡) TF & RBP regulatory score in multiple cancer types	102

7.3.5 S (TL, †) Network rewiring and rewiring index	102
7.4 S (TL, †) Experimental Validation	103
7.4.1 S (TL, †) Luciferase assay related	103
7.4.2 S (TL, †) MYC knockdown experiments.....	103
7.5 S (TL, †) Code Release	104

Supplementary Figures

Figure S 1-2 (TL,) Summary of RBP annotation.....	17
Figure S 1-3 (HL,) Summary of the ENCODE cell lines	18
Figure S 1-4 (HL, ‡) Broad spectrum of ENCODE cell types	18
Figure S 1-5 (TL, ‡) Expression correlations with K562 from many other cell lines (TL, NP) ..	20
Figure S 1-6 (TL, ‡) Comparison of tumor with normal cell lines by replication timing data	23
Figure S 1-7 (HL, , shadow figure) Summary of ENCODE data for multiple cancer types	24
Figure S 1-8 (TL, ‡) Schematics of RNA-seq data processing	26
Figure S 2-1 (TL, ‡) Local context severely confounds BMR in multiple cancer types.....	28
Figure S 2-2 (TL, ‡) Violin plot of estimated BMR over local context and genomic locations ..	29
Figure S 2-3 (TL,) Example of external effects on local mutation rate	30
Figure S 2-4 (TL,) Correlation of mutation rate and external features across multiple cancer types (shadow figure for Fig. 2B)	32
Figure S 2-5 (HL,) Schematic of the recurrence analysis	33
Figure S 2-6 (TL, ‡) Heatmap of feature correlations	35
Figure S 2-7 (TL, ‡) Summary of feature PCA analysis	36
Figure S 2-8 (TL, ‡) Boxplot of Pearson correlations of top PCs to mutation counts	36
Figure S 2-9 (TL, ‡) Summary of estimated overdispersion parameter in multiple cancer types	41
Figure S 2-10 (TL, ‡) Performance of BMR model training using different number of parameters.	42
Figure S 2-11 (TL, ‡) BMR estimation with unmatched data	43
Figure S 3-1 (TL,) Power analysis of annotation length effect.....	45
Figure S 3-2 (TL,) Power analysis of annotation number.....	46

Figure S 3-3 (HL, ‡) Overall schematic of enhancer and gene linkage	47
Figure S 3-4 (TL, ‡) Integrated approach to generate high-confidence enhancers list	48
Figure S 3-5 (TL, ‡) Schematic of shape-based enhancer prediction method.....	50
Figure S 3-6 (TL, ‡) Flowchart of capture STARR-seq target region selection procedure	50
Figure S 3-7 (TL, ‡) Capture STARR-seq experiment design	52
Figure S 3-8 (TL, ‡) Schematic of ESCAPE pipeline	53
Figure S 3-9 (TL, ‡) Whole genome STARR-seq signal enrichment properties	55
Figure S 3-10 (TL, ‡) Capture STARR-seq experiment properties.....	55
Figure S 3-11 (TL, ‡) Schematic of JEME.....	59
Figure S 3-12 (HL, , shadow figure for Fig. 2 C) Schematic of extended gene definition.....	60
Figure S 3-13 (TL, ‡) Q-Q plots of P-values for CLL.....	61
Figure S 3-14 (TL, ‡) Q-Q plots of P-values for BRCA	61
Figure S 3-15 (TL, ‡) Q-Q plots of P-values for LIHC.....	62
Figure S 4-1 (TL, ‡) Expression patterns of transcription factors across cancer types	63
Figure S 4-2 (TL, ‡) Schematic of RNA-seq normalization	64
Figure S 4-3 (TL, ‡) Regulatory network construction	65
Figure S 4-4 (TL, , shadow figure for Fig. 4) Heatmap of TF activities in multiple cancer types	67
Figure S 4-5 (TL,) The potential role of ZNF687 in cancer	68
Figure S 5-1 (HL,) Network rewiring schematics.....	73
Figure S 5-2 (TL,) Kmeans clustering of rewired TFs in K562 and GM12878	74
Figure S 5-3 (TL,) Schematic of gene community based rewiring analysis.....	75
Figure S 5-4 (TL,) Example of θ distribution difference in tumor and normal cell lines.....	76

Figure S 5-5 (TL,) Comparison of rewiring direction with respect to H1-hESC	77
Figure S 5-6 (TL,) Rewiring of TF across tumor types	79
Figure S 5-7 (TL,) Survival analysis on MYC's common target genes between MCF-7 and MCF-10A.....	83
Figure S 5-8 (TL,) Survival analysis on MYC's MCF-7 specific target genes	83
Figure S 5-9 (TL,) Survival analysis on MYC's MCF-10A specific target genes	83
Figure S 5-10 (TL,) Survival analysis on MYC's target gene expression levels in three replicates	84
Figure S 5-11 (TL,) MYC activity scores were then compared between three different severity levels using ANOVA	85
Figure S 5-12 (TL, ‡) Illustration of the binding sites and their length on both TFi and TFj. Red and blue rectangles denote the binding sites of TFi and TFj, respectively. Blue shades depict the intersection of binding sites of TFi and TFj.....	86
Figure S 5-13 (TL, ‡) Co-binding scores $c(i,j)$ of the transcription factors both in GM12878 and K562 cell lines. Rows represent TFi and columns represent TFj. Red color indicates high co-binding score, where blue color indicates low co-binding scores.	87
Figure S 5-14 (TL, ‡) Difference of co-binding scores $c(i,j)$ of the transcription factors between K562 and GM12878 cell lines. Rows represent TFi and columns represent TFj. ZNF274, which has consistently higher co-binding scores with other TFs in K562 cell line compared to GM12878 is highlighted.	88
Figure S 6-1 (TL, ‡) Variant prioritization scheme based on STARR-seq	89
Figure S 6-2 (TL, ‡) Schematic of Motifool output	91
Figure S 6-3 (TL,) Schematic of SNV validation.....	93

Supplementary Tables

Table S 1-1 (TL, , shadow table for data in Fig. 1) Detailed Annotation of common TFs in K562 and GM12878	14
Table S 1-2 (TL,) Summary of cell line and cancer type matching.....	19
Table S 2-1 (TL,) List of cancer whole genome DNA sequence data obtained for variant calling	27
Table S 3-1 (TL,) Number of enhancers predicted by histone-shape based method	49
Table S 3-2 (TL, ‡) The 49 ENCODE and Roadmap Epigenomics cell lines used to construct enhancer-target networks by JEME	57
Table S 4-1 (TL, ‡) Statistics of regulatory networks.	66
Table S 4-2 (TL,) Correlation between SUB1 expression and target activity	68
Table S 5-1 (TL,) Comparison of rewired edges between K562-GM12878 network with H1-hESC	78
Table S 6-2 (TL,) Details of SNV replication technical replicate 1	93
Table S 6-3 (TL,) Details of SNV replication technical replicate 2	93
Table S 7-1 (TL, ‡) Naming convention - primary category.....	95
Table S 7-2 (TL, ‡) Naming convention - secondary category	95

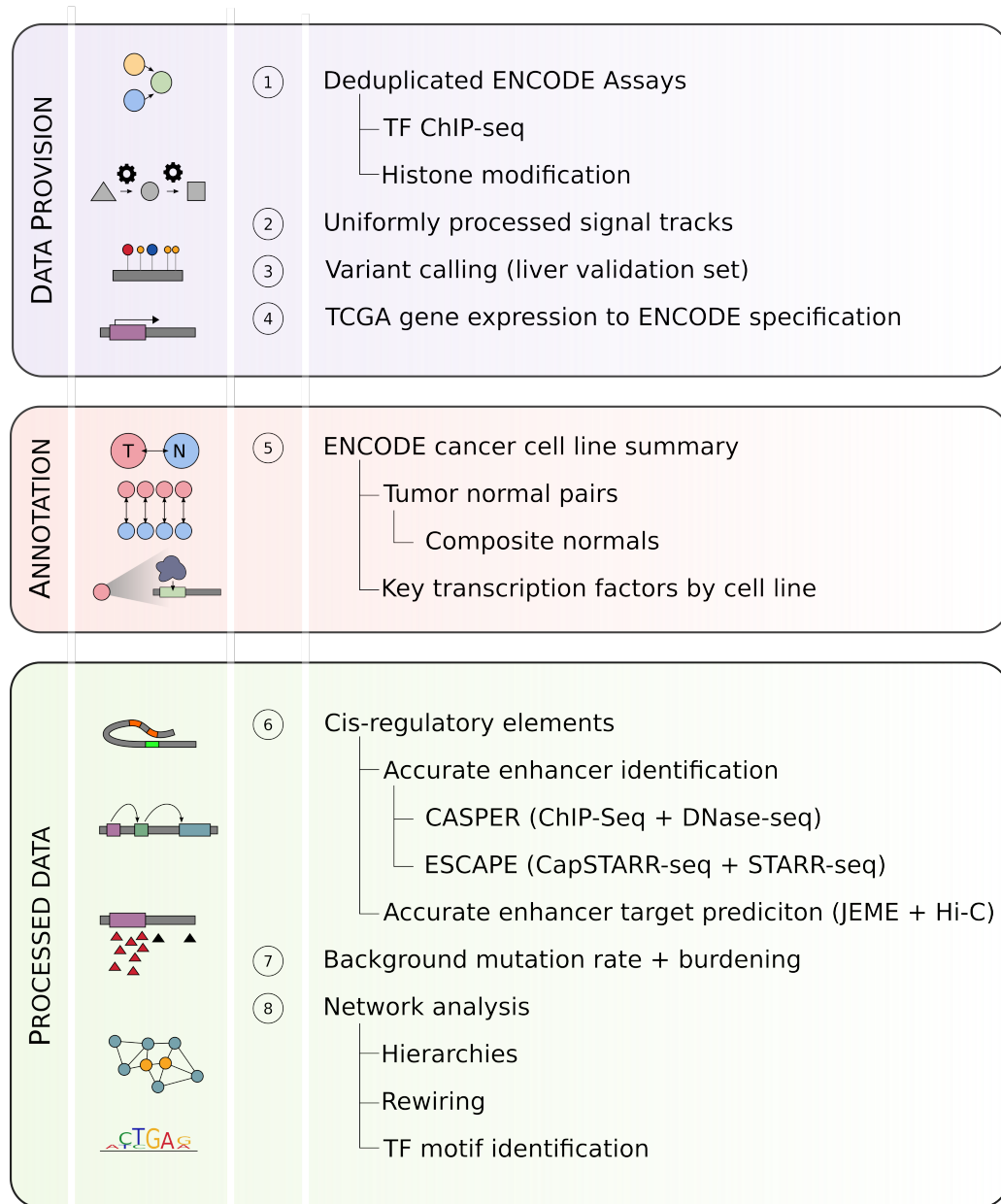
1 S (HL, ||) More details about “data summary from ENCODE”

1.1 S (HL, ||) Summary of the cancer-related encyclopedia companion resource

Mutations associated with cancer have been well characterized in many key oncogenes and tumor suppressors. However, the overwhelming bulk of mutations in cancer genomes – particularly those discovered from the recent large-scale cancer genomics initiatives – lie within non-coding regions. Whether these mutations drive cancer development or progression, or simply emerge as byproducts of genomic instability remains an open question. Newly-released data from the ENCODE Consortium can help to address this question by providing a comprehensive characterization of non-coding genomic elements, as well as by linking such elements to well-known cancer associated genes.

Here, we endeavor to provide a resource to the main ENCODE encyclopedia by building an “ENCODE Cancer-related encyclopedia companion” resource (EN-CODEC). The main encyclopedia is oriented toward the breath of the annotations to describe elements over thousands of cell types. In contrast, we focus on top cell types with a wide variety of profiles available. Most of these cell types are associated with cancers of the blood, liver, lung, cervix, and breast. We show that these cell types can be used to provide a better understanding of oncogenesis, and we provide a resource for interpreting the wealth of mutational and transcriptional profiles produced by the cancer community. We summarize our efforts in Figure S 1-1. This encyclopedia companion mainly provides three layers of resources: 1) Data provision: carefully collected and de-duplicated signal tracks from various experimental assays both within and outside ENCODE; 2) pairing cell types and datasets to cancer types; 3) Detailed Annotations: enhancers and their gene linkages, cell-type specific and generalized networks, network hierarchies, rewiring status, gene expression regulating potentials, predicted mutation rates, and motif identifications.

Figure S 1-1 (HL, ||) Summary of the resources in cancer related encyclopedia companion



1.2 S (TL, ||) Detailed annotation of TFs and RBPs

In this study, we collected a total of 344 transcription-related factors and abbreviated them all as TFs in the main text for simplicity. For our main analyses, we further classified them into four major classes: 282 sequence-specific TFs, which bind DNA at particular motifs to regulate gene

expression; 16 general TFs, which comprise that segment of the cell's transcriptional machinery that complexes with DNA; 19 chromatin-associated TFs, which comprise complexes that bind to and remodel chromatin; and 27 co-factors, which support the function of other TFs, do not directly bind DNA, and do not belong to another class. A detailed classification was given in the supplementary datasheet, which is also available from our main data portal (<http://encodec.encodeproject.org/>).

We further extracted 68 common TFs between K562 and GM12878, annotated in Table S 1-1. We searched the COSMIC Cancer Gene census² and an authoritative list of cancer genes by Vogelstein *et al.* to identify TFs associated with cancer³. We further listed whether a TF has been reported to regulate the ABL gene or BCR-ABL transcript, or the BCR-ABL KEGG pathway⁴, because of the dominant role this fusion gene plays in CML and K562^{5,6}.

Table S 1-1 (TL, ||, shadow table for data in Fig. 1) Detailed Annotation of common TFs in K562 and GM12878

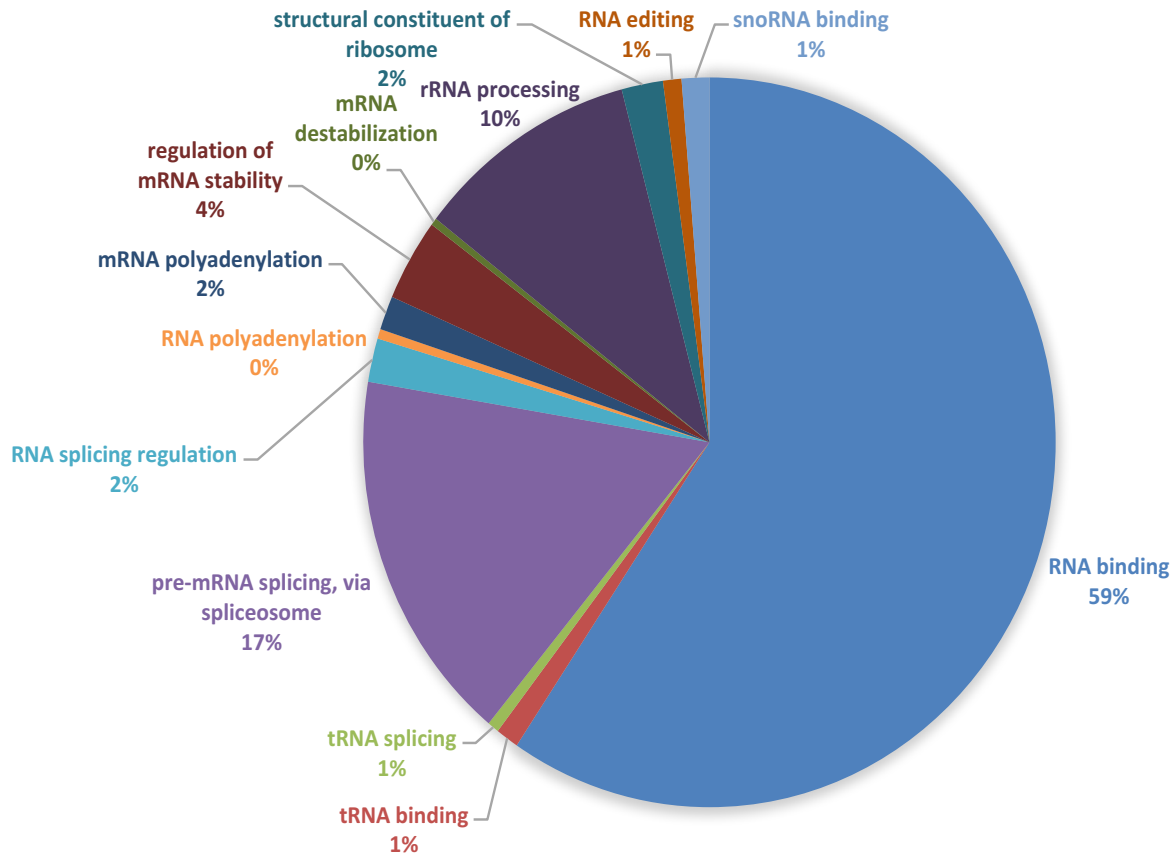
TF	Class	FAMILY	COSMIC	Vogelstein	ABL*	BCR-ABL Pathway*	Vogelstein*
ATF3	TFSS	bZIP	0	0	1	1	1
BCLAF1	TFSS	bZIP	0	0	0	1	1
BHLHE40	TFSS	HLH	0	0	0	0	0
CBX5	chromatin		0	0	0	0	0
CEBPB	TFSS	bZIP	0	0	0	1	1
CEBPZ	TFSS	bZIP	0	0	0	0	0
CHD1	chromatin	Homeodomain	0	0	0	0	0
CHD2	chromatin	Homeodomain	0	0	0	0	0
CTCF	TFSS	ZNF	1	0	0	1	1
E2F4	TFSS	wHTH	0	0	0	1	1
EGR1	TFSS	ZNF	0	0	0	1	1
ELF1	TFSS	ETS	0	0	0	1	1
ELK1	TFSS	ETS	0	0	0	0	0
EP300	general		1	1	1	1	1
ETS1	TFSS	ETS	0	0	0	1	1
ETV6	TFSS	ETS	1	0	0	0	0
EZH2	chromatin		1	1	0	0	0
FOS	TFSS	bZIP	0	0	0	1	1

GABPA	TFSS	ETS	0	0	0	0	0
HDGF	TFSS		0	0	0	0	0
IKZF1	TFSS	ZF-C2H2	1	0	0	0	0
JUNB	TFSS	bZIP	0	0	0	0	0
JUND	TFSS	bZIP	0	0	0	1	1
MAFK	TFSS	bZIP	0	0	1	1	1
MAX	TFSS	HLH	1	0	0	1	1
MAZ	TFSS	HLH	0	0	0	0	0
MEF2A	TFSS	MADs-box	0	0	0	0	0
MLLT1	TFSS		1	0	0	0	0
MTA2	TFSS	ZF-GATA	0	0	0	0	0
MXI1	TFSS	HLH	0	0	0	1	0
MYC	TFSS	HLH	1	0	0	1	1
NBN	TFSS		1	0	0	0	0
NFE2	TFSS	bZIP	0	0	0	1	0
NFYA	TFSS	CBF-NFY	0	0	0	1	1
NFYB	TFSS	CBF-NFY	0	0	0	1	1
NR2C2	TFSS	NR	0	0	1	1	1
NRF1	TFSS	bZIP	0	0	1	1	1
PML	cofactor		1	0	0	0	0
POLR2A	general		0	0	0	0	0
POLR3G	general		0	0	0	0	0
RAD21	chromatin		1	0	1	1	1
RCOR1	TFSS	MYB	0	0	0	0	0
REST	TFSS	ZNF	0	0	0	1	1
RFX5	TFSS	wHTH	0	0	0	0	1
SIN3A	general		0	0	0	1	1
SIX5	TFSS	Homeodomain	0	0	0	1	1
SMAD5	TFSS	MH1	0	0	0	0	0
SMC3	chromatin		0	0	1	1	1
SP1	TFSS	ZNF	0	0	0	1	1
SPI1	TFSS	ETS	0	0	0	1	1
SRF	TFSS	MADs-box	0	0	0	1	1
STAT5A	TFSS	STAT	0	0	0	0	0
SUZ12	chromatin	ZNF	1	0	0	1	1
TAF1	general		0	0	0	1	1
TARDBP	TFSS		0	0	0	0	0
TBL1XR1	cofactor		1	0	0	0	0
TBP	general		0	0	0	0	1
UBTF	TFSS	HMG	0	0	0	0	0

USF1	TFSS	HLH	0	0	0	1	1
USF2	TFSS	HLH	0	0	1	1	1
YBX1	TFSS	CSD	0	0	0	0	0
YY1	TFSS	ZNF	0	0	0	1	1
ZBED1	TFSS	ZNF	0	0	0	0	0
ZBTB33	TFSS	ZNF	0	0	1	1	1
ZBTB40	TFSS	ZNF	0	0	0	0	0
ZNF143	TFSS	ZNF	0	0	0	0	0
ZNF274	TFSS	ZNF	0	0	1	1	1

To provide functional annotation of the RBPs included in our study, we used gene ontology (GO) categorizations from the Gene Ontology Consortium. Using the Amigo2 webserver (amigo.geneontology.org/goose), we selected 17 GO categories representing major functional categories of RBP function, and overlapped these with the list of RBPs generated by the ENCODE project. Our chosen functional categories correspond to RNA binding (GO:0003723), tRNA binding and splicing (GO:0000049 and GO:0006388), RNA splicing (GO:0043484 and GO:0000398), RNA polyadenylation (GO:0043631, GO:0006378, and GO:1900363), regulation of RNA stability (GO:0043488 and GO:0061157), rRNA processing/ribosome (GO:0006364 and GO:0003735), RNA editing (GO:0009451), and snoRNA binding (GO:0030515). Of the ~1000 ENCODE annotated RBPs, 553 are listed as "RNA binding" by GO, and 327 have at least one specific functional annotation that involves RNA binding. A summary of the RBP annotations have been listed in Figure S 1-2.

Figure S 1-2 (TL, ||) Summary of RBP annotation



1.3 S (TL, ||) Matching of ENCODE cell types to major cancer types

1.3.1 S (HL, ||) ENCODE data is suitable for cancer analysis

Of all the cell lines in ENCODE, we found around 70 percent of them to be cancerous (shown in Figure S 1-3). Many of the cell types are quite enriched with various experimental assays for functional characterization, leaving the ENCODE data quite suitable for cancer research (Figure S 1-4).

Figure S 1-3 (HL, ||) Summary of the ENCODE cell lines

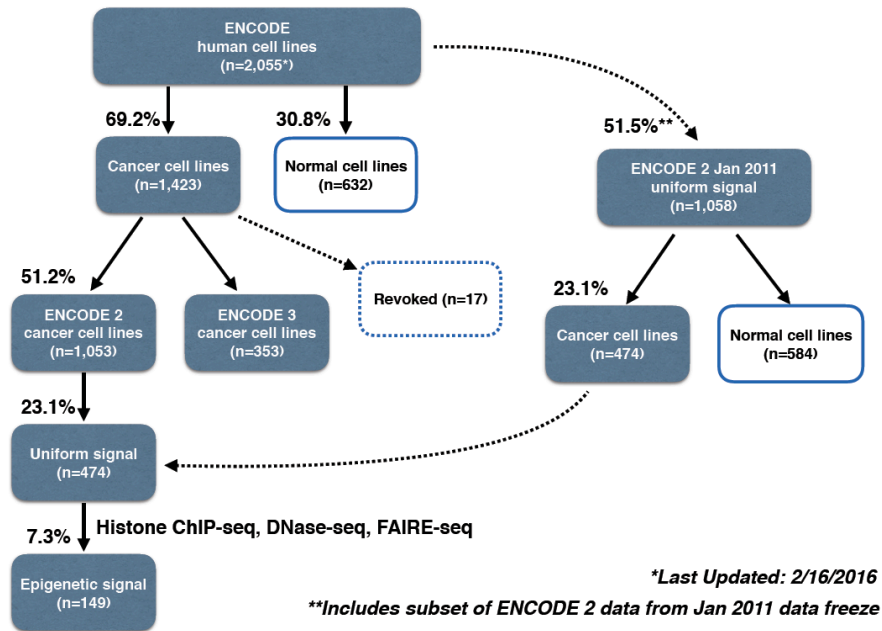
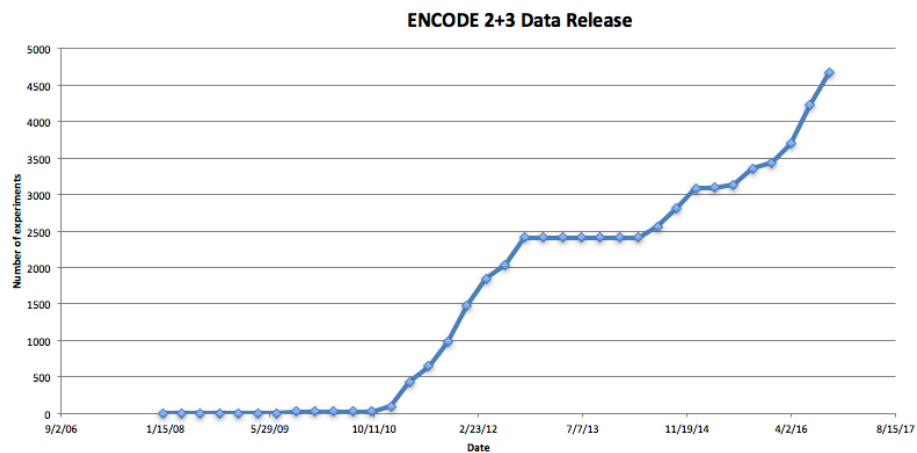


Figure S 1-4 (HL, †) Broad spectrum of ENCODE cell types



1.3.2 S (HL, ||) Rationale for matching cell types

Although wide-ranging functional characterization assays are available through ENCODE, applying this data to cancer research remains challenging. Biological heterogeneity among cancer types requires that cell types studied in cancer research be optimally matched to a particular cancer

of interest. However, well-matched tumor-normal pairs are only available for certain cancer types from among ENCODE cell types, and most cell types lack data from one or more key experimental assays (as shown in Fig 1). Therefore, it is necessary to create biologically relevant tumor-normal pairs and to develop algorithms to learn from sub-optimally matched data. Another challenge arises from the heterogeneous nature of raw data collected from experimental assays. Data must undergo de-duplication, unified processing, and proper normalization before accurate large-scale integration can be achieved. Here we endeavor to provide ENCODE data matched according to cancer type, and with appropriate tumor-normal pairs, for several high-incidence cancer types. A detailed matching summary is provided in Table S 1-2.

To utilize extensive collection of advanced ENCODE assays on several “key cell types”, one can perform an approximate matching of cancerous cells to normal cells. For the normal cells, we could simply combine a collection of normal proxies to form a composite normal. In this way, we can maximize the functional coverages of approximately matched normal while minimizing artifacts by diluting unwanted cell type specific noises.

A key feature of the ENCODE annotation is that it includes data from a great diversity of functional assays. Because it is not currently possible to perform such a wide variety of assays on tissue from individual cancer patients, we believe that this matching provides a unique opportunity to refine our understanding of the cancer genome, using large-scale data integration.

Table S 1-2 (TL, ll) Summary of cell line and cancer type matching

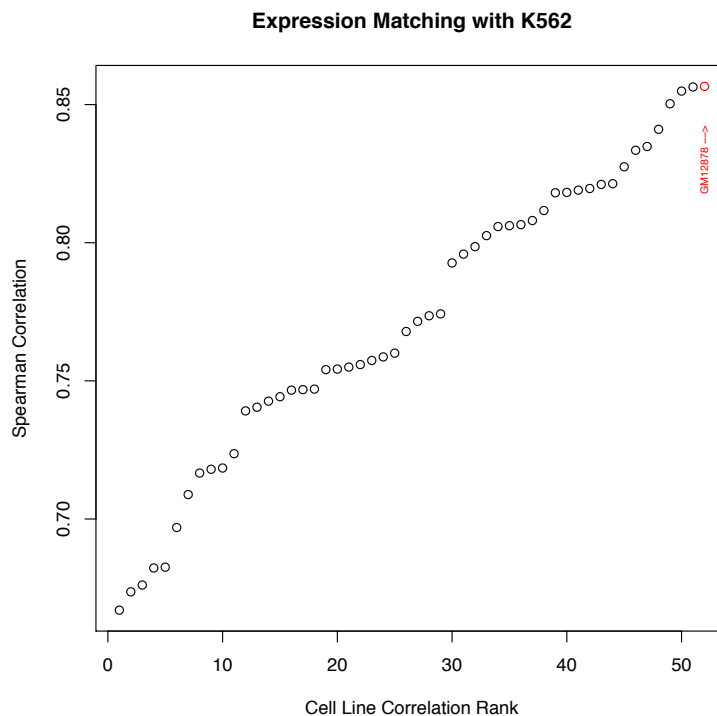
Cancer	Abbreviation	ENCODE cell line	
Breast	BRCA	Tumor	MCF-7
		Normal	HMEC, MCF-10A
Liver	LIHC	Tumor	HepG2
		Normal	Adult liver tissue
Lung	LUAD [SARC]	Adenocarcinoma	A549
		Sarcoma	SK-N-MC
		Normal	Lung tissue, IMR-90
Blood	CML [CLL/LAML]	Tumor	K562, DND-41
		Normal	CD34+ common myeloid progenitor cell, GM12878
Cervix	CESC	Tumor	HeLa-S3
		Normal	N/A

Colorectal	COAD+READ	Adenocarcinoma	Caco-2, HCT116
Prostate	PRAD	Adenocarcinoma	LNCaP, PC-3
Pancreas	PAAD	Adenocarcinoma	Panc1

1.3.3 S (TL, ||) Blood cancer cell line matching

Wherever possible, we have matched each ENCODE cancer cell type with a composite normal, which was derived from multiple of normal samples with the same cell type of origin. Exact matching was not possible with K562: this cancer cell-line derives from a myeloid lineage, but there is no data-rich noncancerous myeloid cell included in ENCODE. GM12878 is a data-rich ENCODE cell-line derived from the closely related lymphoid lineage. Supporting this choice, we determined that among all non-cancerous cell-lines provided by Roadmap Epigenome and GTEX, GM12878 has the highest Spearman correlation with K562, as shown in in Figure S 1-5. Hence, we used GM12878 as a *rough* pair for K562.

Figure S 1-5 (TL, ‡) Expression correlations with K562 from many other cell lines (TL, NP)



In addition, we found CD34+ common myeloid progenitor cells to be another close normal proxy to K562. Common myeloid progenitor cells are a direct ancestor of many differentiated myeloid cells including granulocytes and monocytes, and therefore it can directly related to chronic myeloid leukemia. However, there is a limited range of data assays with CD34+ common myeloid progenitor cell, and therefore we merged them with data-rich GM12878 assays to build a composite normal.

1.3.4 S (TL, ||) Breast cancer cell line matching

MCF-7 is the most studied human breast cancer cell line, with nearly 25,000 scientific publications reporting results from studies of MCF-7⁷. It is a human cell line derived from a malignant pleural effusion due to breast carcinoma⁸. MCF-7 is one of few cell lines that express substantial levels of estrogen receptor (ER), and so is widely used to mimic ER-positive invasive human breast cancers. It is also used to study intracellular binding constants, transport mechanisms, and DNA binding sites among ER target genes.⁷ T47D is also an ER-positive breast cancer cell line that has been widely used to study breast cancer, and is also derived from a malignant pleural effusion⁹. Unlike MCF-7, T47D is a mutant for the tumor suppressor gene TP53¹⁰.

MCF-10A is the human breast epithelial cell line most commonly used as an *in vitro* model for studying normal breast cell function and transformation¹¹. It was derived from spontaneously immortalized benign fibrocystic mammary tissue, which is non-tumorigenic and does not express ER^{11,12}. Numerous studies have utilized both MCF-7 and MCF-10A cell lines to facilitate the development of breast cancer treatment and therapy, by comparing the differential response of these two cell lines under multiple experimental settings¹³⁻¹⁵.

A recent study challenges MCF-10A as a representative model for normal mammary cells, with the study authors claiming that this cell line exhibits phenotypes and expression profiles that have not been observed in mammary gland tissues¹¹. However, these authors caution a need for further investigation into the appropriateness of MCF-10A cells as a model for normal human mammary epithelial cells. Though we cannot exclude differences between MCF-7 and MCF-10A from causes unrelated to malignant transformation, given the wealth of ENCODE data on MCF-7, and the high incidence of breast cancer, we consider the pairing of MCF-7 and MCF-10A worthwhile.

Human mammary epithelial cells (HMEC) is another representative model for normal mammary cells and numerous studies have used them for matching normal against MCF-7¹⁶⁻¹⁸. HMEC is also widely used outside ENCODE and we were able to obtain external data such as Hi-C, from literature search (GSM1551613).

1.3.5 S (TL, ||) Lung cancer cell line matching

A549 is a carcinomic lung epithelial cell line¹⁹ and IMR-90 is a normal lung fibroblast cell line²⁰. Lung fibroblasts and lung epithelial cells are closely related cell types, and conversion between these cell types is common and meaningful in tumor cells and normal cells^{21,22}. Lung fibroblasts like IMR-90, are mesenchymal cells that arise in embryologic development subsequent to epithelial to mesenchymal transition (EMT). The dedifferentiation of mesenchymal cells into secondary epithelial tissue following mesenchymal to epithelial transition (MET) is also observed and is best characterized in kidney development²³. It has been postulated that the dedifferentiation and metastasis of epithelial lung cancer cells, may occur through EMT and/or MET²⁴⁻²⁷. Such a process has been observed in other cancers²². Indeed, exposure of A549 epithelial cells to chemotherapeutic agents or TGF-B, causes differentiation to a mesenchymal phenotype, and EMT is thought to play a role in chemotherapeutic resistance of lung adenocarcinoma^{28,29}. These cellular relationships support the benefit of using a tumor normal comparison between A549 cancer cells and IMR-90 normal cells. Indeed, IMR-90 is frequently used as a normal control for A549 in experiment³⁰⁻³⁶.

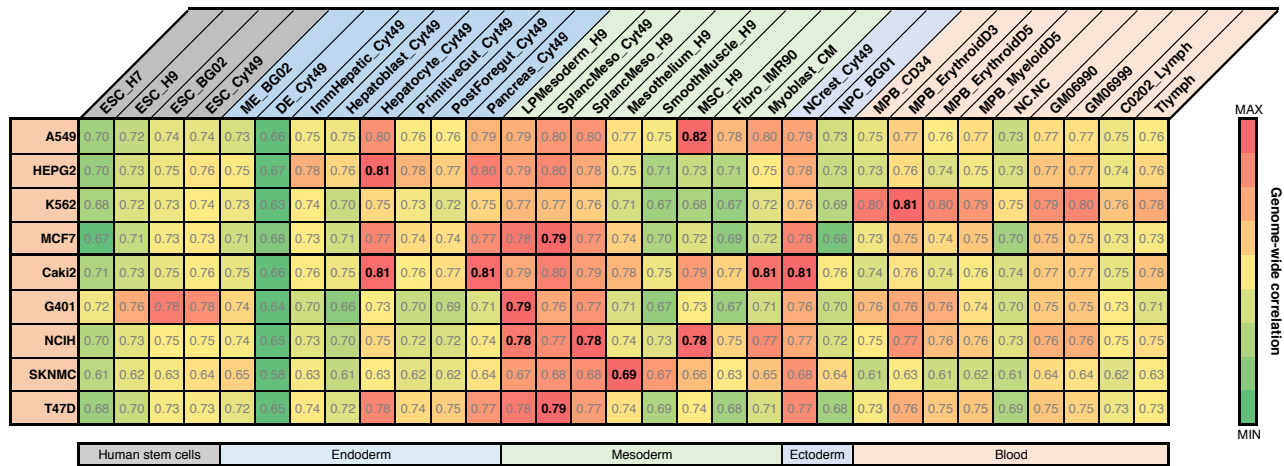
ENCODE contains a wide range of data-rich assays on both fetal and adult lung tissues, including but not limited to DNase-seq, ChIP-seq, and RNA-seq. Not a single biosample can be used as a perfect match for A549, and therefore, we merged data-rich assays on normal lung biosamples from anatomical origin (IMR-90, fetal and adult lung tissue samples) or cellular origin (any normal epithelial cells) to form a composite normal.

1.4 S (TL, †) Normal to tumor cell line matching using replication timing data

It is well known that replication timing significantly affects the mutational landscape in both germline and normal cells³⁷. We also made a genome-wide correlation of replication timing data (excluding ChrX and ChrY to avoid gender differences) between the cancer cell lines and several candidate normal cell types. Results are listed in

Figure S 1-6. As expected, the best matching normal data for K562 and HepG2 cell lines are Erythroid progenitors and Hepatocytes. However, we also noticed that replication timing data in A549 and MCF-7 shows the highest correlation with those in Mesenchymal Stem cells and Splanchnic mesoderm. However, our proposed matching normal cell lines, such as like IMR-90 for A549, still showed a decent correlation regarding their replication timing profiles.

Figure S 1-6 (TL, †) Comparison of tumor with normal cell lines by replication timing data

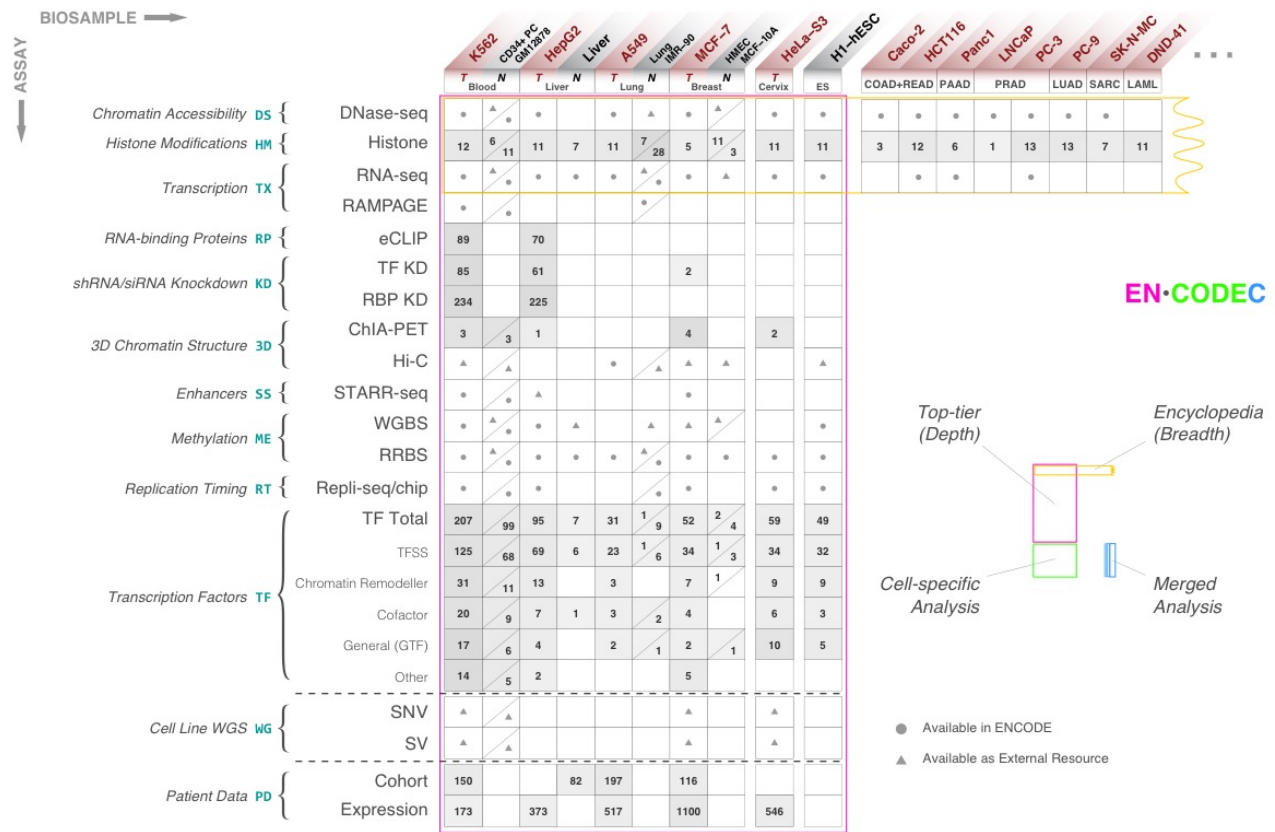


1.5 S (TL, ||) Summary of data from each experimental assay from ENCODE

We have integrated data sets from ENCODE and Roadmap Epigenomics Mapping Consortium (REMC), after performing quality control and uniform processing, to build one of the most comprehensive representations of how functional regulatory elements interplay in the human

genome. All datasets used in the analysis were mapped to a standardized version of the GRCh37 (hg19) reference human genome. We used ENCODE data that was submitted and released up to October 31st, 2016 (Oct 2016 freeze). We summarized the ENCODE data with matched tumors in Figure S 1-7.

Figure S 1-7 (HL, ||, shadow figure) Summary of ENCODE data for multiple cancer types



1.5.1 S (TL, ||) Collection of RNA-seq data

We downloaded the signal tracks of all RNA-seq experiments and counted the average signal of a fixed bin size (e.g 1mb, or 100kb). If there are multiple RNA-seq data for each cell type, we prioritize data in the following order: ENCODE3 polyA mRNA > pair-end stranded > single-end unstranded > ENCODE2 RNA-seq.

1.5.2 S (TL, ||) Preprocessing of Repli-seq data

The raw signal of 90 Repli-seq data sets for 15 different tissue or cell lines were downloaded from the ENCODE data portal ([link](#) here). For each tissue/cell line, in cell cycle phases G1, S1,

S2, S3, S4, and G2, newly replicated DNA positions were sequenced and analyzed by massive parallel sequencing were sequenced³⁸. Similar to Suzuki *et al*³⁸, we added up the signal strength in 1mb bins by comparing the (G1 + S1) with the (S4 + G2) datasets by measuring the inverse tangent (arctangent) for each data point³⁹.

1.5.3 S (TL, ||) Deduplication of ChIP-seq data

We collected **1,040** TF ChIP-seq experiments released for ENCODE. There are **888** released TF ChIP-seq experiments for ENCODE2. We used a subset of 801 experiments that either had no treatment or ethanol treatment only. There were **570** TF ChIP-seq experiments released for ENCODE3, which had no treatment.

For a common TF target in top-tier cell lines, ENCODE has multiple of the same experiments from different labs. We carefully de-duplicated the dataset by selecting one TF ChIP-seq experiment per each sample by the following prioritization scheme. When an ENCODE3 experiment was available, it was prioritized over the ENCODE2 experiment. When there was the same type of experiments done by different labs, we prioritized using the following order determined by the total number of ChIP-seq experiments deposited on ENCODE: *stanford*, *haib*, *broad*, *usc*, *uw*, *uta*, *uchicago*, *hms*, *yale*. We removed epitope-tagged experiments if an endogenous antibody was available. After deduplication, there were **860** unique TF ChIP-seq experiments.

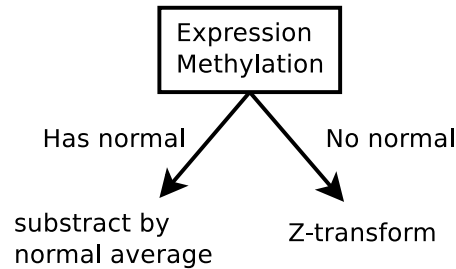
1.5.4 S (TL, ||) External data

We deeply integrated our ENCODE functional characterization data with data from external cohorts to interpret cancer genome. Specifically, we downloaded both expression and WGS data from external cohorts.

1.5.5 S (TL, ||) Expression data from external Cohort

All TCGA expression, methylation and mutation data were downloaded from GDAC firehose (<http://gdac.broadinstitute.org>) with data version of 2016_01_28. For cancer types with normal control samples profiled, the expression values of each gene are subtracted with the average value of all normal controls. For cancer types without any normal samples profiled, the expression profile of each gene is transformed to zero mean and unit deviation (see Figure S 1-8). The DNA methylation values are also normalized in the same way as RNA-seq data, according to the availability of normal control samples in each cancer type. For copy number alteration (CNA), GDAC firehose does not provide standardized data, and we downloaded the data matrix from cBioportal with data version of 2016_10_20 (<http://www.cbioportal.org>).

Figure S 1-8 (TL, #) Schemetics of RNA-seq data processing



1.5.6 S (TL, #) WGS data

2709 WGS samples were collected for 5 cancer types (BRCA, LAML, LUAD, LIHC, UCEC).

2 S (TL, ||) More details about “ENCODE data allows more accurate BMR estimation”

2.1 S (TL, ||) Variant calling

2.1.1 S (TL, ||) Liver Germline and somatic variant calling

We called germline single nucleotide variants (SNVs) for a set of 88 liver cancer samples (Table S 2-1) that were whole genome DNA sequenced at the Beijing Genomics Institute (BGI) Shenzhen for a mutation analysis published in *Genome Research*⁴⁰. The authors made the raw sequence data available in FASTQ format from the European Nucleotide Archive (ENA) under accession ERP001196. We downloaded these files and conducted a germline variant calling procedure in accordance with the Broad Institute’s Best Practices for read-to-variant workflows (<https://software.broadinstitute.org/gatk/best-practices/index.php>). Read alignments were generated using the Burrows-Wheeler Aligner (BWA v0.7.15; <http://bio-bwa.sourceforge.net/>), using the BWA-MEM algorithm. After that, we proceeded with preprocessing for variant calling, including cleaning out duplicate reads using Picard tools (MarkDuplicates tools v2.6.0), and base recalibration with the Genome Analysis Toolkit (GATK; v3.6.0). Variant calls for individual samples were derived with the GATK HaplotypeCaller, followed by joint genotyping with the GenotypeGVCFs tool. The final variant set was subjected to standard quality filtration in accordance with the standard configuration of the GATK VariantFiltration tool. Each step was performed on the Mt Sinai Minerva scientific compute cluster, and utilized hundreds of CPU cores per compute step. Table S 2-1 summarizes the distribution of germline variant calls per sample.

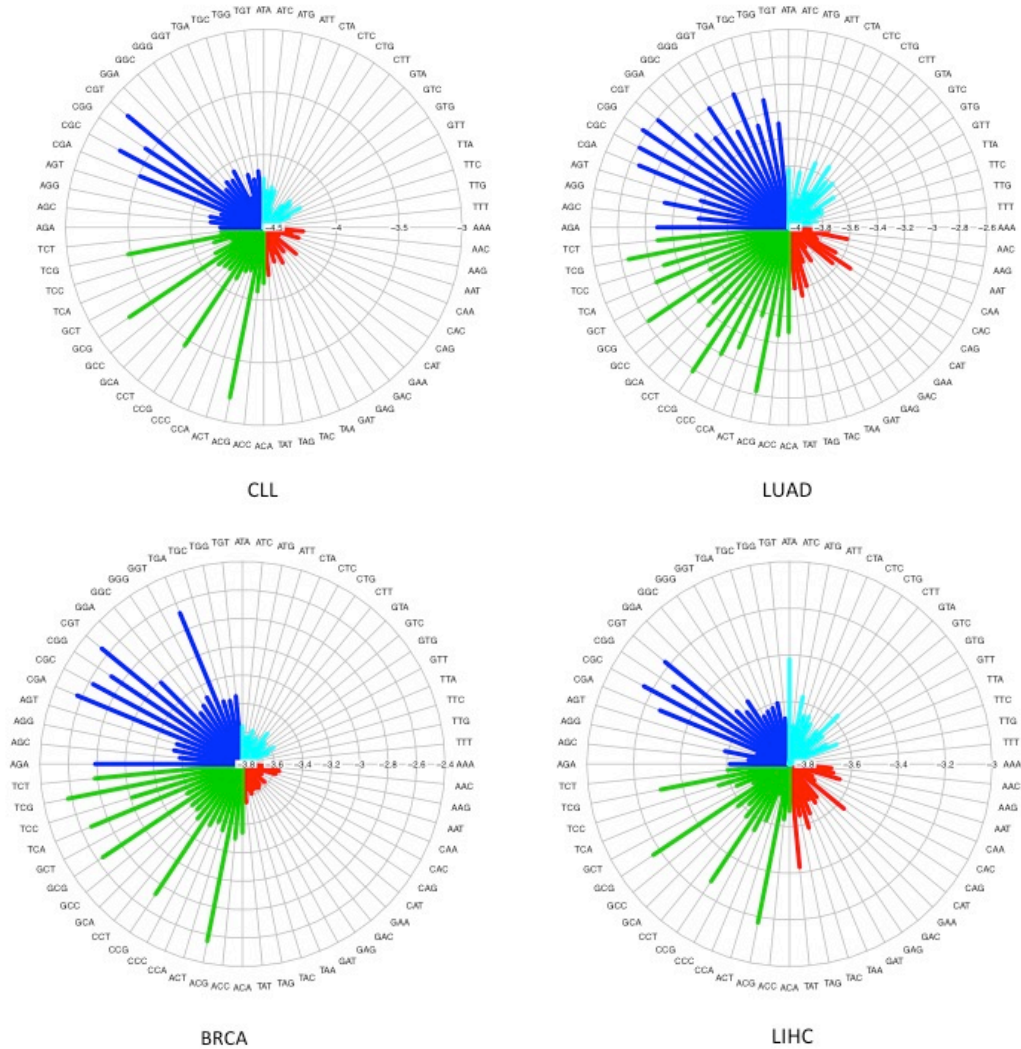
Table S 2-1 (TL, ||) List of cancer whole genome DNA sequence data obtained for variant calling

Cancer type	Number of samples	Median # of var per sample	Source
Liver - germline	88	4,156,068	BGI Shenzhen (Kan <i>et al.</i> 2013)
Liver - somatic	88	13,647	BGI Shenzhen (Kan <i>et al.</i> 2013)

2.2 S (TL, ||) Local context effect significantly affect local mutation rate

We observed that BMR is significantly associated with local context effect in all cancer types up to several orders, which largely contributes to the mutation rate heterogeneity. Details are given in Figure S 2-1. For example, the average pooled mutation rate ranges from $1.58e-04$ to $2.92e-03$ (18.35 fold). The observed mutation has been plotted in the following radial plots for each cancer type. In general, G/C positions are more prone to mutations as compared to A/T positions, but the local context effect within G/C positions still has a strong effect ($2.40e-04$ and $2.40e-04$ vs.

Figure S 2-1 (TL, ‡) Local context severely confounds BMR in multiple cancer types

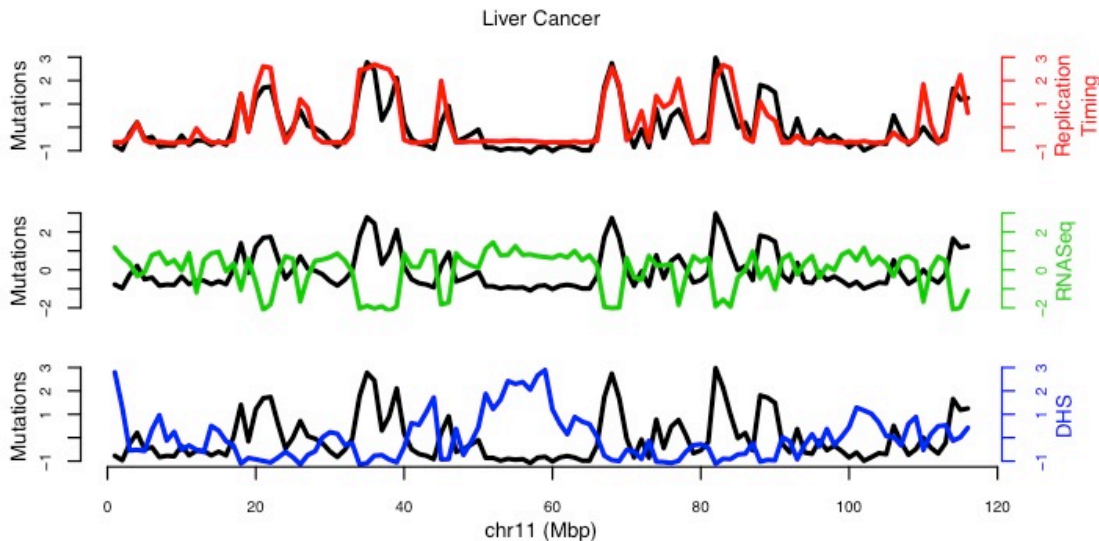


cancer types. For example, the normalized pooled mutation rates in the 1Mb bins are given in Figure S 2-3 chromosome 11. It correlated replication timing data quite well. On the contrary, it has a negative correlation with both RNA-seq and DHS signal in liver cancer. Hence, it is important to correct BMR against the confounding effects of these external genomic features.

We systematically explored the effect of multiple genomic features including replication timing, DHS, WGBS, RNA-seq and Hi-C and their correlation with the overall mutation rate in multiple cancer types is given in

Figure S 2-4. For example, in breast cancer, the correlation between replication timing and mutation rate ranges from 0.47 to 0.55, while correlation from DHS signals ranges from -0.42 to -0.18 . However, we observed an increased correlation of mutation rates to these features in liver cancer (0.59 to 0.74 for replication timing and -0.58 to -0.33 for DHS, details in Table S 2-2). Hence it is important to correct the effect of external features in a cancer specific way to achieve

Figure S 2-3 (TL, ||) Example of external effects on local mutation rate



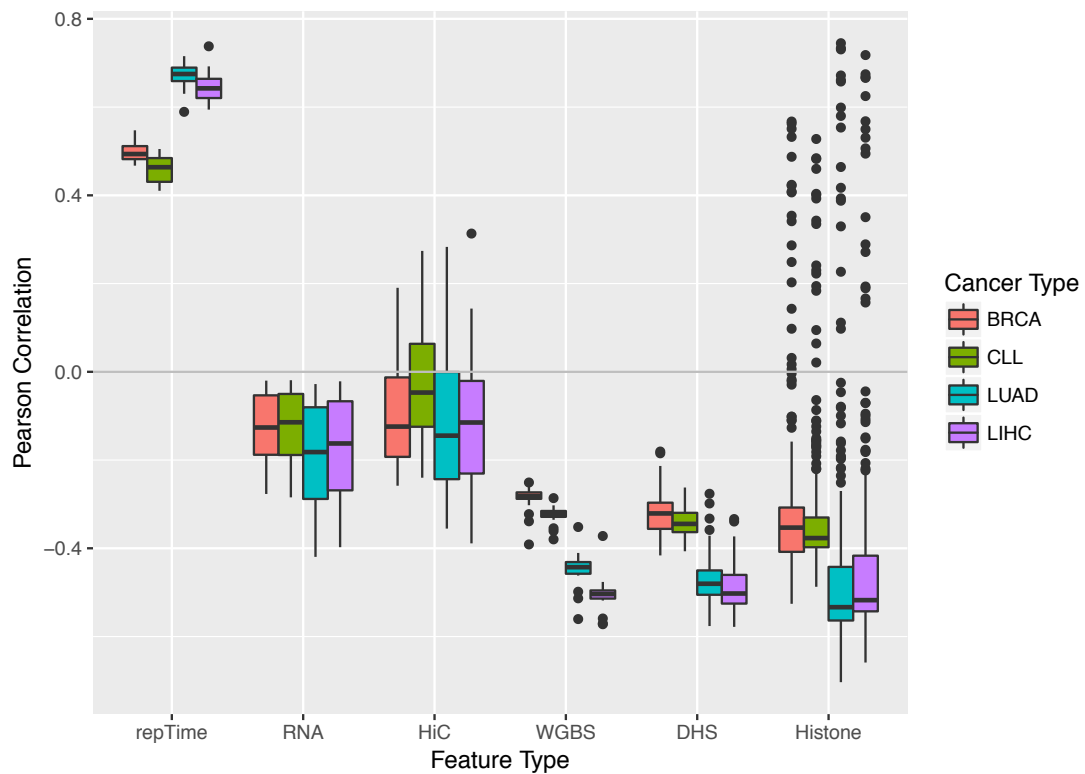
better burden analysis.

Table S 2-2 (TL, ||) Summary of correlation of mutation rate at 1mb bins with different external features in multiple cancer types

		BRCA	CLL	LUAD	LIHC
repTime	Min	0.467300058	0.410292073	0.589242196	0.594308714

repTime	Median	0.493598234	0.4637348	0.67495952	0.642464943
repTime	Max	0.547374543	0.504968332	0.715431489	0.737831334
RNA	Min	-0.276898241	-0.284573043	-0.419458551	-0.397504844
RNA	Median	-0.126228292	-0.114417754	-0.181953795	-0.162453668
RNA	Max	-0.019998871	-0.019088747	-0.027760515	-0.021616959
HiC	Min	-0.258214534	-0.240053286	-0.355389238	-0.388864195
HiC	Median	-0.124167655	-0.047070425	-0.144698057	-0.114903485
HiC	Max	0.190402416	0.274050935	0.283105375	0.31333984
WGBS	Min	-0.391201031	-0.379756186	-0.560373539	-0.572058872
WGBS	Median	-0.28162047	-0.321745409	-0.442804565	-0.503776857
WGBS	Max	-0.250846402	-0.28621958	-0.35169477	-0.37209731
DHS	Min	-0.416168532	-0.406787562	-0.576209738	-0.578067199
DHS	Median	-0.321014839	-0.344702489	-0.480339053	-0.502492181
DHS	Max	-0.180644113	-0.262259514	-0.276360875	-0.333674803
Histone	Min	-0.525809902	-0.487246457	-0.703446634	-0.658923263
Histone	Median	-0.35312576	-0.376874169	-0.533489718	-0.517573323
Histone	Max	0.567295147	0.527731502	0.74483745	0.717959133

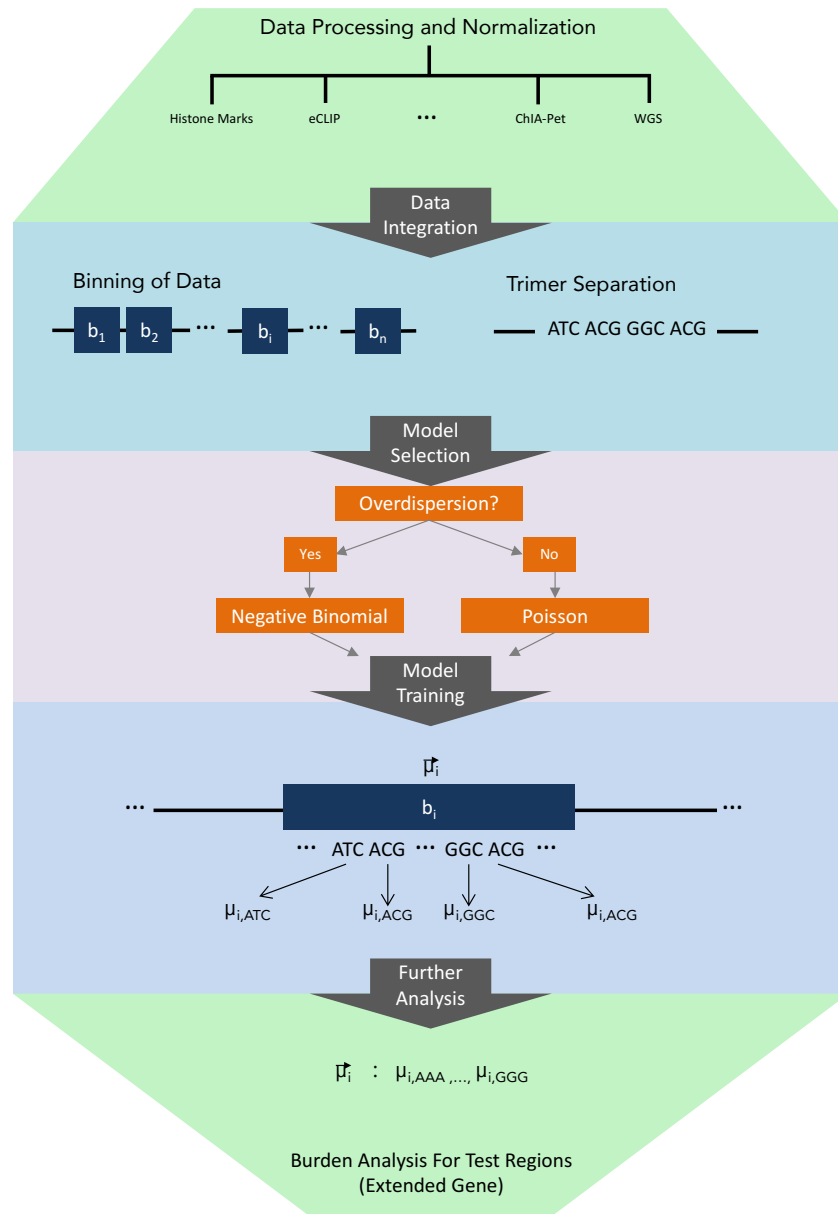
Figure S 2-4 (TL, ||) Correlation of mutation rate and external features across multiple cancer types (shadow figure for Fig. 2B)



2.4 S (TL, ||) Background mutation rate estimation and P-value calculation

Here we proposed a regression based somatic mutation recurrence analysis in cancer. The schematic of this method is shown in Figure S 2-5.

Figure S 2-5 (HL, II) Schematic of the recurrence analysis



2.4.1 S (HL, II) Covariate data collection

We collected uniformly processed and non-redundant set of confounding genomic features across different cell types from both ENCODE to build the master covariate matrix that was used

to correct for the background mutation rate (BMR). To ensure that the covariate matrix is not affected by processing bias and artifacts, we manually curated the dataset processed by the latest uniform processing pipeline and de-duplicated signal tracks from either untreated or ethanol-treated experiments. To build a covariate matrix, we then averaged the signal over specified 1Mb bin size.

2.4.2 S (TL, #) Covariate table creation

We trained our model using the master covariate matrix. Different from the calibrated training data selection mentioned in Lawrence *et al*⁴¹, we divided the whole genome into bins with fixed length, such as 1mb, 100kb, 50kb, etc. Only autosomal chromosomes and chromosome X were included in our analysis to remove the gender imbalance in mutation data or covariates.

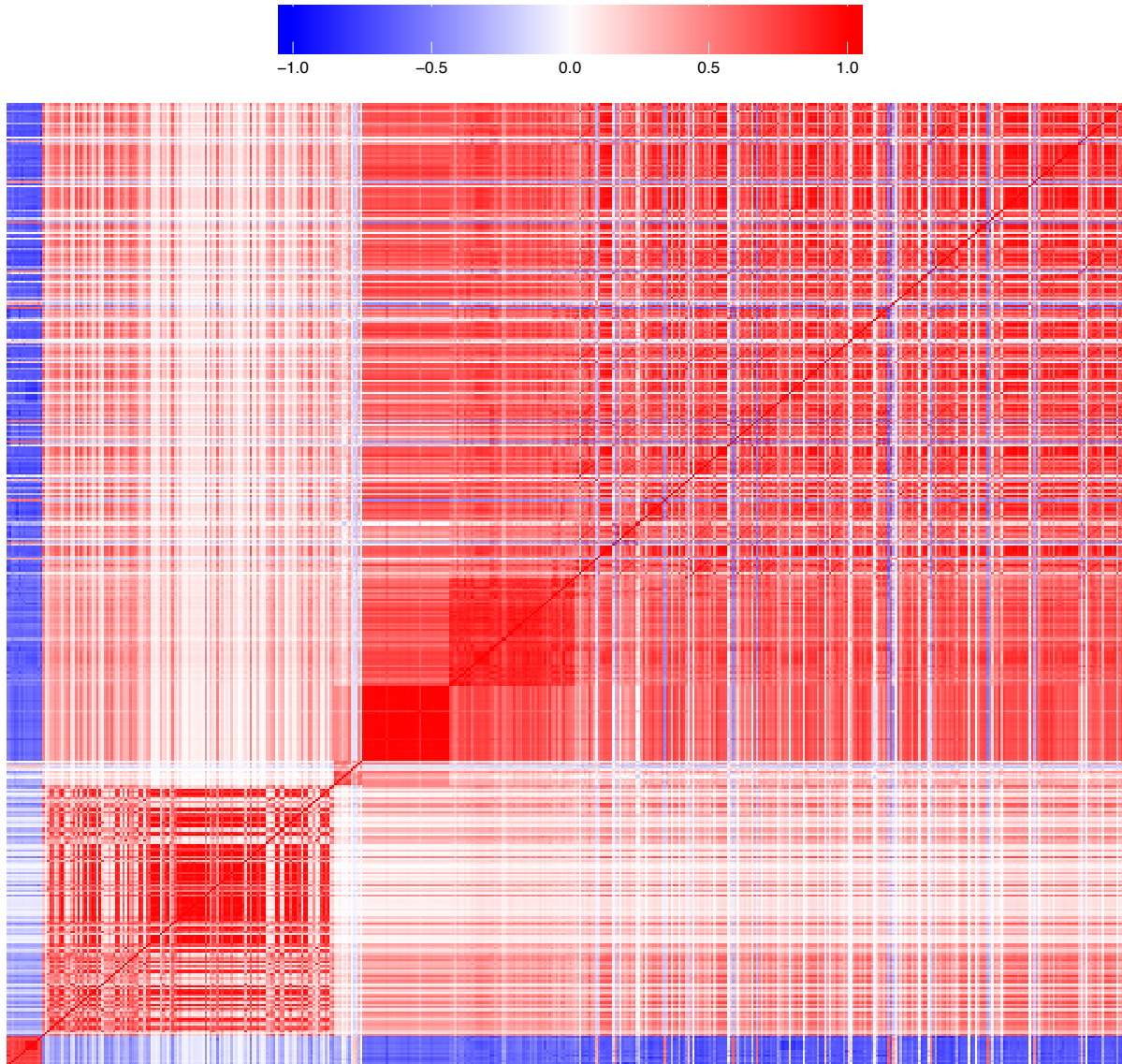
Repetitive regions on human genome are known to generate artifacts in high throughput sequencing analysis mainly due to their low mappability. We downloaded the mappability consensus excludable table used in the ENCODE project from <http://hgdownload.cse.ucsc.edu/goldenpath/hg19/encodeDCC/wgEncodeMapability/wgEncodeDacMapabilityConsensusExcludable.bed.gz>. Any fixed length bins that overlap with this table would be removed from the training process. We also downloaded the gap regions of hg19 from the UCSC genome browser, which include gaps from the telomere, short_arm, heterochromatin, contig, and scaffold. The fixed length bins that intersect with these gap regions were also removed in our analysis.

All the bigWig files generated in step one were used to calculate the average signal using the bigWigAverageOverBed tool for each fixed length bin we generated above. In the end, we summarized all the covariates values in each bin into a covariate table, with 475 columns indicating different features and rows representing different training bins.

2.5 S (TL, †) PCA analysis of the covariate matrix

It has been reported that many genomic signal tracks demonstrate noticeable correlations across features and tissues. A heatmap of the Pearson correlation of the 475 features from 229 cell types was given in Figure S 2-6. We observed strong correlations among the used features. For

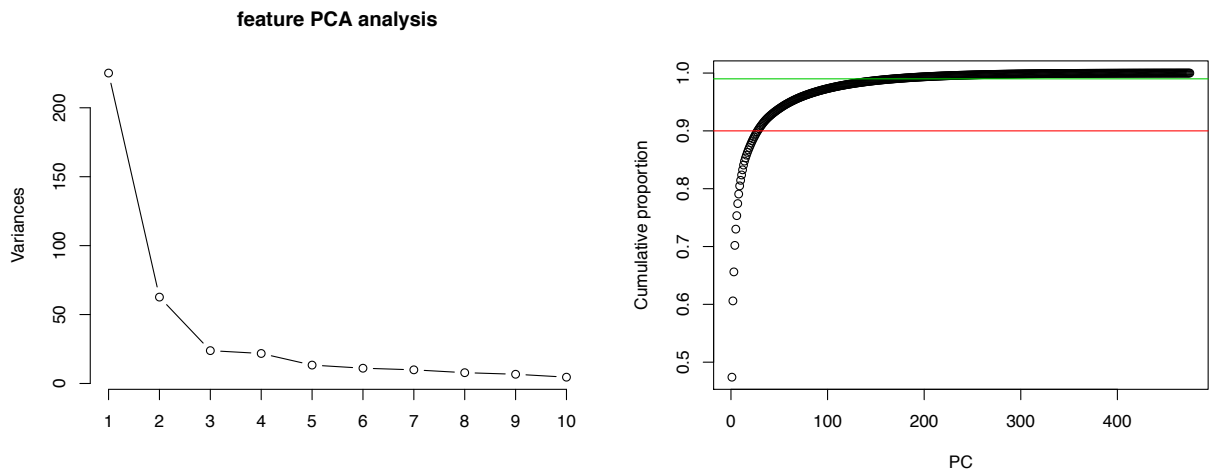
Figure S 2-6 (TL, †) Heatmap of feature correlations



example, Pearson correlation of colors ranges from -0.874 to 0.998 at the 1Mb bins.

Hence we first centered and scaled the covariate matrix X and then performed PCA on it to obtain \hat{X} . Then the cumulative proportion of variance explained by the PCs was given in Figure S 2-7. As expected, the covariate table is highly redundant, as implied by the fact that the first PC may explain as much as 47.41% of variance, and the 2nd PC explains an additional 13.19%. Nonetheless, the various data types contribute some unique information since it takes up to 28 and 169 PCs to capture 90% and 99% of variance (details in Figure S 2-7).

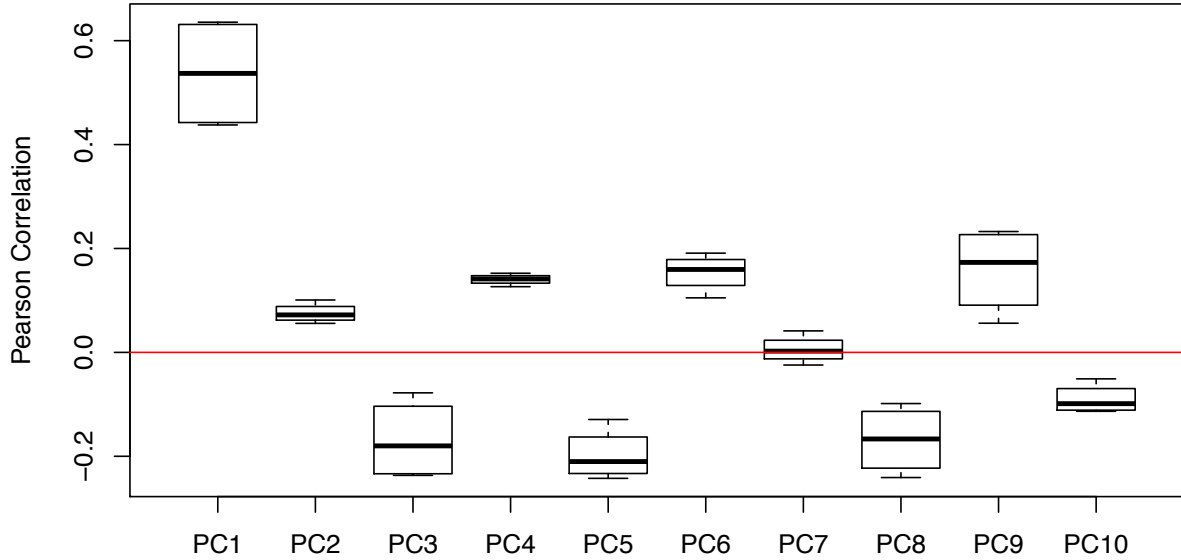
Figure S 2-7 (TL, #) Summary of feature PCA analysis



We also calculated the Pearson correlation of PC j with mutation counts in cancer type d as ρ_j^d . Then the absolute correlation value $|\rho_j^d|$ were averaged over different cancer types as $\hat{\rho}_j$ to rank the PCs. The top 10 PCs with highest $\hat{\rho}_j$ were selected and boxplot for each of the PCs was given in Figure S 2-8.

Figure S 2-8 (TL, #) Boxplot of Pearson correlations of top PCs to mutation counts

PC vs. Mutation counts per bin



2.6 S (TL, ‡) Training model details

First we divide the whole genome into bins with fixed length l . In this stage, l is usually large, such as 1 Mb. Any bins overlapping either of the two blacklist regions are removed. Then, 475 features are extracted from both REMC and ENCODE, and the average signal in the bins is calculated. We let $x_{i,j}$ denote the average signal strength for the i^{th} bin and j^{th} covariate, where $i = 1, \dots, n$ and $j = 1, \dots, m$.

Suppose there are $d = 1, \dots, D$ different diseases (or disease types) in the collected WGS data, and $s = 1, \dots, s_d$ unique samples, for example different patients, for each disease (or disease type such as liver cancer or lung cancer) d . Let $y_i^{d,s}$ and $\lambda_i^{d,s}$ denote the observed mutation count and rate for the i^{th} bin defined above for sample s in disease d . In previous efforts, scientists assume that mutation rate $\lambda_i^{d,s}$ is constant across different regions of the human genome, samples, and diseases, so they have that $\lambda_i^{d,s} \triangleq \lambda$ for $\forall i, d, s$. Hence $y_i^{d,s}$ follows a Poisson distribution with the probability mass function (PMF) given in equation (2-1).

$$P\{Y_i^{d,s} = y_i^{d,s}\} = \frac{e^{-\lambda_i^{d,s}} (\lambda_i^{d,s})^{y_i^{d,s}}}{y_i^{d,s}!} \triangleq \frac{e^{-\lambda} \lambda^{y_i^{d,s}}}{y_i^{d,s}!} \quad (2-1)$$

However, somatic genomes are highly heterogeneous because mutation rates vary considerably among various diseases, samples, and regions of the same genome, severely violating the assumption in equation (2-1). As a result, fitting of $y_i^{d,s}$ is usually very poor because overdispersion is often observed⁴². Simply assuming a constant mutation rate will generate numerous false positives. Instead, in our model we assume that different $\lambda_i^{d,s}$ are random variables that follow a Gamma distribution with probability density function (PDF)

$$P\{\lambda_i^{d,s} = x\} = \frac{1}{\Gamma(c_i^d)(v_i^d)^{c_i^d}} x^{(c_i^d-1)} e^{-\frac{x}{v_i^d}} \quad (2-2),$$

where $c_i^d > 0$ and $v_i^d > 0$. In equation (2-2), c_i^d and v_i^d are the shape and scale parameters respectively. Assume that $\lambda_i^d = \sum_{s=1}^{s_d} \lambda_i^{d,s}$ is the overall mutation rate from all samples in bin i of disease d . Its distribution can be readily obtained through convolution as

$$P\{\lambda_i^d = x\} = \frac{1}{\Gamma(s_d c_i^d)(v_i^d)^{s_d c_i^d}} x^{(s_d c_i^d-1)} \exp\left(-\frac{x}{v_i^d}\right) \quad (2-3).$$

If we let $y_i^d = \sum_{s=1}^{s_d} y_i^{d,s}$ represent the total mutation counts in region i from all disease samples, d , then the conditional distribution of y_i^d given λ_i^d can be written as

$$P(y_i^d | \lambda_i^d) = \frac{(\lambda_i^d)^{y_i^d} \exp(-\lambda_i^d)}{(y_i^d)!} \quad (2-4).$$

By integrating (2-3) into (2-4), the marginal distribution of y_i^d can be denoted as a negative binomial distribution⁴³.

$$P(y_i^d | c_i^d, v_i^d) = \left(\frac{1}{1+v_i^d}\right)^{s_d c_i^d} \frac{\Gamma(s_d c_i^d + y_i^d)}{\Gamma(s_d c_i^d)(y_i^d)!} \left(\frac{v_i^d}{1+v_i^d}\right)^{y_i^d} \quad (2-5a).$$

Equation (2-5a) is the PDF of a negative binomial distribution with $E(y_i^d) = s_d c_i^d v_i^d$ and $Var(y_i^d) = s_d c_i^d v_i^d (1 + v_i^d)$. To better interpret (2-5a), we define $v_i^d = \mu_i^d \sigma_i^d$ and $s_d c_i^d = 1/\sigma_i^d$. Then equation (2-5a) can be rewritten as (2-5b).

$$P_{Y_i^d}(y_i^d | \mu_i^d, \sigma_i^d) = \left(\frac{1}{1 + \sigma_i^d \mu_i^d} \right)^{y_i^d} \frac{\Gamma(y_i^d + 1/\sigma_i^d)}{\Gamma(1/\sigma_i^d) \Gamma(y_i^d + 1)} \left(\frac{\sigma_i^d \mu_i^d}{1 + \sigma_i^d \mu_i^d} \right)^{y_i^d} \quad (2-5b)$$

The mean and variance of y_i^d from (2-5b) can be described as μ_i^d and $\mu_i^d (1 + \mu_i^d \sigma_i^d)$ respectively. Our model in equation (2-5b) is convenient due to its explicit interpretability. First, it assumes that the individual mutation rates are heterogeneous by modeling $\lambda_i^{d,s}$ as i.i.d. Gamma distributed random variables. Unlike the constant mutation rate assumption where $Var(y_i^d) = E(y_i^d)$, our model captures the extra variance of y_i^d due to population heterogeneity. Our model in (2-5b) also clearly separates the two main parameters μ_i^d and σ_i^d with physically interpretable meanings: the mean and overdispersion, respectively. Here a larger σ_i^d indicates a more severe degree of overdispersion, which is usually due to larger differences in mutation rates.

After modeling y_i^d with a negative binomial distribution, we then estimate the local mutation rate by correcting the covariate matrix \mathbf{X} described above. Again $x_{i,j}$ denotes the average signal strength in the i^{th} bin and j^{th} covariate, where $i = 1, \dots, n$ and $j = 1, \dots, m$. Because the genomic features in the covariate matrix are highly correlated and may introduce multicollinearity if directly used in regression, we first apply principal component analysis (PCA) to matrix \mathbf{X} . We define \mathbf{X}' to be the covariate matrix after PCA and $x'_{i,j}$ as each element in \mathbf{X}' .

A generalized regression scheme is used here. Suppose g_1 and g_2 are two link functions. We then use linear combinations of covariate matrix \mathbf{X}' to predict the transformed mean parameter, μ_i^d , and overdispersion parameter, σ_i^d , as

$$\begin{aligned} g_1(\mu_i^d) &= \log(\mu_i^d) = \beta_0^d + \beta_1^d x'_{i,1} + \dots + \beta_j^d x'_{i,j} + \dots + \beta_m^d x'_{i,m} \\ g_2(\sigma_i^d) &= \log(\sigma_i^d) = \alpha_0^d + \alpha_1^d x'_{i,1} + \dots + \alpha_j^d x'_{i,j} + \dots + \alpha_m^d x'_{i,m} \end{aligned} \quad (2-6).$$

Here we use a log link function for both g_1 and g_2 , so the regression model in (6) is a negative binomial regression. Note that \mathbf{X} contains 475 genomic features in all available tissues. In the following analysis, we use all features to run the regression in (2-6) to achieve better performance. The GAMLSS package in R is used to estimate the parameters in (2-6) as $\hat{\alpha}_0^d, \dots, \hat{\alpha}_m^d, \hat{\beta}_0^d, \dots, \hat{\beta}_m^d$. Generally, there are biological reasons to explain how μ_i^d changes with covariates. For example,

single-stranded DNA in the later replicated regions usually suffers from accumulative damage resulting in larger μ_i^d . It is more difficult to interpret such a relationship with σ_i^d . Hence, we simplify equation (2-6) by assuming σ_i^d is constant in our real data analysis. In order to separate the local context effect, we separate the 64 local 3 mers to train 64×2 parameters during the training process.

2.7 S (HL, †) Testing details

Suppose there are K regions to be tested. We use the local mutation rate to evaluate the mutation burden. For the k^{th} target region ($k = 1, \dots, K$), one way of calculating the covariates is to extend it into length l (illustrative figure given in Figure S 2-5). Then we calculate the average signal for feature j as $x_{k,j}, j = 1, \dots, m$ for this extended bin, and after PCA projection let $x'_{k,j}$ represent the value for the j^{th} PC. The local mutation parameters $\hat{\mu}_k^d$ and $\hat{\sigma}_k^d$ in the extended bin for the k^{th} target region can be calculated as

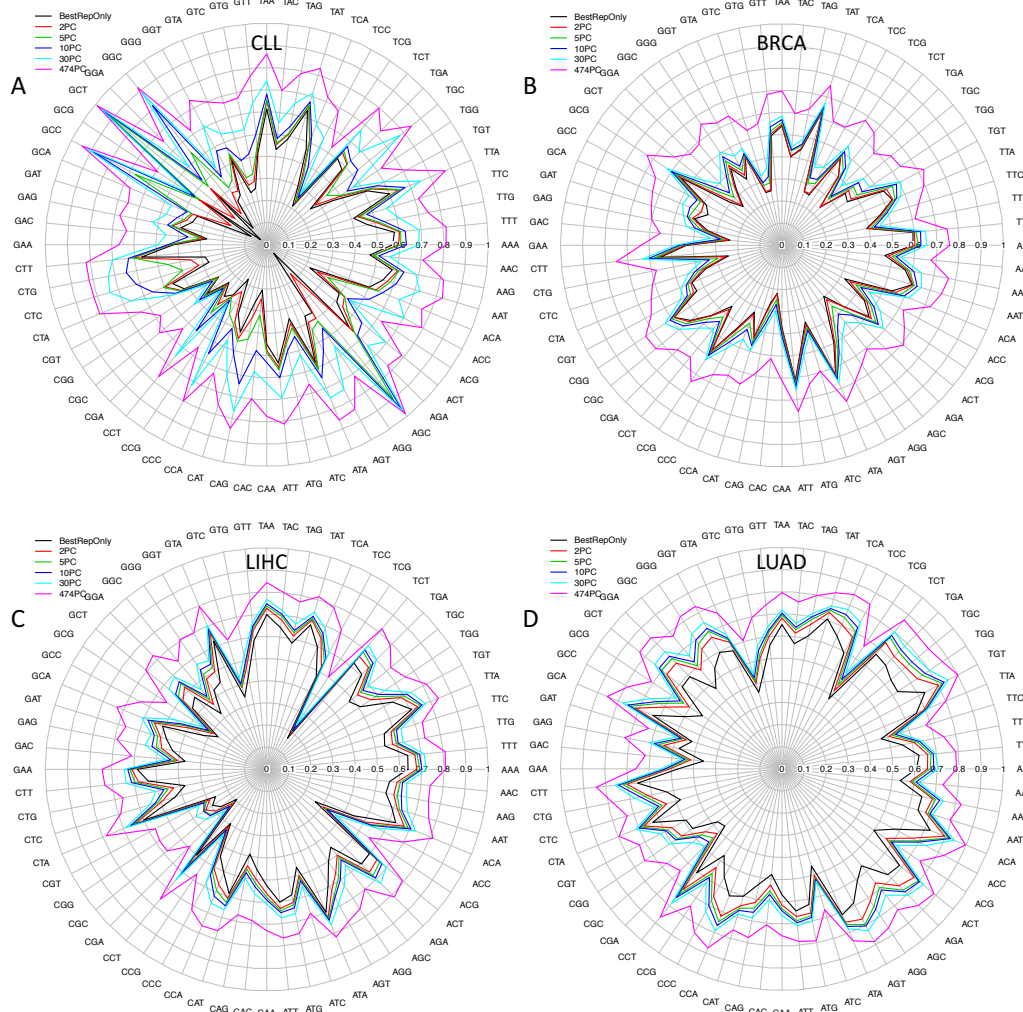
$$\begin{aligned}\hat{\mu}_k^d &= \exp\left(\hat{\beta}_0^d + \hat{\beta}_1^d x'_{k,1} + \dots + \hat{\beta}_j^d x'_{k,j} + \dots + \hat{\beta}_m^d x'_{k,m}\right) \\ \hat{\sigma}_k^d &= \exp\left(\hat{\alpha}_0^d + \hat{\alpha}_1^d x'_{k,1} + \dots + \hat{\alpha}_j^d x'_{k,j} + \dots + \hat{\alpha}_m^d x'_{k,m}\right)\end{aligned}\tag{2-7}.$$

In real data analysis, the length of the k^{th} test region l_k is much shorter than the length of the training bins (up to 1Mb). Hence $\hat{\mu}_k^d$ needs to be adjusted by a factor of l_k/l . Then $\hat{\sigma}_k^d$ and the adjusted $\hat{\mu}_k^d$ can be used to calculate the disease specific P-value, p_k^d . This above scheme is usually computationally expensive because there are typically millions of target regions to be tested. Therefore, we also propose an alternative approximation using fixed, optimized values for $\hat{\mu}_k^d$ and $\hat{\sigma}_k^d$ in our analysis. In order to separate the local context effect, we separate the 64 3-mers and run individual regression models for each 3-mer..

The negative binomial model mentioned in equation (2-5) can effectively control the false positive rate when there is large overdispersion. However, the downside for (2-5) is that when there is little heterogeneity among patients, such that heterogeneity over different regions of the genome are completely removed by regressing against the external features, then estimation in (2-7) might fail. In other words, it cannot handle the non over-dispersed data well. In order to solve this problem, we first use Poisson regression which assumes equal mean and variance. Then we

Figure S 2-10. We observed that in all cancer types, using more features significantly improves the BMR estimation precision. However, to avoid overfitting, we first run a regression using projected PCs on the feature matrix, and then all PCs with adjusted P-value greater than 0.05 are removed during the training process.

Figure S 2-10 (TL, ‡) Performance of BMR model training using different number of parameters.



Sometimes it is necessary to analyze several related diseases (or disease types) to provide a combined P-value. One typical example is in pan-cancer analysis. In the above section, we calculated the P-value for disease/disease type d as p_k^d for test region k . Fisher's method can be used to combine these P-values. Specifically, the test statistic is

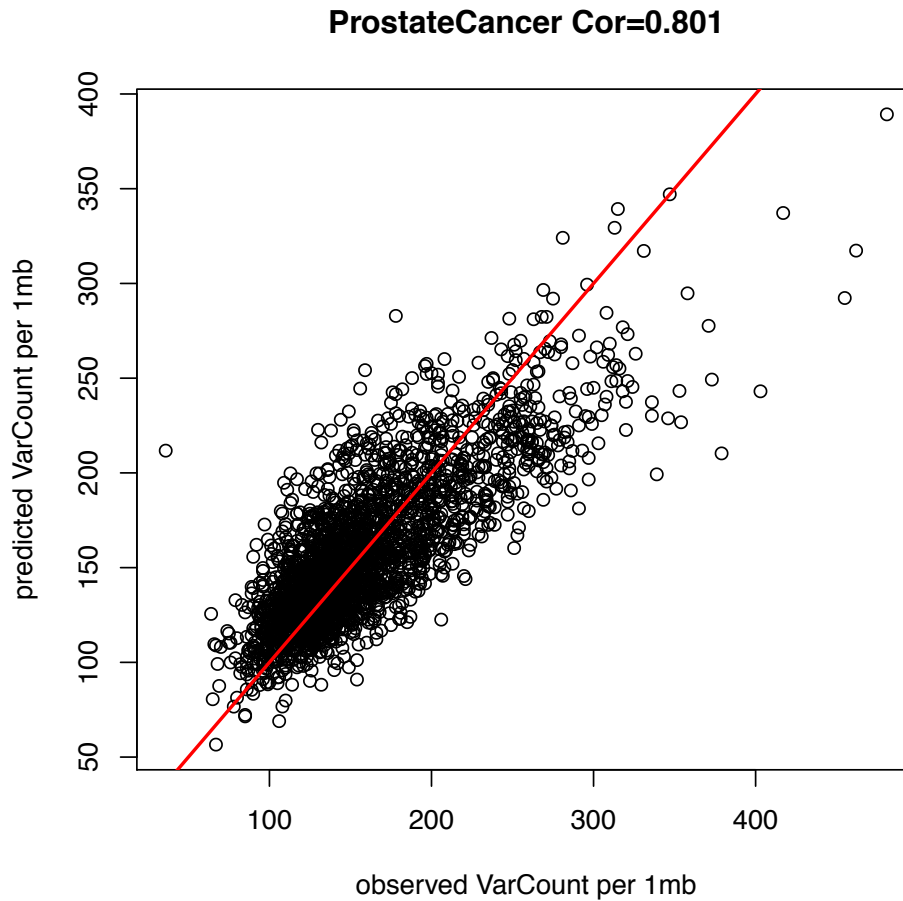
$$T_k = -2 \sum_{d=1}^D \ln(p_k^d) \sim \chi^2(2D) \quad (2-8).$$

Here T_k follows a centered chi-square distribution with $2D$ degrees of freedom, where D is the total number of diseases/disease types. The final P-value, p_k , can be calculated from T_k .

2.8 S (TL, ‡) BMR estimation using unmatched data

As shown in Figure S 2-6, features across multiple cell types are highly correlated. This characteristic enables us to estimate BMR of a potentially unmatched cancer type with acceptable accuracy. For example, ENCODE has very limited functional characteristic data for prostate cancer. However, the correlation between the observed and estimated variant counts per 1 Mb bin is as high as 0.80 from our model (Figure S 2-11).

Figure S 2-11 (TL, ‡) BMR estimation with unmatched data



3 S (TL, ||) More details about “A focused, compact annotation increases power for detecting cancer drivers” and “An extended gene annotation by linking non-coding elements to genes”

3.1 S (TL, ||) Power analysis

In this section, we discussed in detail how the annotation quality and quantity would affect the statistical power of burden analysis.

3.1.1 S (TL, ||) Power of individual burden test

Similar to the power calculation mentioned in previous papers^{45,46}, let L and μ denote the length of test region and background mutation rate for this region. The probability that there is at least one mutation can be formulated as

$$p_0 = 1 - (1 - \mu)^L \quad (3-1)$$

For the driver regions, the fraction of mutations over population is r and miss detection rate during the variant calling process is m . Then under the alternative hypothesis, the mutation rate should be

$$p_1 = p_0 + r(1 - m) \quad (3-2)$$

Suppose the total number of test regions is K , then the P value needed to claim significance would be

$$P_{thre} = \frac{0.05}{K} \quad (3-3)$$

Let N_{min} is the minimum number of samples needed under the null hypothesis that has p value at P_{thre} . Then the power can be calculated as

$$Power = P\{Bi(N_{min}, p_1)\} \quad (3-4)$$

If $\mu = 6/Mbp$, $m = 0.5$, $r = 5\%$, and $K = 25000$ (roughly the number of genes), then from the simulation in **Error! Reference source not found.**, it is obvious that longer regions needs larger number of sample to achieve similar power level. Hence it is better to maintain a minimum length of the functional regions with true functional impact.

3.1.2 S (TL, ||) Power of multiple burden tests

We also fixed the length of the annotation and checked the effect of annotation numbers on burden tests. Since a large number of annotation will introduce huge penalty due to multiple test correction, it is better to confine tests on core annotations with high confidence (**Error! Reference source not found.**).

Figure S 3-1 (TL, ||) Power analysis of annotation length effect

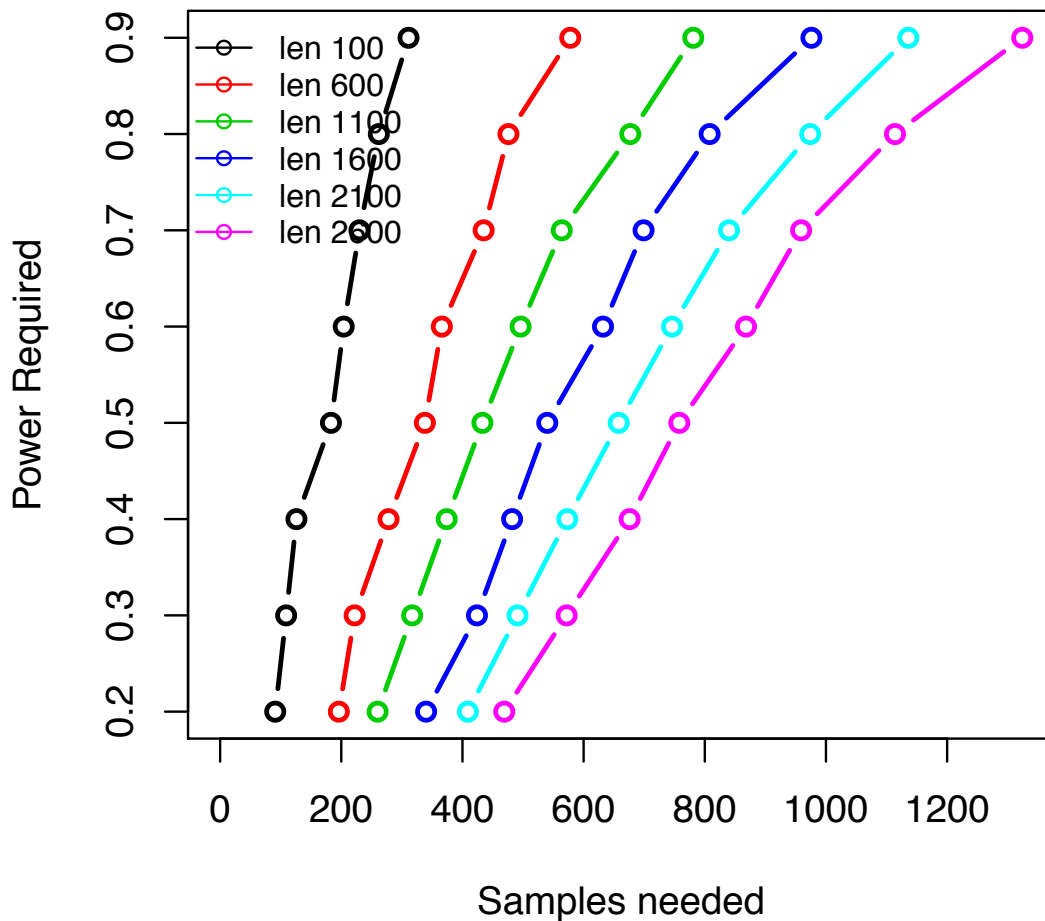
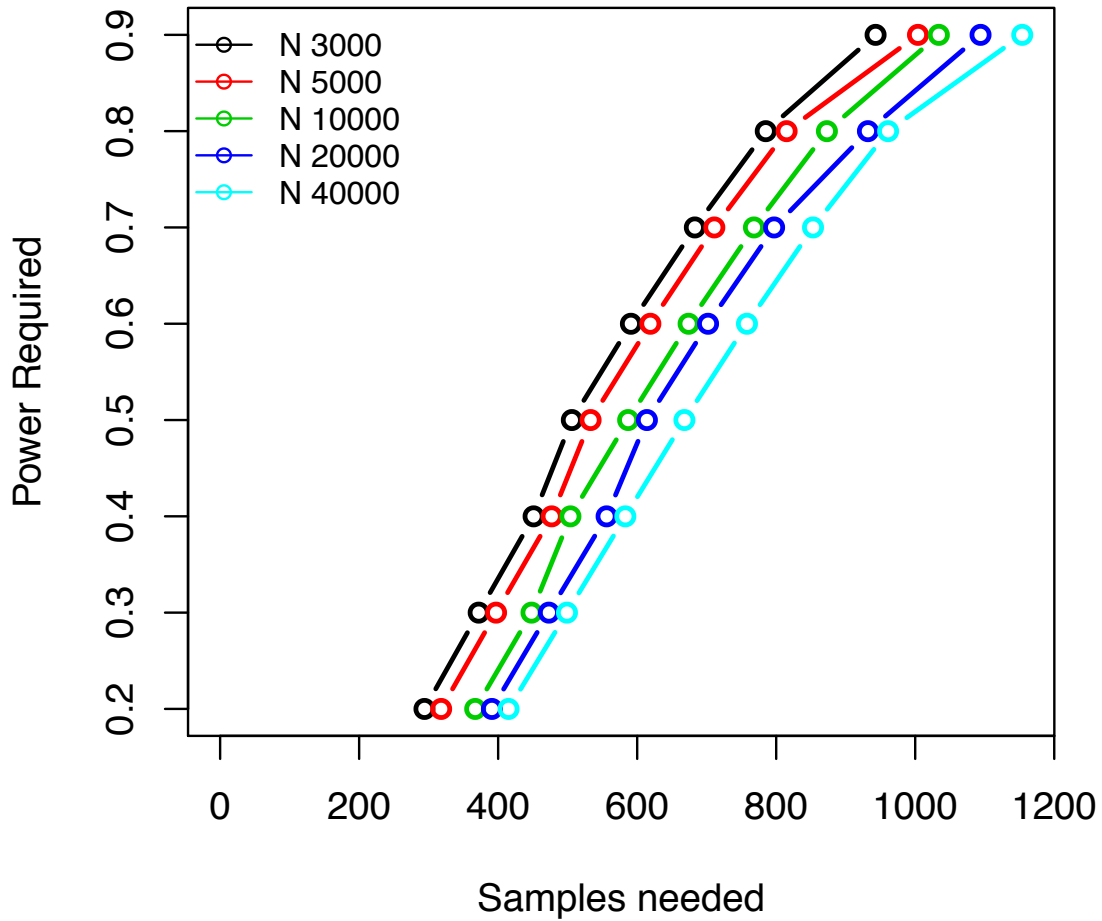


Figure S 3-2 (TL, ||) Power analysis of annotation number

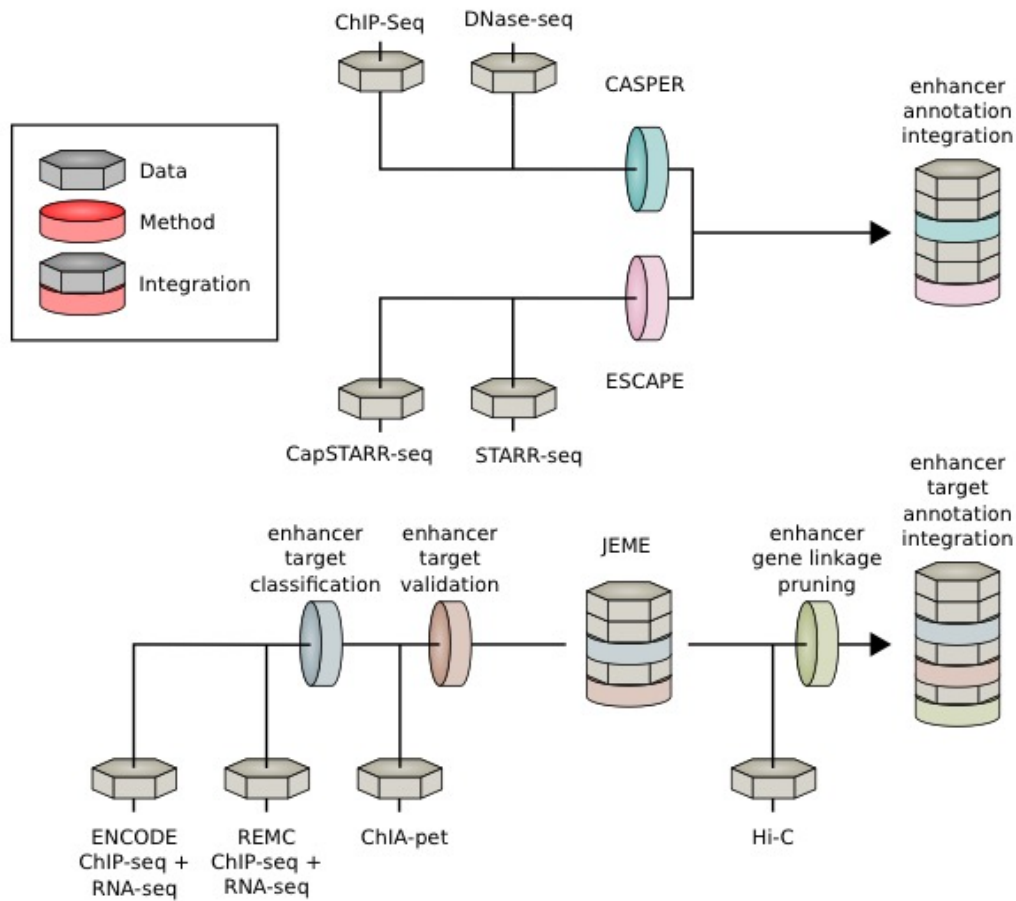


3.2 S (TL, ||) An stepwise screening method to predict enhancers and their gene linkages

In contrast to previous approaches to enhancer annotations (many of which use only histone modification and chromatin accessibility data⁴⁷), we proposed an ensemble method to accurately pinpoint active enhancers and link them to protein coding genes. It composes three computational pipelines (CASPER, ESCAPE, and JEME) to integrate tens of data sets from six different experimental assays, including ChIP-seq, DNase-seq, STARR-seq (CapSTARR-seq), RNA-seq,

ChIA-PET, and Hi-C for higher accuracy. The overall schematic has been summarized into Figure S 3-3.

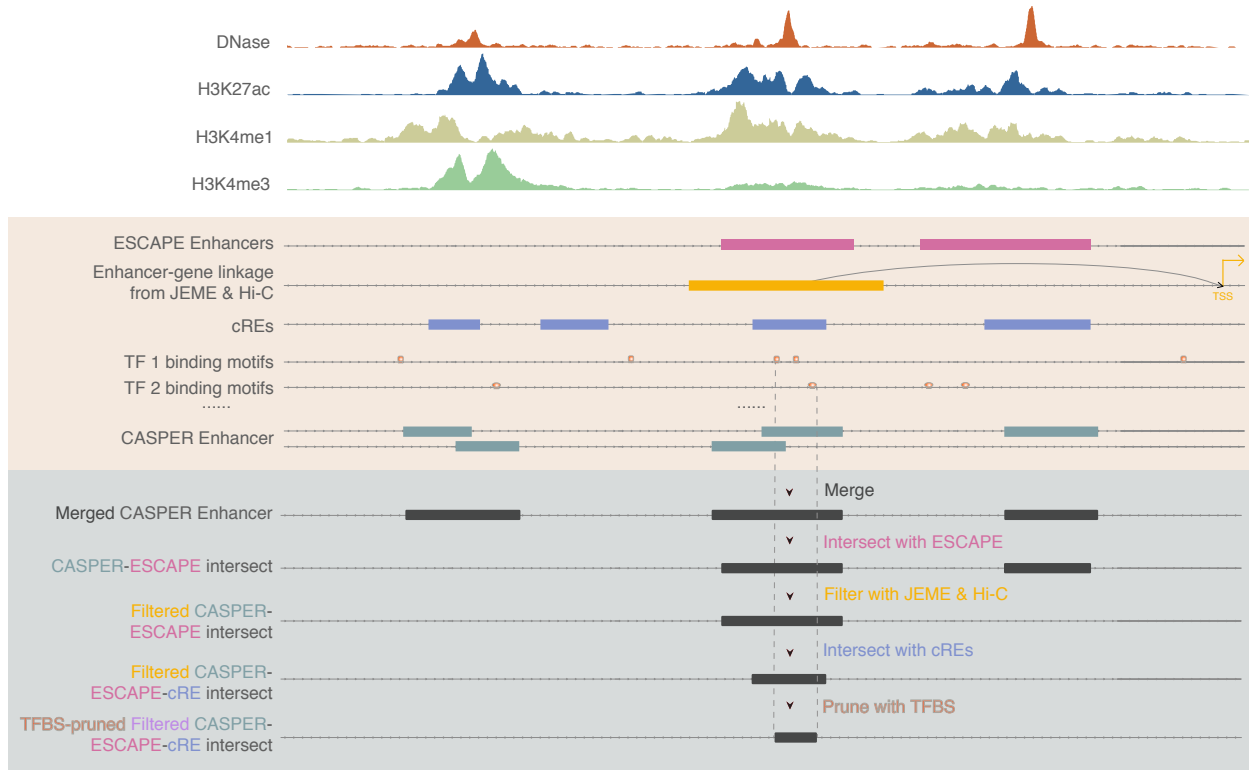
Figure S 3-3 (HL, #) Overall schematic of enhancer and gene linkage



For the enhancer prediction part, we integrated prediction results from different methods and data source, as shown in Figure S 3-4. First, we proposed a computational method, called CASPER, to make enhancer predictions based on pattern recognitions of histone marks (details in Figure S 3-5). The upper white panel of Figure S 3-4 shows an example of the signal tracks (DNase, H3K27ac, H3K4me1 and H3K3me3) of GM12878. Based on these signals and other experiment results, we have a collective data source including enhancers predicted from CASPER and ESCAPE, an enhancer-gene linkage map from JEME and Hi-C, cREs from Phase III encyclopedia and transcription factor (TF) binding sites (middle panel). Specifically, we took intersections of predicted enhancers from CASPER and ESCAPE and further filtered them from target predictions

with JEME and Hi-C results. The resulting list is further refined by intersecting with cREs from the main encyclopedia paper. In the last step, we pruned the enhancers in the list to trim both ends that are not covered by any transcription factor binding motifs (TFBS). The final list is a set of precisely refined and high-confidence enhancers.

Figure S 3-4 (TL, †) Integrated approach to generate high-confidence enhancers list



3.2.1 S (TL, †) Enhancer prediction Pipeline based on ChromAtin Shape Pattern Recognizer (CASPER)

We first developed a framework to detect enhancer regions across the genome through aggregated signals of epigenetic features. Previous analysis demonstrated that regulatory regions are depleted of histone proteins while surrounding regions tend to contain histone proteins with certain post-translational modifications⁴⁸. This characteristic is revealed in many ChIP-seq experiments as enriched peak-trough-peak (double peak) signal at the distal regulatory regions for many activating histone marks. A supervised machine-learning model is well suited to identify this pattern.

For each histone modification, we aggregated the ChIP-seq signals around known enhancer regions. The two maxima in each region are aligned, interpolated and smoothed before averaged to generate meta profile. An additional flipping step was applied to maintain the asymmetry of the two maxima since it might be associated with the directionality of transcription. The meta profile is then used to scan the whole genome to find matched patterns. A 10-fold cross-validation is performed to assess the accuracy of prediction through this method. We found that H3K27ac is the most accurate feature for predicting active regulatory regions. Other features including H3K4me1 and H3K4me2 also achieved high performance.

To achieve higher accuracy, we further developed an ensemble method to combine the normalized pattern-matching result from several different epigenetic marks with linear support vector machine (SVM) (Figure S 3-5). This includes ChIP-seq signals for H3K27ac, H3K4me1, H3K4me2, H3K4me3, H3K9ac and DHS signals associated with active regulatory regions. The ChIP-seq data is available through ENCODE Consortia (<https://www.encodeproject.org>) and Roadmap Epigenomics (<http://www.roadmapepigenomics.org>). The integrated model performs better than each of the individual histone marks, and different integration methods perform similarly. We use linear SVM to assemble the signals to form a discriminant function, where the sign of the result value is used to predict whether a specific region is an enhancer. The resultant enhancers have been summarized in Table S 3-1.

Table S 3-1 (TL, II) Number of enhancers predicted by histone-shape based method

Cell Type	GM2878	HepG2	K562	MCF-7
Number of Enhancers	45,202	61,005	45,801	59,827

Figure S 3-5 (TL, †) Schematic of shape-based enhancer prediction method

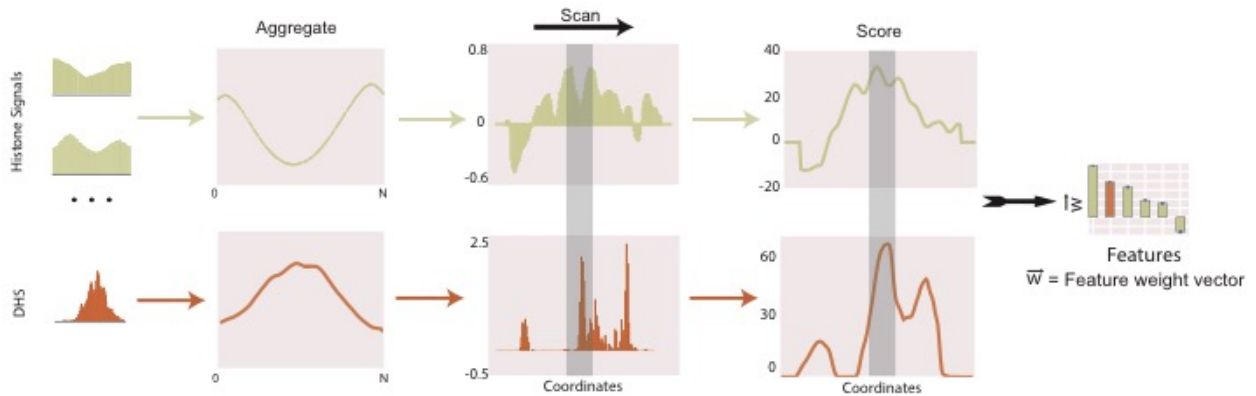
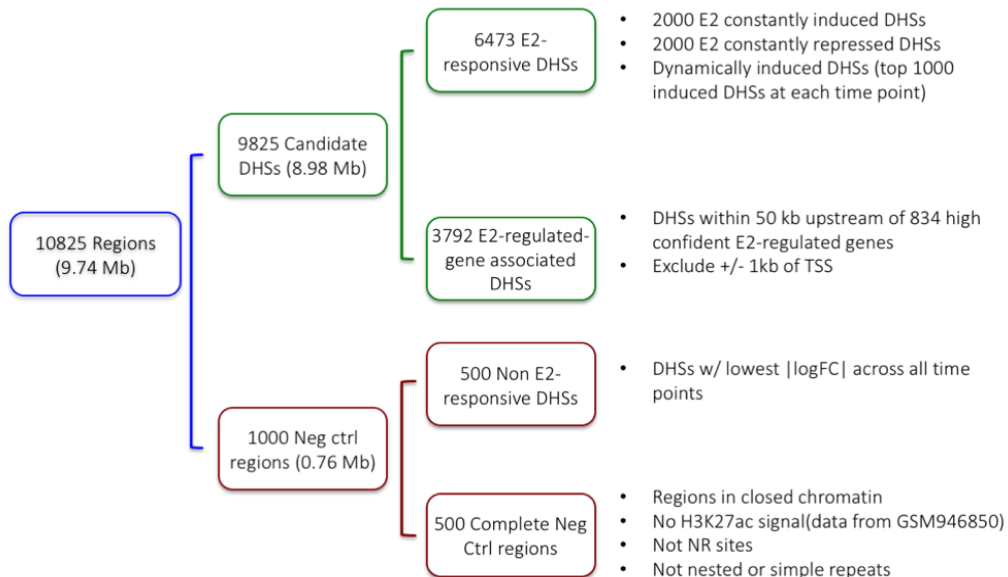


Figure S 3-6 (TL, †) Flowchart of capture STARR-seq target region selection procedure

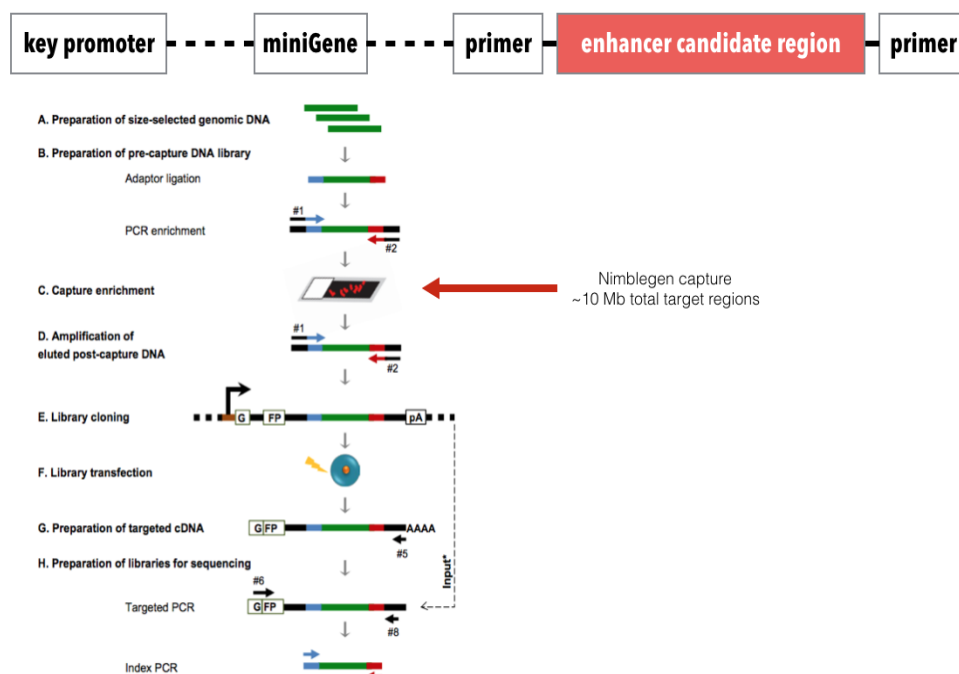


3.2.2 S (TL, †) Enhancer prediction by EnhancerS Peak Calling Pipeline from STARR-seq (ESCAPE)

The whole-genome STARR-seq was performed using a protocol conceptually similar to the previously published STARR-seq technique that was done in the *Drosophila melanogaster*

genome⁴⁹. The CapSTARR-seq is a variant of STARR-seq technique which combines STARR-seq with genome capturing technology⁵⁰. In brief, the genomic DNA from each cell line was fragmented into ~500 bp by sonication and built into plasmid library, which was named as screening library. The screening library was subjected for next generation sequencing. We verified the sequence complexity and genome coverage of screening libraries, which were then transfected into GM12878, K562 or MCF-7 cells by electroporation. After 24 hours of transfection, the plasmid-specific mRNA was purified, reverse transcribed and PCR amplified. The PCR products, which are the so-called STARR-seq libraries, were subjected to sequencing. Both screening library and STARR-seq libraries were sequenced as 100 bp paired-end on the Illumina HiSeq 2500/4000 platforms. The general workflow of the MCF-7 CapSTARR-seq is similar to the whole-genome STARR-seq, however, we captured ~10,000 DNase I hypersensitivity sites (a total length of 9.7 Mb) from fragmented genomic DNA to build the screening library. Compared to the published STARR-seq work, we'd like to note the following innovation and improvement: (1) We significantly increased the complexity of the screening libraries to ensure comprehensive coverage to the human genome; (2) We significantly increased the electroporation scale and efficiency to maximize the size of screening library that got into the cells; (3) We introduced an extra multiplexing step to minimize the bias introduced by PCR duplicates. For the capture based assay for MCF-7 cell line, a total of 10,825 target regions consisting of 9,825 candidate enhancer regions and 1,000 negative control regions were selected tested for regulatory potential. Candidate enhancer regions were selected based on DHS peaks excluding both 1kb upstream and downstream of TSS. Negative control regions were selected from 500 randomly selected regions and 500 non-E2-responsive DHS regions. Details of the selection procedure can be found in Figure S 3-6. (L. Ma et al for GM12878 and K562 whole-genome STARR-seq; S. Yu et al for MCF-7 CapSTARR-seq, in preparation). Candidate enhancer regions were primed and inserted into 3' UTR. Schematics of the experimental procedure can be found in Figure S 3-7.

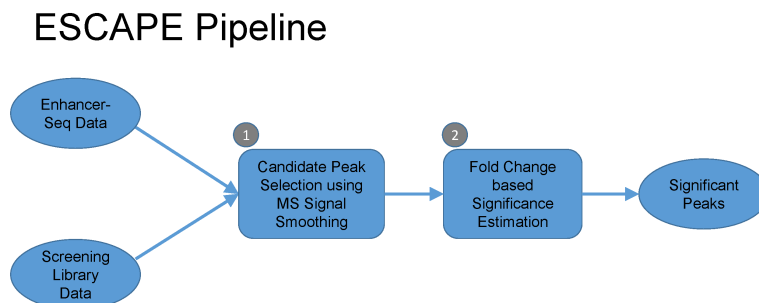
Figure S 3-7 (TL, †) Capture STARR-seq experiment design



To uniformly process the data from whole genome and capture-based STARR-seq assays, (TL, †)we developed a new analysis pipeline named ESCAPE (Figure S 3-8). The pipeline is tailored for optimally processing the output from STARR-seq experiments. The output from an STARR-seq experiment is two datasets for each cell line. First is screen library that contains the sequencing of plasmids from which the enrichment is performed. This screen library serves as a control in the STARR-seq analysis. Second is the actual STARR-seq enriched sequencing data that contains the actual enhancer signal.

We have removed low-quality reads and mapped them using BWA version 0.7.12⁵¹. We have used the reference genome from 1000 Genomes Project's decoy genome⁵². ESCAPE then removes the reads with mapping quality lower than 20 and removes PCR duplicates and estimates fragment length distribution using cross-correlation between the strands (Figure S 3-9). Then the STARR-seq signal tracks are generated to perform peak calling. The STARR-seq signal shows lower fold change characteristics compared to ENCODE ChIP-seq datasets (Figure S 3-9).

Figure S 3-8 (TL, #) Schematic of ESCAPE pipeline



For peak calling, ESCAPE uses the following strategy: First, the peak candidates are identified. For the whole genome assay, ESCAPE uses a multiscale decomposition based peak calling strategy⁵³. For this, we have decomposed the signal using smoothing filters with lengths varying between 100 and 2000 base pairs. The filtering can be summarized with following formula:

$$x_i^s = \text{median} \left(\{\tilde{x}_a\}_{a \in [i - \frac{l_s}{2}, i + \frac{l_s}{2}]} \right), l_s \in (l_{start}, \lfloor l_{start} \times \sigma \rfloor, \dots, l_{end}) \quad (3-1)$$

where x_i^s is the i^{th} signal level at scale decomposition s . The smoothing window length is l_s . Then we identified the local minima in the smoothed signal profiles and used these as possible enriched regions. For this, ESCAPE first estimates the derivative at each point:

$$dx_i^s = (x_i^s - x_{i-1}^s) \quad (3-2)$$

where dx_i^s is the derivative of the smoothed signal x_i^s . The local extrema are found as the points where the derivative flips its sign:

$$I_{min} = \{i \mid dx_i^s < 0, dx_{i-1}^s > 0\} \quad (3-3)$$

$$I_{max} = \{i \mid dx_i^s > 0, dx_{i-1}^s < 0\} \quad (3-4)$$

where I_{min} and I_{max} are the sets of positions of minima and maxima of x_i^s , respectively. The scale specific candidate enriched regions of x_i^s are identified as the regions between the consecutive minima. The multiscale decomposition approach identifies enriched regions at different length scales that correspond to punctate features like enhancers. Then, ESCAPE

computes the fold change on each peak candidate as the ratio of total signal in the STARR-seq signal and screening library signal. We refer to this as FC :

$$FC = \frac{\sum_{i=s}^e x_i^s}{\sum_{i=s}^e y_i^s} \quad (3-5)$$

where y_i^s represents the value of screening library signal profile at position i . For capture based assay, ESCAPE uses a more focused analysis to identify candidate peak regions. For each capture region, ESCAPE selects a bins size that balances the peak calling sensitivity and specificity. To set a threshold for the fold change to select candidate peaks, we exchanged screening library and STARR-seq and we computed the fold change on the candidate peaks, which we refer to as FC_{random} :

$$FC_{random} = \frac{\sum_{i=s}^e y_i^s}{\sum_{i=s}^e x_i^s} \quad (3-6)$$

These fold change scores serve as a random distribution of fold change scores. We use this distribution for selecting a fold change threshold. For a FC threshold fc , we estimated the false discovery rate as the ratio of number of peaks that for which $FC_{random} > fc$ and the number of peaks for which $FC > fc$. We set the FDR threshold at 0.1% and filtered the peaks that do not satisfy the FC threshold selected using this FDR threshold. For capture based assay, ESCAPE uses the candidate enriched regions with top 10% FC values.

Figure S 3-9 (TL, #) Whole genome STARR-seq signal enrichment properties

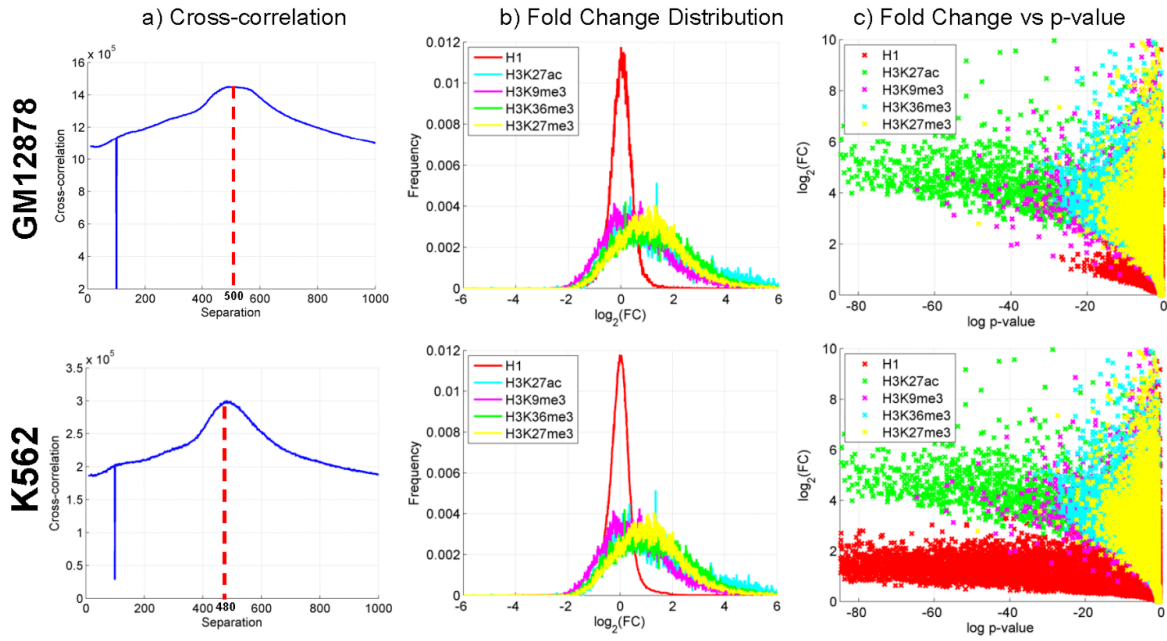
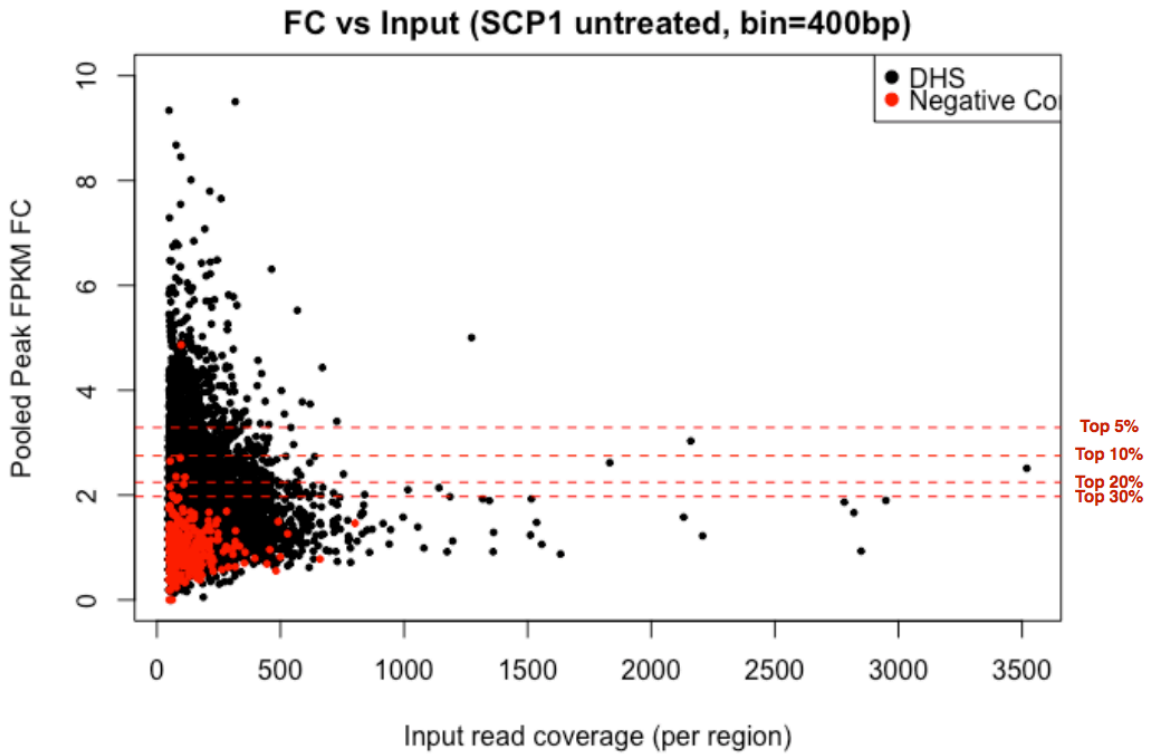


Figure S 3-10 (TL, #) Capture STARR-seq experiment properties



3.2.3 S (TL, #) Enhancer Target prediction

3.2.3.1 S (TL, #) Enhancer Gene linkage prediction using JEME

Enhancer targets were predicted using JEME (Joint Effect of Multiple Enhancers, Yip *et al.*, Nature Genetics, in press), which involves two main steps (Figure S 3-11). In the first step, the transcript levels around each transcription start site (TSS) in 49 ENCODE and Roadmap Epigenomics cell lines (Table S 3-2) were modeled based on histone modification data at nearby enhancers without requiring any known enhancer-target pairs as examples. Specifically, for each enhancer feature i the expression level y of a TSS is modeled as $y = a_{i0} + \sum_j a_{ij} x_{ij}$, where the summation is over all enhancers j within 1Mbp from the TSS, and x_{ij} is the value of feature i of enhancer j . The coefficients a_{ij} of the enhancers are learned by LASSO, which minimizes the regression error over all samples while selecting a small number of enhancers to have non-zero coefficients. The features considered include H3K4me1, H3K27ac and H3K27me3 (A separate model involving only the latter two features was built when constructing the enhancer-target network in MCF-7 since H3K4me1 data were unavailable).

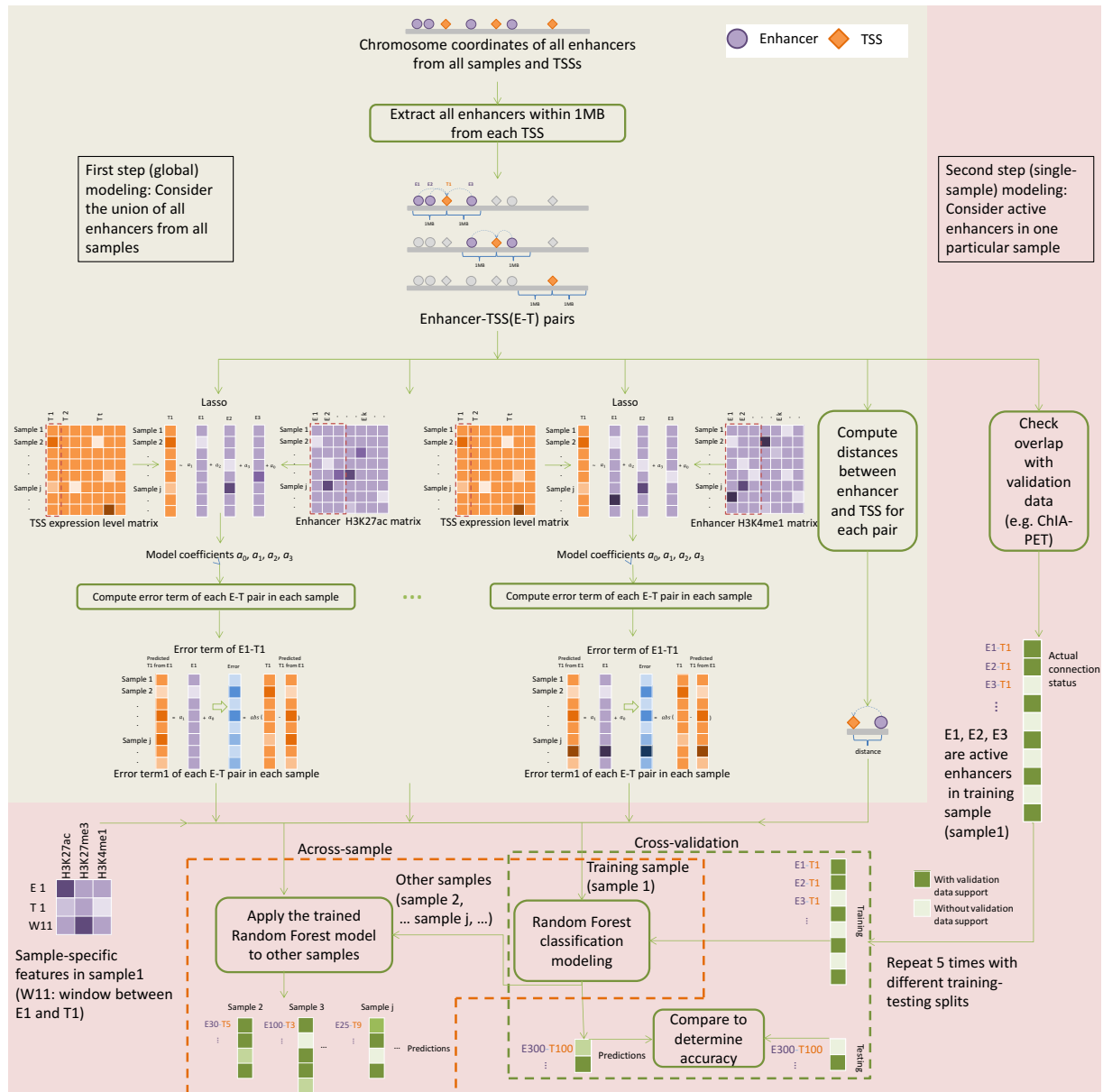
In the second step, single-enhancer error terms were first computed. Specifically, an error term is computed to check how much the expression y_k of the TSS in sample k can be explained by considering each feature i of each enhancer j , i.e., $e_{ijk} = |y_k - (a_{i0} + a_{ij}x_{ijk})|$, where x_{ijk} is the value of feature i of enhancer j in sample k and a_{i0} and a_{ij} are the coefficients learnt in the first step. These error terms were then combined with genomic distance and cell-line-specific data (i.e. the levels of histone modifications across the enhancer, the TSS and the window between them in sample k) to predict the enhancers that regulate a TSS in a particular cell line using a Random Forest model. The parameter values of these second-level models were learned from published ChIA-PET data from K562 and MCF-7 cell lines. A 5-fold cross-validation procedure was used to evaluate the accuracy of the predicted enhancer-target pairs. The model was then applied to those samples without ChIA-PET data.

Table S 3-2 (TL, †) The 49 ENCODE and Roadmap Epigenomics cell lines used to construct enhancer-target networks by JEME

Data source	Cell lines
ENCODE	GM12878
ENCODE	HepG2
ENCODE	K562
ENCODE	MCF-7
ENCODE	A549
ENCODE	HeLa-S3
ENCODE	HMEC
ENCODE	HSMM
ENCODE	HUVEC
ENCODE	NHEK
ENCODE	NHLF
REMC	H1 Cells
REMC	H1 BMP4 Derived Mesendoderm Cultured Cells
REMC	H1 BMP4 Derived Trophoblast Cultured Cells
REMC	H1 Derived Mesenchymal Stem Cells
REMC	H1 Derived Neuronal Progenitor Cultured Cells
REMC	hESC Derived CD184+ Endoderm Cultured Cells
REMC	hESC Derived CD56+ Ectoderm Cultured Cells
REMC	hESC Derived CD56+ Mesoderm Cultured Cells
REMC	HUES64 Cells
REMC	Primary T helper memory cells from peripheral blood 2
REMC	Primary T helper naive cells from peripheral blood
REMC	Primary T CD8+ naive cells from peripheral blood
REMC	Primary hematopoietic stem cells G-CSF-mobilized Female
REMC	Foreskin Fibroblast Primary Cells skin01
REMC	Foreskin Fibroblast Primary Cells skin02
REMC	Foreskin Keratinocyte Primary Cells skin03
REMC	Foreskin Melanocyte Primary Cells skin01

REMC	Foreskin Melanocyte Primary Cells skin03
REMC	Primary mononuclear cells from peripheral blood
REMC	Aorta
REMC	Liver
REMC	Brain Hippocampus Middle
REMC	Esophagus
REMC	Fetal Intestine Large
REMC	Fetal Intestine Small
REMC	Pancreatic Islets
REMC	Gastric
REMC	Left Ventricle
REMC	Lung
REMC	Ovary
REMC	Pancreas
REMC	Psoas Muscle
REMC	Right Atrium
REMC	Right Ventricle
REMC	Sigmoid Colon
REMC	Small Intestine
REMC	Thymus
REMC	Spleen

Figure S 3-11 (TL, †) Schematic of JEME



3.2.3.2 S (TL, †) Enhancer gene linkage pruning using Hi-C data

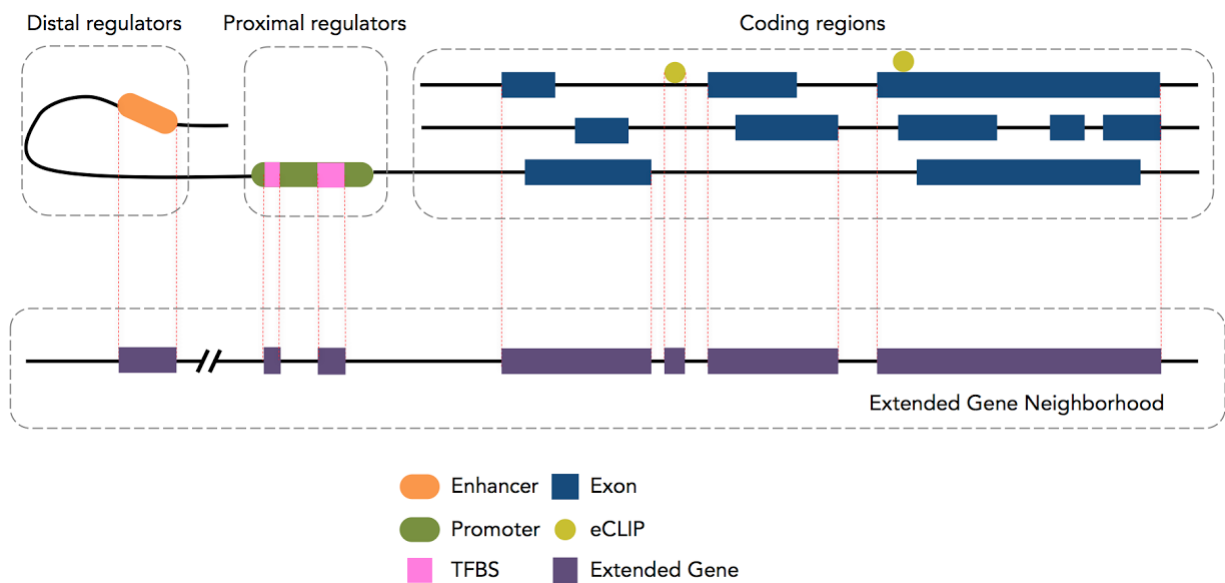
Enhancer target predictions are further filtered by using Hi-C data. Contact maps of individual chromosomes (in 5kb bins) for both K562 and GM12878 cell lines were obtained from Rao *et al*⁵⁴. MCF-7 contact maps (40kb) were obtained from Barutcu *et al*⁵⁵. Element (i, j) in a contact map represents the frequency of interactions between genomic loci i and j . For all possible (i, j), we

used the tool Fit-Hi-C to estimate the statistical significance of the contact frequency based on the coverage of the loci as well as their genomic distance⁵⁶ and to keep the interactions with $q\text{-value} < 0.1$. We then used the list of significant loci to filter the enhancer-target predictions. Only enhancer-gene pairs in which enhancer and gene are respectively belong to a pair of significantly interacting loci are kept for further analysis.

3.3 S (TL, ||) Extended gene neighborhood generation

Here we generated the extended gene neighborhoods by combing the coding region with the key non-coding proximal and distal regulatory elements together for a joint mutation burdening quantification. Details of the schematic are given in Figure S 3-12.

Figure S 3-12 (HL, ||, shadow figure for Fig. 2 C) Schematic of extended gene definition



3.4 S (TL, ||) P-value summaries

To check the distribution of P-values vs. the theoretical ones, the Q-Q plots were given in Figure S 3-13 to Figure S 3-15.

Figure S 3-13 (TL, #) Q-Q plots of P-values for CLL.

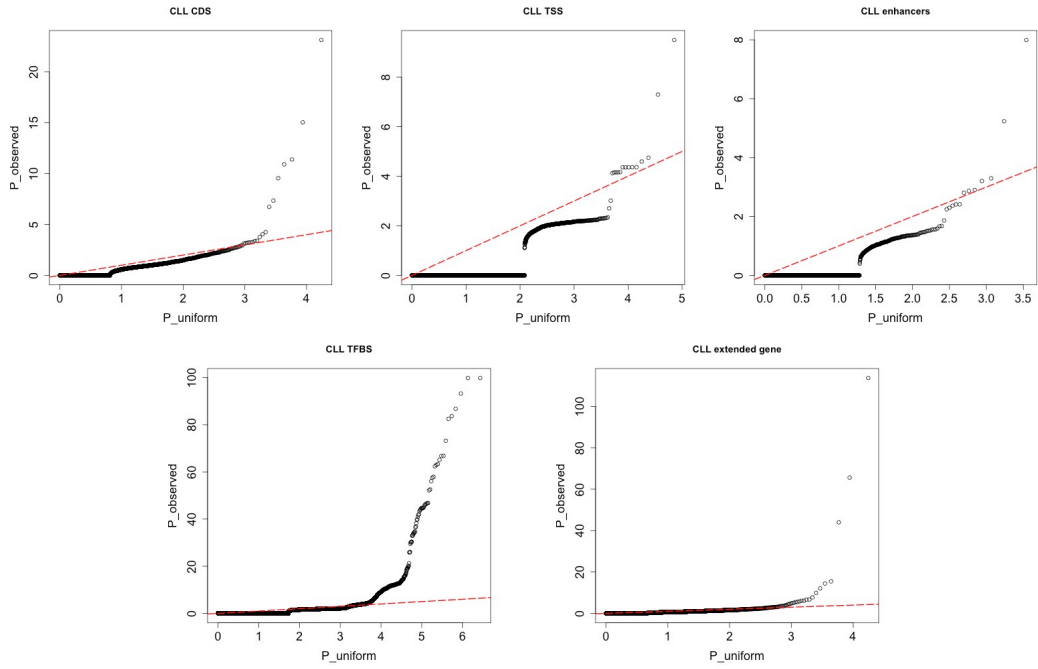


Figure S 3-14 (TL, #) Q-Q plots of P-values for BRCA.

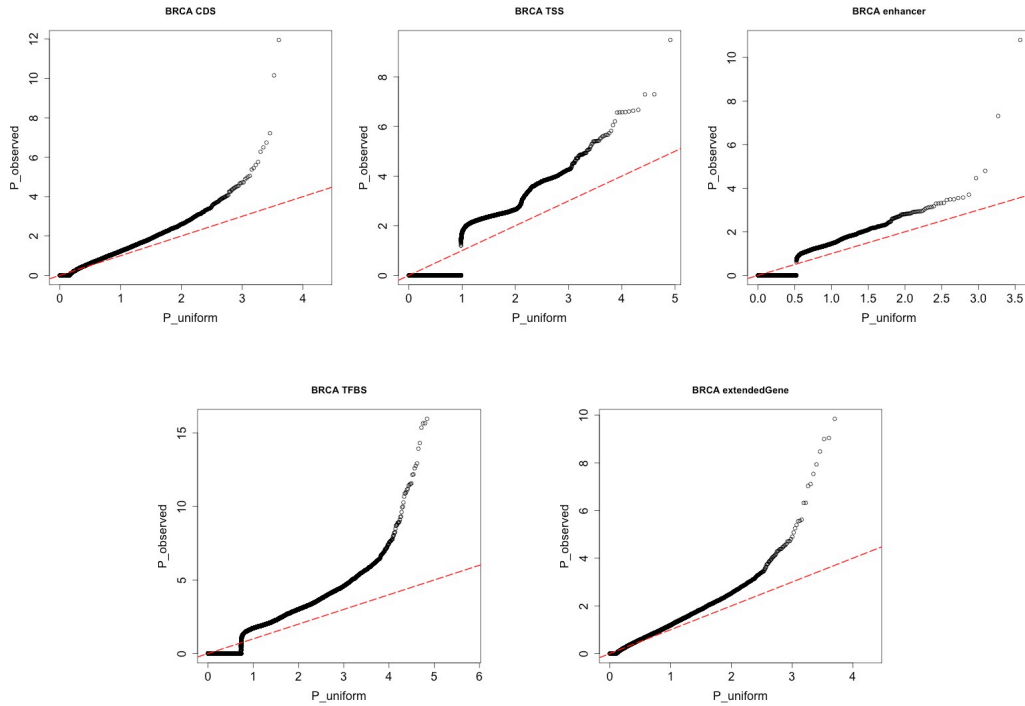
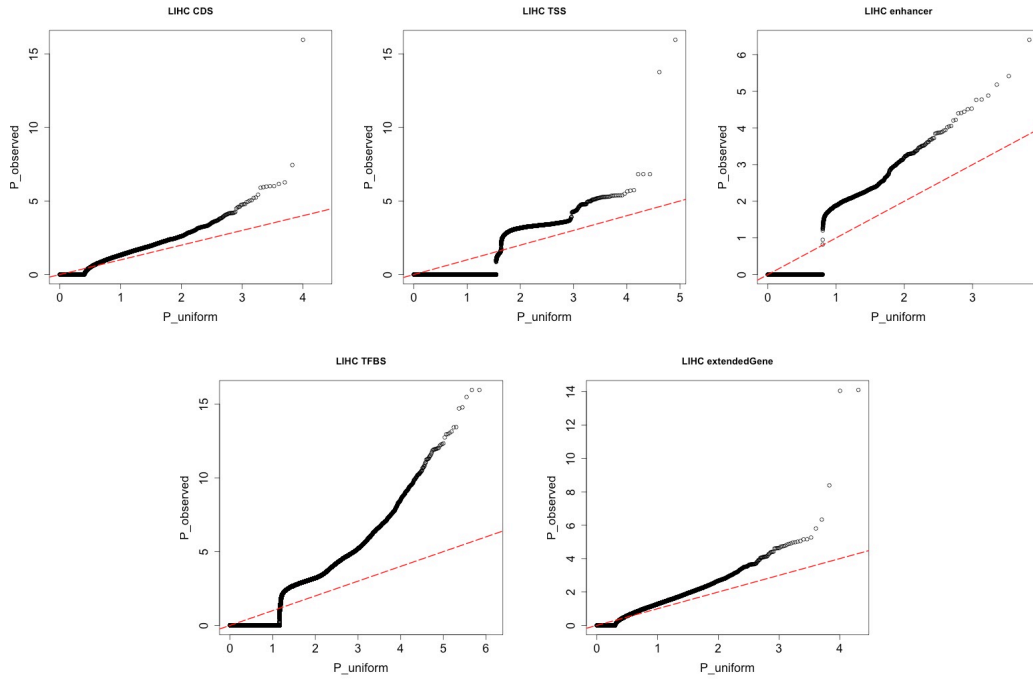


Figure S 3-15 (TL, †) Q-Q plots of P-values for LIHC

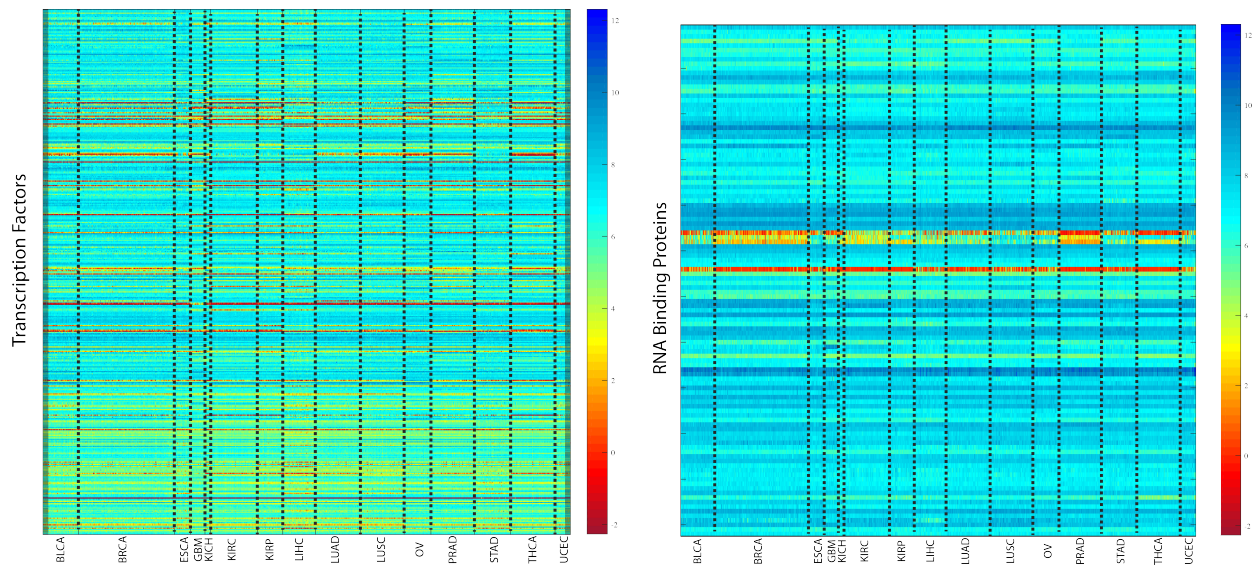


4 S (TL, ||) More details about “Interpreting tumor expression profiles using ENCODE networks identifies key regulators”

4.1 S (TL, †) Expression pattern of TF and RBPs across cancer types.

We plotted the expression values of TF and RBPs across different cancer types to show the difference in expression in different cancer types.

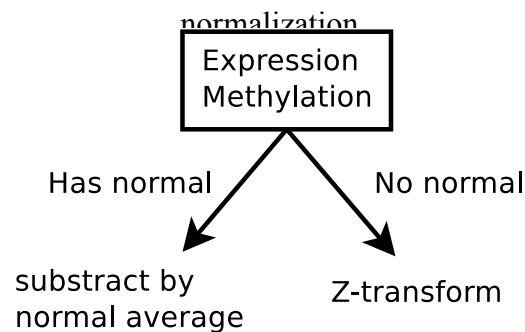
Figure S 4-1 (TL, †) Expression patterns of transcription factors across cancer types



4.2 S (TL, †) TCGA expression data processing

All TCGA expression, methylation and mutation data were downloaded from GDAC firehose (<http://gdac.broadinstitute.org>) with data version of 2016_01_28. For cancer types with normal control samples profiled, the expression values of each gene are subtracted with the average value of all normal controls. For cancer types without any normal samples profiled, the expression profile of each gene is transformed to zero mean and unit deviation. The DNA methylation values are also normalized in the same way as RNASeq data, according to the availability of normal control samples in each cancer type. For copy number alteration (CNA), GDAC firehose does not provide standardized data, therefore we downloaded the data matrix from cBioportal with data version of 2016_10_20 (<http://www.cbioportal.org>).

Figure S 4-2 (TL, †) Schematic of RNA-seq



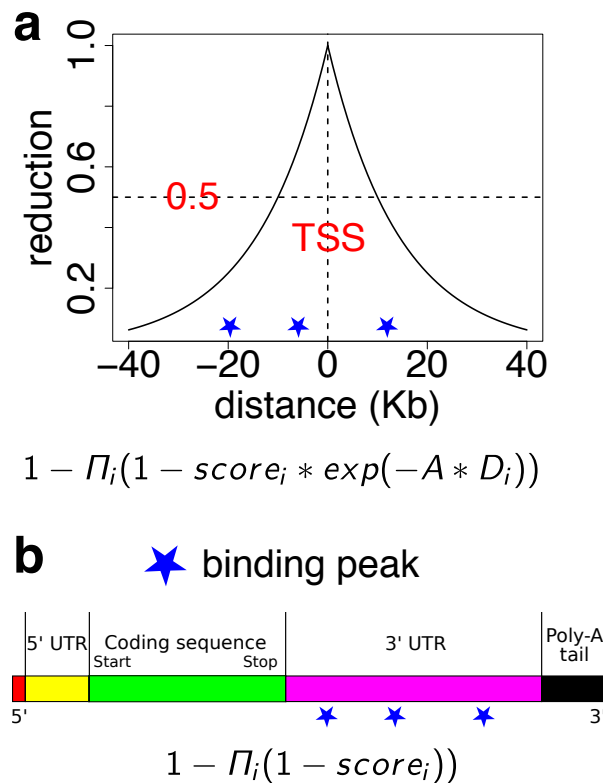
4.3 S (TL, †) Probabilistic Regulatory network construction from ChIPSeq and eCLIP data

For regulatory analysis, we only considered transcription factors (TF), chromatin regulators (CR), and RNA binding proteins (RBP). In total, there are **978** TF/CR ChIPSeq profiles and **159** RBP eCLIP profiles downloaded from ENCODE DCC as of January 4th, 2017 (<https://www.encodeproject.org>).

All ChIP-seq and eCLIP peak scores are linearly scaled into range (0,1). The regulatory score between TF peaks and gene promoters were built with “connect_host” commands from RABIT

package (Regression Analysis with Background InTegration, <http://rabit.dfci.harvard.edu>) following an exponential decay model (Figure S 4-3 a). A regulatory score between RBPs and genes were built through counting eCLIP peaks within gene 3'UTR regions (Figure S 4-3 b). The following steps were made to construct the network. a) For ChIP-seq data, A regulatory potential score is calculated between each pair of ChIP-seq peak and gene TSS by multiplying the ChIP-seq intensity score with an exponential decay score $\exp(-A * \text{Distance})$ of their distance between. The coefficient A is set as $\log(2)/10K$, so that a binding peak 10K bps away from gene TSS will decay by 50%. For each gene TSS, if there are several peaks of a TF nearby, we merged their regulatory potential scores by noisy-or: (b) For eCLIP data, only binding peaks over gene 3'UTR regions were considered for possible regulatory role of transcript stability. For each gene 3'UTR region, if there are several peaks of a RBP, we merged their regulatory potential scores by noisy-or operation. All regulatory potential scores stay within range (0,1).

Figure S 4-3 (TL, ‡) Regulatory network construction



ChIPSeq and eCLIP profiles were excluded from further analysis if the total sum of regulatory scores across all human genes is less than 100. All general TFs including Pol2 and Pol3 were excluded from further analysis. For certain TF, there exist many ChIP-seq profiles profiled in different conditions. We run a hierarchical clustering among all of its ChIP-seq profiles and cut the hierarchical tree at correlation distance of 0.2. Only profiles in the largest cluster are used for further analysis. The final size of regulatory networks constructed are shown in Table S 4-1. For each data type, column “Profile” represents the number of experimental profiles (ChIP-seq or eCLIP) that passed our quality controls. Column “Regulator” represents the number of regulators (TF, CR or RBP) analyzed. Column “Condition” represents the number of experimental conditions included in profiles. Column “Target” represents the total number of human genes profiled as targets of analyzed regulators.

Table S 4-1 (TL, †) Statistics of regulatory networks.

	Profile	Regulator	Condition	Target
ChIPSeq	762	496	44	21,348
eCLIP	159	112	2	14,593

To systematically search for TFs that drive tumor-specific gene expression patterns, we used a previously developed integration framework RABIT (Regression Analysis with Background InTegration, <http://rabit.dfc.harvard.edu>). In the RABIT framework, for a given TF ChIP-seq binding profile, candidate target genes are identified by weighting the number of binding sites by their distance to the transcription start site (TSS) of each gene. For a given eCLIP RBP binding profile, candidate genes are identified through searching the binding sites within the gene 3’UTR regions. RABIT uses three steps to identify TFs (or RBPs) that drive tumor-specific gene expression patterns at both the individual tumor level and the whole cancer type level. In Step one, RABIT screens for TFs that significantly affect the gene expression patterns in each tumor, and selects the most relevant ChIP-seq (or eCLIP) profile if multiple profiles exist for the same regulator. In Step two, RABIT further selected a subset of TFs among those screened in Step one to achieve an optimized model error. In Step three, RABIT investigates how well the public ChIP-seq profiles can capture the active TF targets in each cancer type, and clean up insignificant TFs.

The final output of RABIT framework is a set of TFs or RBPs that shape the tumor-specific expression patterns at individual tumor level in each cancer type.

Based on ENCODE ChIPSeq data and TCGA profiles, we applied RABIT framework to identify TFs whose target genes are differentially regulated in cancer. The fractions of patients with TF targets differentially regulated are shown. Only TFs with targets differentially regulated in over 40% patients in at least two cancer types are included, and results were summarized into Figure S 4-4. We further extracted those TFs with stronger signals to shown in Figure S 4-4. Except the well-known MYC targets showing consistent up-regulation pattern across multiple cancer types, we also found novel TFs such as ZNF687 to be strongly up-regulated in breast and prostate cancer (star in Figure S 4-4). Also, the breast tumors were further classified into subtypes according to PAM50 classification and ER status to show the scores predicted by RABIT for each subtype by boxplots. We further checked in each TCGA cancer type, the fractions of patients detected with different types of ZNF687 alterations (Figure S 4-5 b).

Figure S 4-4 (TL, ||, shadow figure for Fig. 4) Heatmap of TF activities in multiple cancer types

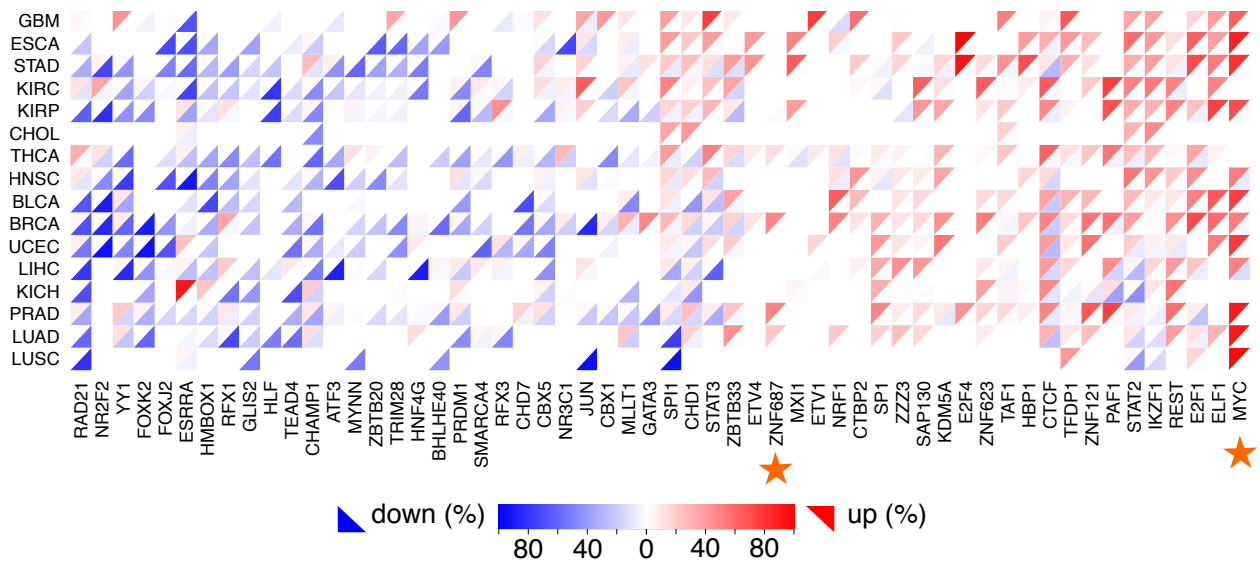
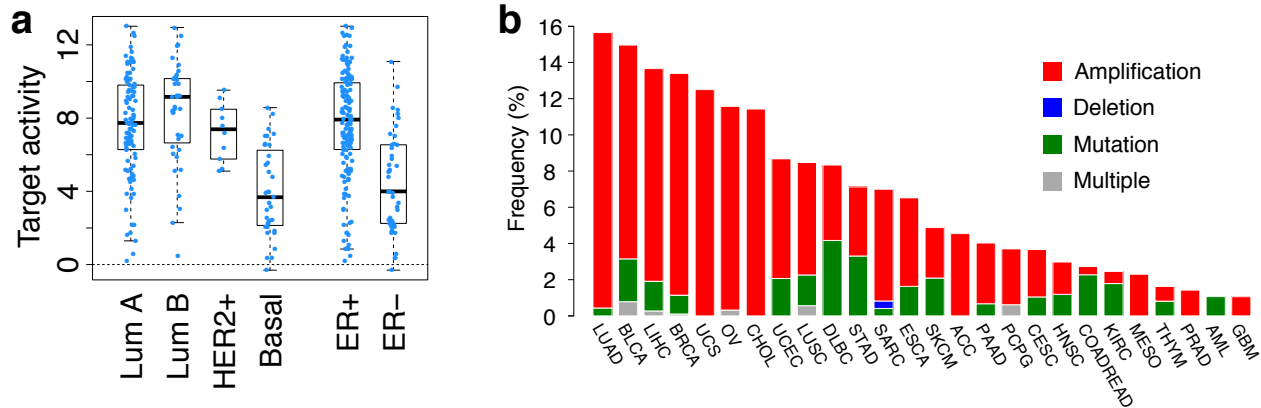


Figure S 4-5 (TL, ||) The potential role of ZNF687 in cancer



SUB1 was also predicted to be significantly associated with expression changes in multiple tumor types. Here we have listed the full predictions in all cancer types for SUB1. In each cancer type, the association between SUB1 expression and SUB1 regulatory activity predicted by RABIT was tested through t-test in linear regression. Only significant associations above FDR threshold 0.05 are shown in Table S 4-2.

For the SUB1 survival plot in Fig. 4, the association between SUB1 regulatory activity computed for each TCGA tumor for each cancer type studied in TCGA and overall survival was tested through two-sided Ward test in Cox-PH regression. In the KM-plot, all patients with SUB1 regulatory activity larger than 2 were categorized as high and the rest were categorized as low.

Table S 4-2 (TL, ||) Correlation between SUB1 expression and target activity

Cancer	Coef	Stderr	<i>t</i> -value	<i>p</i> -value
THCA	4.79	0.46	10.46	9.03E-23
OV	4.47	0.61	7.37	1.53E-12
LUAD	2.87	0.46	6.22	3.25E-09
PRAD	2.9	0.48	6.02	4.56E-09
HNSC	2.61	0.46	5.72	2.73E-08
KIRC	3.6	0.63	5.73	5.66E-08
GBM	2.93	0.54	5.47	2.60E-07
LIHC	3.22	0.64	5.02	1.18E-06
BLCA	3.21	0.66	4.83	3.91E-06
LUSC	2.8	0.66	4.25	6.39E-05

KIRC	1.91	0.5	3.83	1.62E-04
STAD	2.16	0.57	3.76	2.14E-04
ESCA	1.67	0.54	3.09	2.34E-03
UCEC	1.47	0.52	2.84	5.28E-03
KICH	1.64	0.58	2.8	6.71E-03

5 S (TL, ||) More details about “Cell-type specific regulatory networks highlight extensive rewiring events during oncogenesis”

5.1 S (TL, †) Regulatory network

5.1.1 S (TL, †) TF network

We defined the TF network directly from the TF-gene interactions based on ENCODE uniformly processed ChIP-seq peak calls. We first defined TF-gene regulatory network in each cell type by searching for TF to gene linkages based on their proximities to the TSS. In addition, we also used target identification from profiles (TIP) method that quantitatively measures the regulatory relationships between TFs and target genes to define a subset of the full TF-gene network⁵⁷. We also provide a more generalized network by reconciling networks from multiple cancer types and applied it in a pan-cancer analysis. All networks were summarized in the supplementary datasheet. For more details, please refer to the section 5.3.2 S.

5.1.2 S (TL, †) RBP network

We defined the RBP network based on the RBP-gene interactions from eCLIP peak calls. eCLIP peak scores between RBPs and genes were built through counting eCLIP peaks within gene's 3'UTR regions and then linearly scaled into range (0,1). For more details, please refer to section 4.3 S. To provide a strict and lenient RBP network, we use 0.9 and 0.1 as the threshold for interaction cutoffs. RBP networks are summarized in the supplementary datasheet.

5.2 S (TL, †) Reconcile with the main ENCODE encyclopedia

Both promoter and enhancer annotations from EN-CODEC were carefully consolidated with the main ENCODE Encyclopedia resources. The ENCODE Encyclopedia comprises of three levels, two integrative levels of annotations and the ground level raw data. The ground level includes peaks and quantifications produced by uniform processing pipelines for individual data types. The integrative level contains annotations produced by integrating multiple data types. The

core of the integrative level is the Registry of candidate Regulatory Elements (cREs). The registry contains approximately ~1.31M human cREs and each cRE has a cell-type non-specific accession number, which then can be browsed from SCREEN (Search Candidate Regulatory Elements by ENCODE, <http://screen.umassmed.edu/>).

Annotations from EN-CODEC were merged against the Registry of candidate Regulatory Elements (cREs). We assigned cell type non-specific cRE accession numbers to ESCAPE and CASPER integrated enhancer annotations when the region had more than 1bp overlap. When there were more than one accession numbers associated with the annotation, we assigned multiple accession numbers to the element. Overall, there was 99% overlap between integrated enhancer annotations and cREs with each element being mapped to 2.5 cRE accessions on average.

For cases without an overlap, we assigned special accession numbers EH37EXXXXXXX-C where XXXXXXXX are replaced with numbers starting from 0000001.

To access the cRE using accession number, one can use the URL <http://screen.umassmed.edu/search/?q={accession}&assembly=hg19#> where {accession} is replaced with the cRE accession number. From SCREEN, one can look up H3K4me3, H3K27ac, CTCF, and DNase Z-scores and signal profiles across all available ENCODE cell types.

5.3 S (TL, ||) Rewiring analysis based on direct counts

5.3.1 S (HL, ||) TF-gene linkage

We evaluated the rewiring of TF to gene linkages between normal and cancerous cells. To define TF rewiring between cell types, we first defined TF-gene regulatory network in each cell type using simple count based target gene linkage. We used two different methods that examine TF to gene linkages based on their proximities to the TSS. For the TSS-based method, we simply used 2,500bp upstream and downstream of transcription start site (TSS) based on Gencode v19 annotation as a boundary for the proximal regulatory region. On average, 33.5% of TF ChIP-seq peaks fell into promoter region. We defined a target gene linkage if TF ChIP-seq peak was found within the boundary. However, we discovered, in Gencode annotation, there were numbers of genes that have more than 50 alternative TSS, which gave these genes unfair advantages of having more target gene linkages than others since their proximal regulatory regions can span up to

250kbp. Therefore, we selected one canonical TSS for each gene based on the total number of aggregated ENCODE TF ChIP-seq peaks. While this method is far from perfect, we believe this is the best method to capture the high-level TF network rewiring and quantify epigenetics changes around TSS while minimizing artifacts when counting all TSSs from all possible alternative transcripts.

In addition to TSS-based TF-gene linkages, we used target identification from profiles (TIP) method that quantitatively measures the regulatory relationships between TFs and target genes to define a subset of the full TF-gene network. For each TF, TIP model builds a characteristic, averaged profile of binding around the TSS and then uses this to weight the sites associated with a given gene, providing a continuous-valued 'regulatory' score relating each TF and potential target⁵⁷. We used false discovery rate of 0.1 for cutoff. Since TIP uses narrower promoter definition than TSS-based method, we defined the TIP-based network as a subnetwork of the TSS-based network.

5.3.2 S (HL, ||) Full regulatory network, merged network, and network rewiring

Both promoter-based linkages and enhancer target based linkages were merged into one to build a complete TF-gene network. For more information about enhancer target based linkages, please refer to section 3.2.3 S. Two versions of full regulatory networks were constructed; one larger network by concatenating TSS-based network and enhancer-based network and another subnetwork by concatenating TIP-based network and enhancer-based network. In addition, we built a merged network by combining all available ENCODE tissue types.

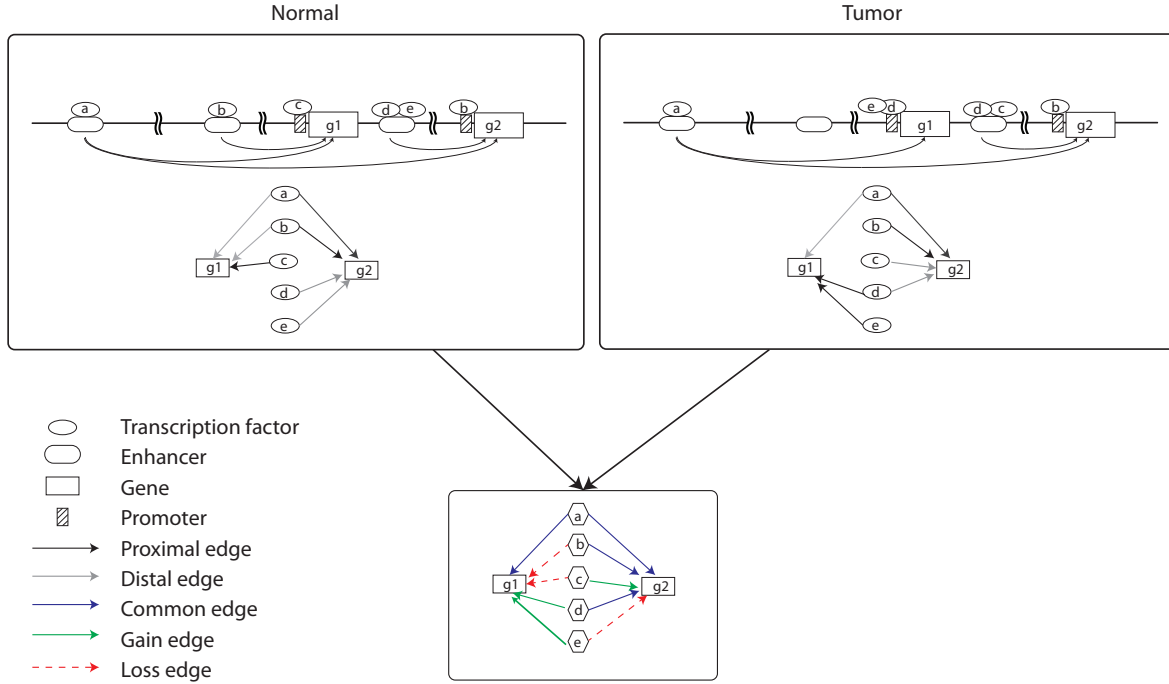
Rewiring of edges between TF and target genes were compared in normal and tumor cells as shown in Figure S 5-1. If a target gene linkage was found in normal but lost in tumor, the edge was marked as loss edge. Similarly, if a target gene linkage was found only in tumor, it was labeled gain edge, and for edges found in both, they were labeled common or retained edges

5.3.3 S (TL, ||) Rewiring score

To quantify rewiring events, we first calculated rewiring score for each regulators (TFs). The fraction of the number of gain, loss, and common edges to the number of fully connected network

edges, where all available TF nodes are fully connected with all available gene targets in the whole network was used to calculate the raw rewiring score.

Figure S 5-1 (HL, II) Network rewiring schematics



$$n_{\text{fully-connected}} = n_{\text{TF}} * n_{\text{gene}} - 1$$

$$rScore_{\text{TF}} = \frac{\frac{G_{\text{in}} + G_{\text{out}}}{L_{\text{in}} + L_{\text{out}}}}{\left| \frac{G_{\text{in}} + G_{\text{out}}}{L_{\text{in}} + L_{\text{out}}} \right|} \cdot \frac{(G_{\text{in}} + G_{\text{out}} + L_{\text{in}} + L_{\text{out}})}{n_{\text{fully-connected}}} \quad (5-1)$$

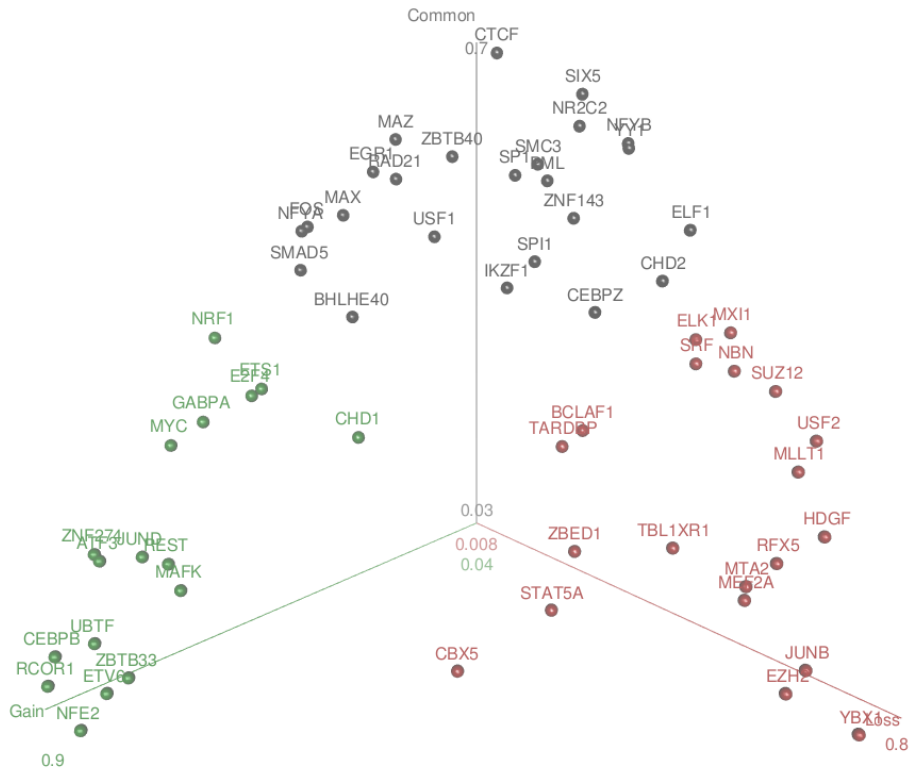
$$rScore_{\text{normalized}} = \frac{rScore_{\text{TF}}}{\max(rScore)}$$

The rewiring score, rScore, after taking normalization over the maximum rScore, was used to rank the TF from the gainer to loser.

5.3.4 S (TL, ||) Clustering of rewired TFs

Based on the fraction of gained, lost, and retained edges with respect to the total number of edges for each TF, rewired TFs were clustered into three groups using Kmeans clustering. Hartigan-Wong algorithm with 10 iterations were used a K-means algorithm by Hartigan⁵⁸. Figure S 5-2 shows the clustering result for rewired TFs between K562 and GM12878. NFE2 and RCOR1 were identified as one of the strongest members of the gained group, CTCF was identified as a member of the common group, and YBX1 was identified as a member of loss group.

Figure S 5-2 (TL, ||) Kmeans clustering of rewired TFs in K562 and GM12878



5.4 S (TL, ||) Rewiring analysis based on mixed membership algorithm

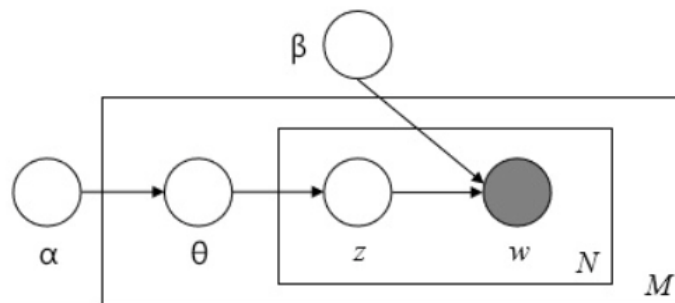
We used mixed membership algorithm to investigate the rewiring changes between GM12878 and K562 cell lines (Figure S 5-3). TF-target matrix ($M \times V$) is converted from enhancer and TSS regulatory network, where M is the number of TF and V is the number of unique target genes for all TFs. Each row represents a target gene of a TF $i=1,2,\dots, M$. The regulatory pattern of each TF is comprised of K latent communities. Each community includes contributions from N target gene and N varies for different TF.

The target gene of TF $w_i, \vec{w} = \langle w_{i,1}^v, w_{i,2}^v, \dots, w_{i,n}^v \rangle$ and $= 1$ means target, 0 means non-target. The observation denotes TF i , target gene j with status v . Similarly $Z_{i,j,v}$ is the community distribution of each target gene j for TF i with status v . $\beta(M \times V)$ denotes the probability of target gene j belong community k , which is parameter of multinomial distribution. θ_i each and denote the distribution of communities for TF i . $\theta \sim \text{Dirichlet}(\alpha)$, where α is the super-parameter of θ .

When inferring the latent gene community model, we are most interested in the communities' parameter β , the Dirichlet parameter α and the latent community distribution θ of TF. So, the key is to find the posterior distribution of latent variables.

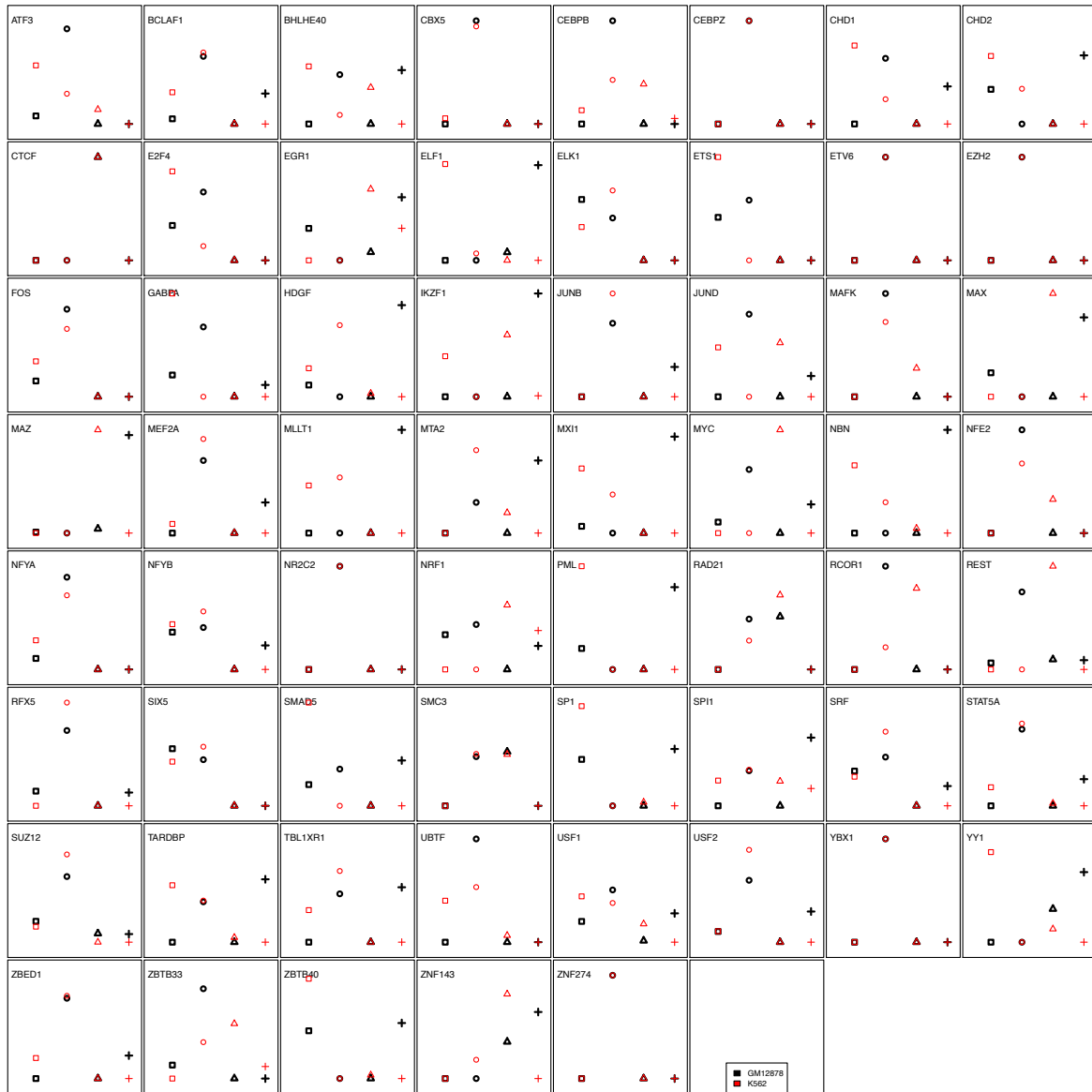
Variational EM algorithm (implemented using mixedMem R package) is used to infer the α and θ as described in Blei *et al*⁵⁹ However, computational benefits of EM lead to optimization uncertain and make it easily converge to local maxima. We have no prior knowledge for the θ and α , which is impossible to use near plausible value to find a reasonable optimum. To hack this, we

Figure S 5-3 (TL, ||) Schematic of gene community based rewiring analysis



repeat multiple times (100) and use the median of rewiring changes from all the non-early stops simulation to represent the most optimal regulatory changes of TF. One example of the θ distribution was given in Figure S 5-4.

Figure S 5-4 (TL, ||) Example of θ distribution difference in tumor and normal cell lines

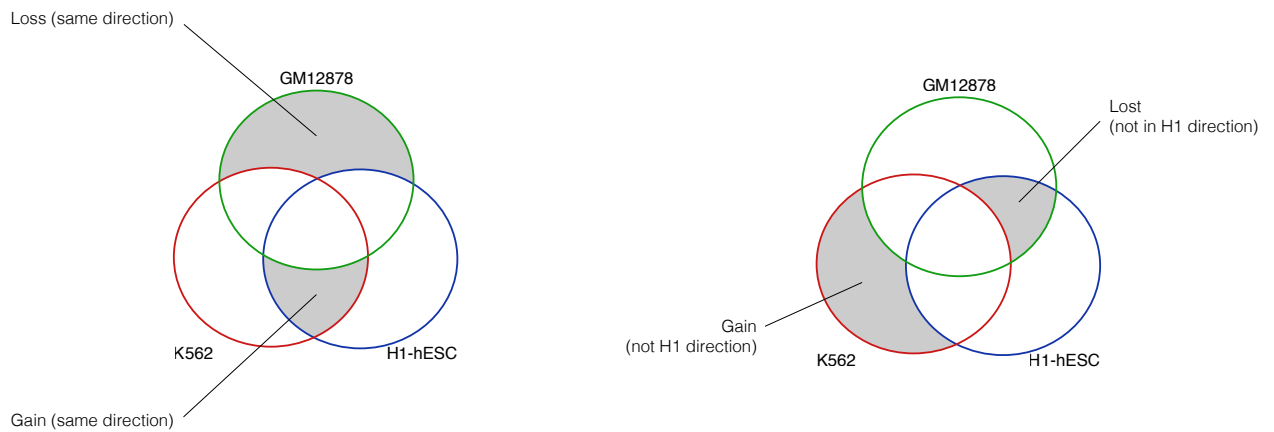


The rewiring of TF regulation is defined by the changes of distribution in K gene communities using $Distance_i = \sqrt[3]{\sum_{i,j} [\sqrt[3]{q_{K562,i,j}} - \sqrt[3]{q_{GM12878,i,j}}]**3}$, where q_i is the distribution of communities for TF i .

5.5 S (TL, ||) Rewiring analysis associated with H1-hESC

Rewired edges of tumor-normal TF network were compared to H1-hESC TF network to evaluate if the rewiring is in the direction favoring toward or moving away from stem cell-like transformation. In doing so, the target genes of gain and loss edges were sub-divided into target genes in the same direction as H1 or not (Figure S 5-5).

Figure S 5-5 (TL, ||) Comparison of rewiring direction with respect to H1-hESC



For K562-GM12878 network as an example, there were 25 TFs that were common among K562, GM12878, and H1-hESC. The following table (Table S 5-1) summarizes the rewired edges target genes in the same direction and overall evaluation of whether the rewiring is resembling H1 or not. About one third of MXI1 edges were rewiring in the same direction of H1, while rewired edges of REST were the most distant from H1.

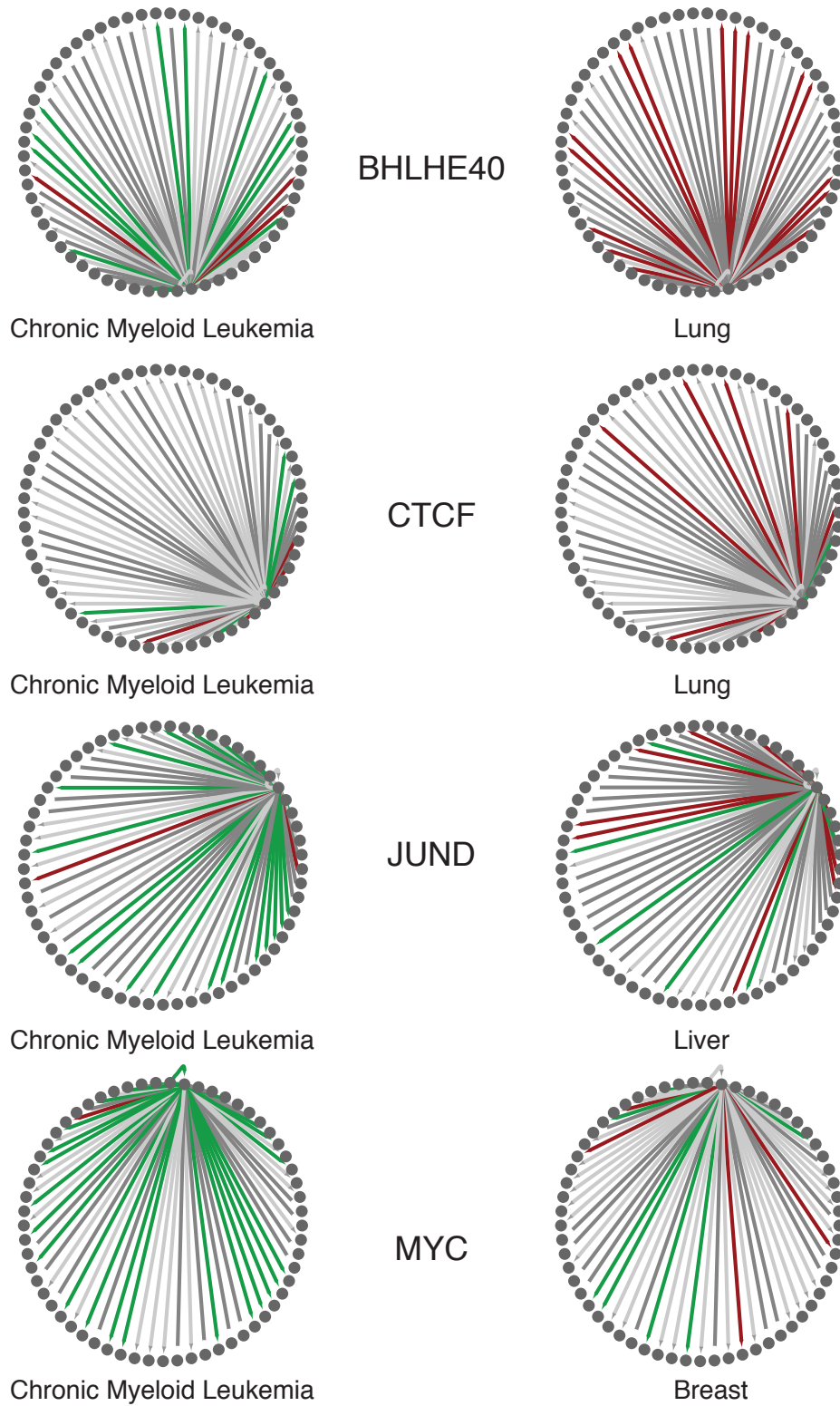
Table S 5-1 (TL, ||) Comparison of rewired edges between K562-GM12878 network with H1-hESC

TF	Toward H1 direction	Against H1 direction	Overall
MXI1	2478	1033	1445
ZNF143	2491	1131	1360
CHD2	2015	891	1124
SUZ12	1325	232	1093
SRF	1541	451	1090
RFX5	1353	360	993
YY1	1914	1023	891
USF2	1157	682	475
SIX5	716	249	467
RAD21	1193	1019	174
CTCF	1221	1060	161
EZH2	337	335	2
USF1	1053	1058	-5
SP1	1249	1475	-226
MAFK	663	1724	-1061
CHD1	982	2147	-1165
ATF3	883	2243	-1360
EGR1	985	2418	-1433
CEBPB	1167	2660	-1493
GABPA	930	2535	-1605
MAX	1055	2707	-1652
JUND	1248	4028	-2780
MYC	917	3788	-2871
NRF1	313	3978	-3665
REST	832	4868	-4036

5.6 S (TL, ||) Rewiring of TF across tumor types

Rewiring of several key TFs in leukemia (K562) were evaluated across lung (A549), liver (HepG2), and breast (MCF-7) cancer models. In some extreme cases, the overall direction of rewiring was reversed. For BHLHE40 in CML as an example, the direction of rewiring is mostly towards gaining patterns, whereas in lung adenocarcinoma, the edges were dominantly lost. For both JUND and MYC, the pattern of gain edges were consistently observed in liver or breast cancer samples.

Figure S 5-6 (TL, II) Rewiring of TF across tumor types



5.7 S (TL, ||) Patient survival analysis based on TF activities

To prioritize TF based on clinical values, patient survival analysis was performed on activity scores of TFs. This section was largely divided into two sections: first, we systemically surveyed TF activities on AML datasets and second, we focused on a specific TF's activity (MYC) to look at its target genes in both cancer and normal counterpart. TFs were prioritized based on their prognostic potential by performing survival analysis using TF activity scores as the primary predictor. This section is comprised of two primary analyses: 1. We systematically interrogated TF activity in several AML datasets and 2. Perform detailed analysis of MYC activity using MYC target genes specific to either cancer or non-cancer cell lines derived from the same tissue.

5.7.1 S (TL, ||) Systematic survival analysis of TFs on AML cohorts

In this analysis, we systematically calculated TF activity in 6 different AML datasets using the ENCODE ChIP-seq data. 292 ChIP-seq experiments from K562 (231 TFs) and 120 ChIP-seq experiments from GM12878 (101 TFs) were used to generate TF binding weight profiles from the TIP output. Specifically, the binding score of a TF to each gene (outputted by the TIP algorithm) was z-transformed and a one-sided z-test was carried out to generate p-values corresponding to each TF-gene binding interaction. P-values were $-\log_{10}$ -transformed and trimmed at -10 or 10. Weight profiles were re-scaled by subtracting each value in a TF weight profile by the minimum and dividing by the range so that all values fell between 0 and 1. These weight profiles were used as input into the BASE algorithm⁶⁰. The BASE algorithm takes in a single sorted (decreasing) patient's gene expression profile and calculates a running sum statistic by moving the down the profile and weighting each gene by its corresponding weight taken from the TF weight profile. This generates a foreground function. Similarly, a background function can be generated by repeating the process by multiplying by 1-weight instead of multiplying the gene by its weight. The maximum deviation between these two functions represents the TF activity score. This score is high when the highly-expressed genes in a patient's profile also tend to be bound tightly by the TF (as determined by the TF weight profile). It calculates TF activity scores for AML patient samples derived from the following gene expression datasets.

Table S 5-2 (TL, ||) Gene expression dataset of AML patients

Source	Accession	Author	Cohort
GEO	GSE37642 (GPL_96)	Herold	n=422
NCI caArray	willm-0019	Wilson	n=170
GEO	GSE14468	Wouters	n=526

Survival analysis was performed for each TF to identify those that were significantly associated with AML patient mortality. Namely, the TF's iRASs (activity scores) across patient samples were used as the independent variable in a Cox proportional hazards model. A hazard ratio <1 indicates that a TF's activity is associated with favorable prognosis and a hazard ratio of >1 indicates that a TF's activity is associated with unfavorable prognosis in AML patient samples. Since a separate model was fit to each TF's iRASs, p-values corresponding to the hazard ratios were adjusted for multiple hypothesis testing by using the Benjamini-Hochberg correction procedure.

In the results, we report the HR, P-value, and Adjusted P-value for each TF and their association with patient survival in each of the 3 AML gene expression datasets. The column labeled "number_datasets_significant_P005" indicates the number of datasets in which the TF's activity was observed to be significantly associated with AML patient prognosis at $P < 0.05$. In particular, EZH2, STAT1, and NR2C2 TFs were found to be significantly associated with prognosis in all 3 datasets. 15 other TFs were found to be significant in 2 datasets. Notably, IKZF1, a well-known oncogene in hematopoietic and lymphoid cancers, was found to be significantly associated with prognosis in 2 datasets with p-value of $9.7E-4$ and $1.9E-2$ in Herold and Wouters set, respectively. For more details, please refer to the supplementary datasheet for a complete list of TFs associated with patient prognosis.

5.7.2 S (HL, ||) TF specific survival analysis

For this analysis, we focused on the METABRIC breast cancer cohort⁶¹, which contains comprehensive survival information and gene expression profiles for 2,509 breast cancer patients. Using this dataset, we investigated the association between TF activity and disease-specific survival (DSS). Presumably, DSS provides stronger evidence compared to overall survival (OS) when evaluating whether some variable (TF activity) is associated with mortality from the actual disease of interest. In some cases, cancer patients die from some other co-morbid condition or the

cause of death is unclear. Unlike OS where any deaths are considered “events” in a survival analysis, DSS considers only deaths caused by cancer. In most cases, evaluating overall survival provides greater statistical power but may not be as accurate as disease-specific survival. Since the METABRIC dataset provides detailed survival information which includes DSS, we used this metric over OS. Please note that all target genes were defined as those with $p < 0.01$ from the TF TIP profile.

5.7.3 S (TL, ||) Survival analysis of MYC in breast cancer cohort:

5.7.3.1 S (TL, ||) TF-level analysis (cell-line specific):

To determine if MYC activity was associated with breast cancer patients’ survival, we utilized three separate MYC target gene sets to interrogate patient gene expression profiles derived from the METABRIC breast cancer gene expression compendia (n=1992).

First, based on ChIP-seq signal profiles, target genes of MYC were grouped into three categories; MCF-7 specific, MCF-10A specific, and common targets of the two cell lines. MYC activity as well as target genes from each of the three gene categories were calculated in each METABRIC breast cancer patient sample using BASE algorithm⁶⁰. Second, we extracted time-to-event (death from breast cancer) information from the patients’ metadata and correlated disease-specific patient survival with MYC activity score using univariate Cox regression models (proportional hazards).

An individual regression model was built for each MYC activity score corresponding to the three different gene sets. A positive association indicated that patients with high MYC activity exhibited longer survival compared to patients with low MYC activity and conversely, a negative association indicated that high MYC activity is associated with shorter patient survival time.

Figure S 5-7 (TL, II) Survival analysis on MYC's common target genes between MCF-7 and MCF-10A

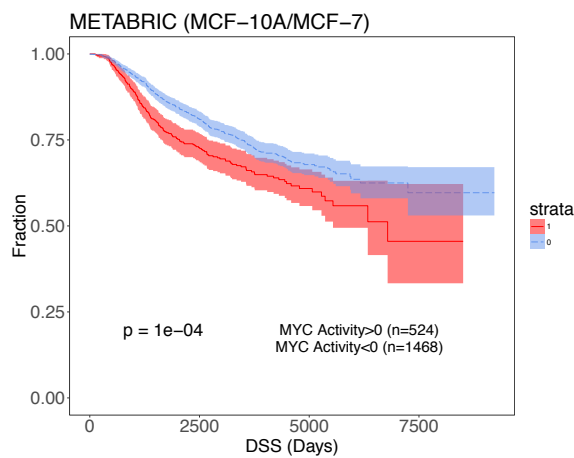


Figure S 5-8 (TL, II) Survival analysis on MYC's MCF-7 specific target genes

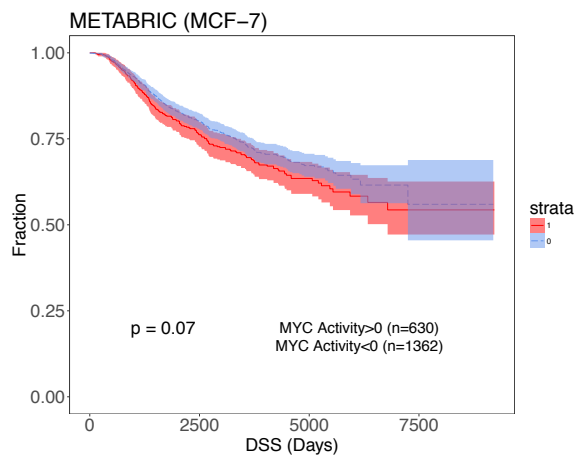


Figure S 5-9 (TL, II) Survival analysis on MYC's MCF-10A specific target genes

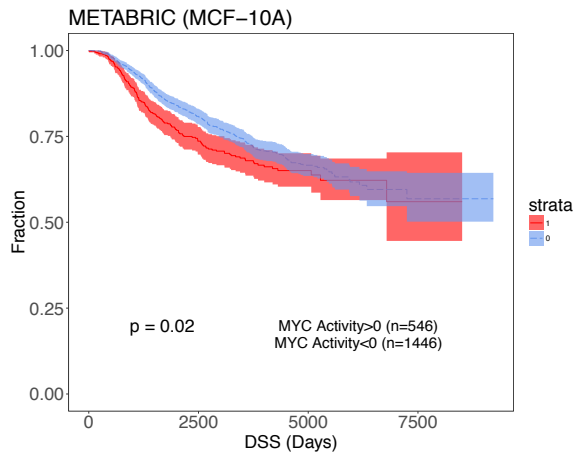
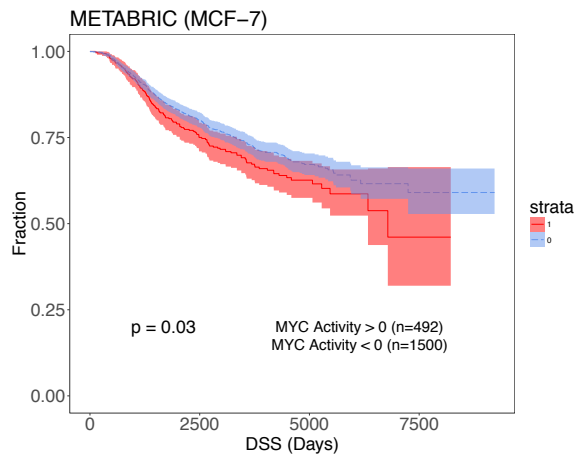
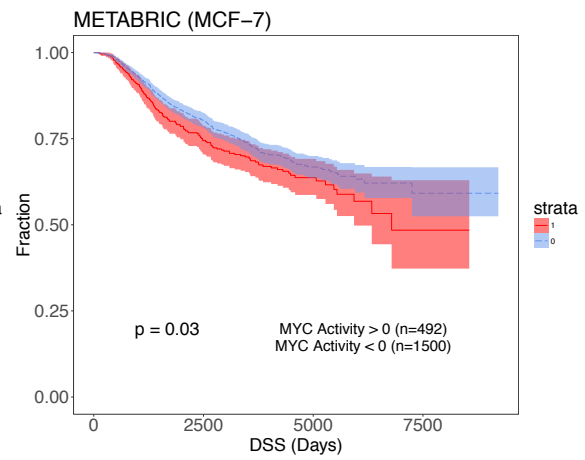
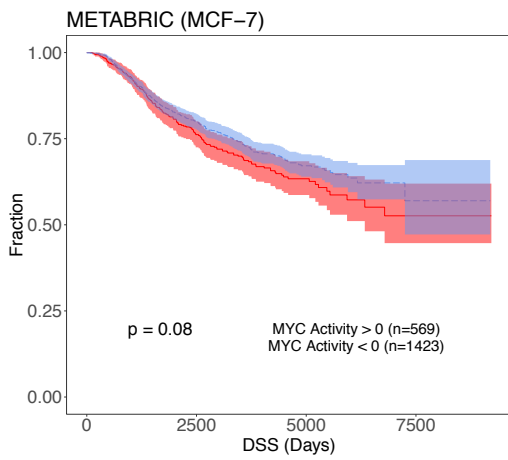


Figure S 5-10 (TL, II) Survival analysis on MYC's target gene expression levels in three replicates



5.7.3.2 S (HL, ||) TF-level analysis (MCF-7)

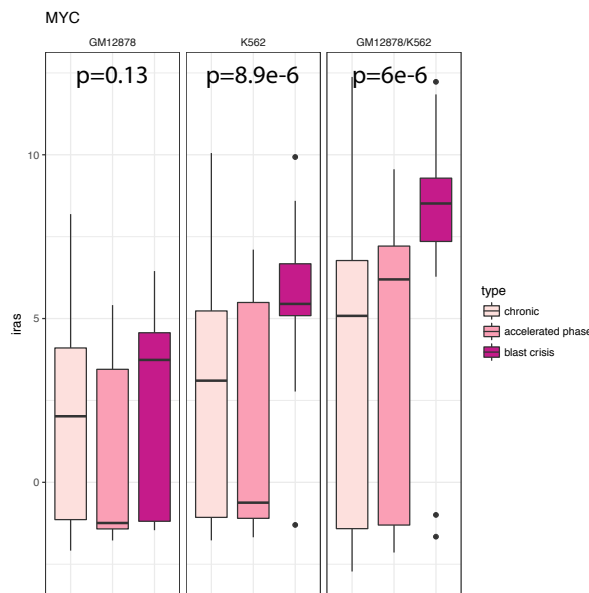
MYC activity survival analysis was also carried out focusing on the entire MYC binding profile in MCF-7 cell lines. Briefly, the p-values outputted by the TIP algorithm were transformed and used as weights as performed in the AML TF activity analysis. MYC activity levels were then used as the independent variable in a Cox regression model. This analysis was performed for three ENCODE replicates.

5.7.4 S (TL, ||) Association of MYC and patient severity in chronic myeloid leukemia

5.7.4.1 S (TL, ||) TF-level analysis

For the CML analysis, target genes of MYC were categorized as K562-specific or GM12878-specific. MYC activity was calculated in each CML patient sample belonging to the GSE4170 dataset using target genes from each of the three gene categories. MYC activity scores were then compared between three different severity levels (chronic, accelerated phase, and blast crisis) using ANOVA.

Figure S 5-11 (TL, ||) MYC activity scores were then compared between three different severity levels using ANOVA



5.8 S (TL, ||) Target gene analysis

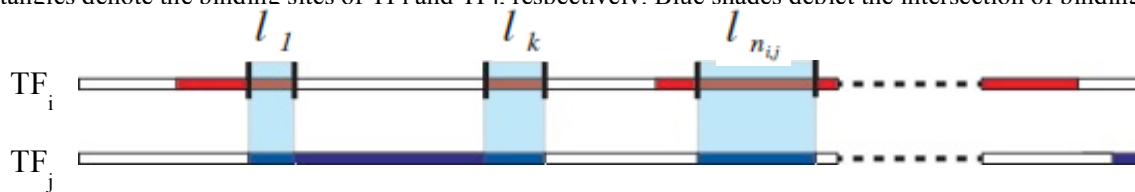
To evaluate the effect and extent of TF-gene network rewiring, target gene's expression and epigenetic changes were evaluated for genes that have gained and lost edges between normal and tumor samples. For expression, we used RESM quantification of ENCODE DCC uniformly processed long polyA RNA-seq and averaged TPM values over all available replicates. For DNase-seq, histone ChIP-seq, and methylation features, we further processed from fold enrichment signal tracks as follows. We averaged the fold enrichment signal across 200bp upstream and downstream of the unique TSS, the same canonical TSS site used define proximal TF-gene linkage. For all expression, DNase-seq, histone ChIP-seq, and methylation feature was expressed as a log₂ ratio between tumor to normal samples. To avoid division by zero error, a pseudo-count of 0.0001 was added to each feature.

5.9 S (TL, †) Co-binding analysis

A score for each transcription factor pair (i, j) is calculated based on the intersection of their binding sites. Let TF_i has n_i binding sites, each with a length of $l_{i,t}$. Using the intersect function of bedtools, we found $n_{i,j}$ intersecting binding sites, each with length l_k between TF_i and TF_j and calculated the co-binding score between TF_i and TF_j as;

$$c(i, j) = \frac{\sum_{k=1}^{n_{i,j}} l_k}{\sum_{t=1}^{n_i} l_{i,t}} \quad (3-2)$$

Figure S 5-12 (TL, †) Illustration of the binding sites and their length on both TF_i and TF_j . Red and blue rectangles denote the binding sites of TF_i and TF_j , respectively. Blue shades depict the intersection of binding



Please note that $c(i,j) \neq c(j,i)$, as the denominator is the total length of binding sites of TF_i . We calculated the co-binding scores for each transcription factor pair in both GM12878 and K562 cell lines. We then calculated the differences between the cell lines by subtracting the co-binding scores.

We found that among all common transcription factors of GM12878 and K562 cell lines, ZNF274 has a larger binding score in K562 cell line compared to in GM12878 cell line. ZNF274 has the highest difference in the co-binding score with 54 out of 68 transcription factor partners, with an average difference of 0.61. The average difference for co-binding scores for all transcription factor pairs is 0.02. This shows that co-binding of ZNF274 increased significantly in K562 cell lines.

Figure S 5-13 (TL, †) Co-binding scores $c(i,j)$ of the transcription factors both in GM12878 and K562 cell lines. Rows represent TF_i and columns represent TF_j . Red color indicates high co-binding score, where blue color indicates low co-binding scores.

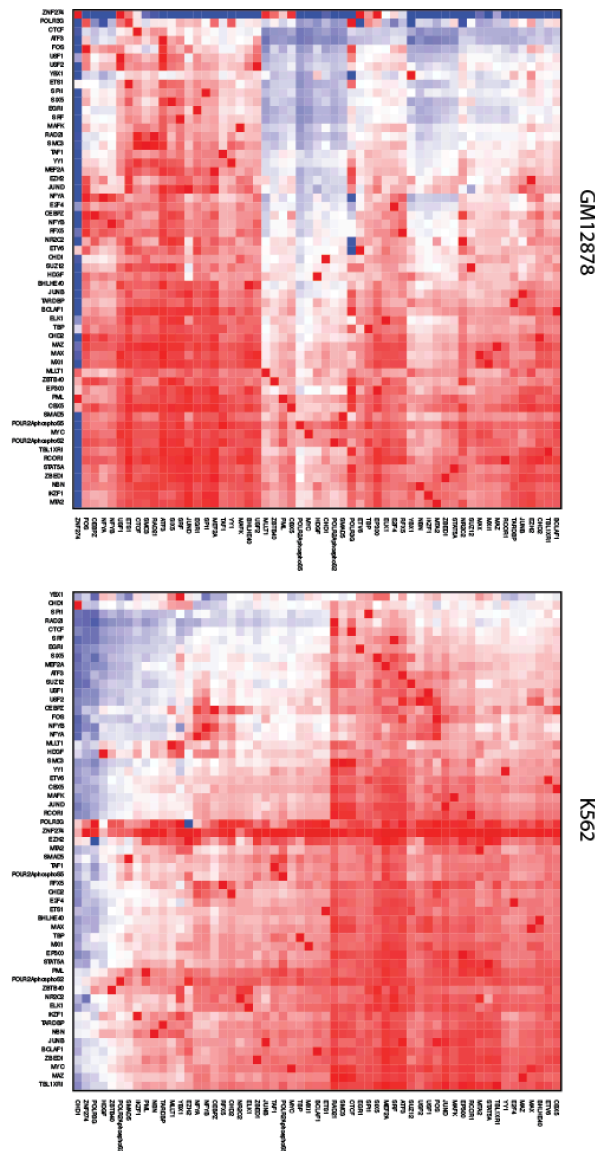
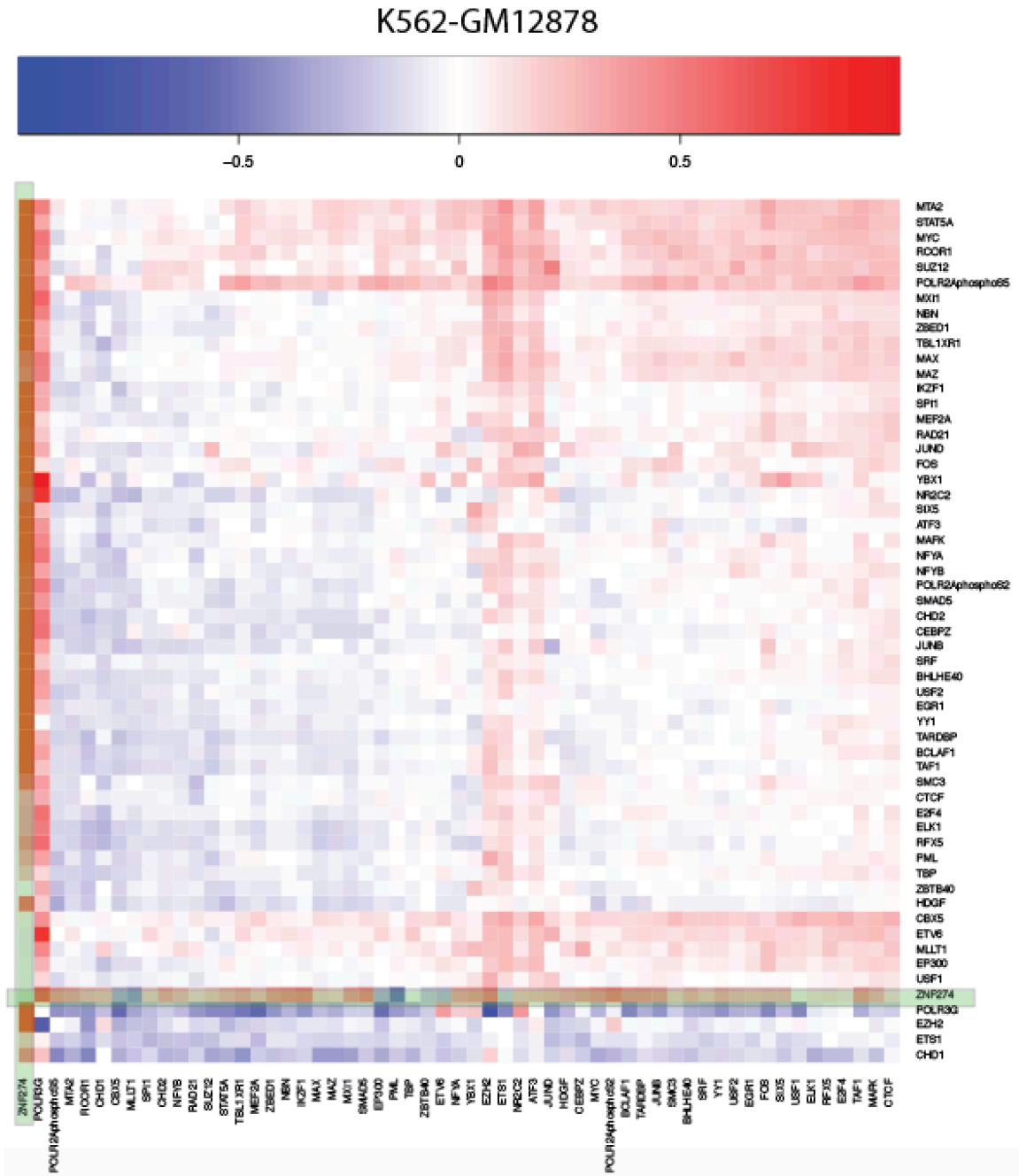


Figure S 5-14 (TL, †) Difference of co-binding scores $c(i,j)$ of the transcription factors between K562 and GM12878 cell lines. Rows represent TF_i and columns represent TF_j . ZNF274, which has consistently higher co-binding scores with other TFs in K562 cell line compared to GM12878 is highlighted.



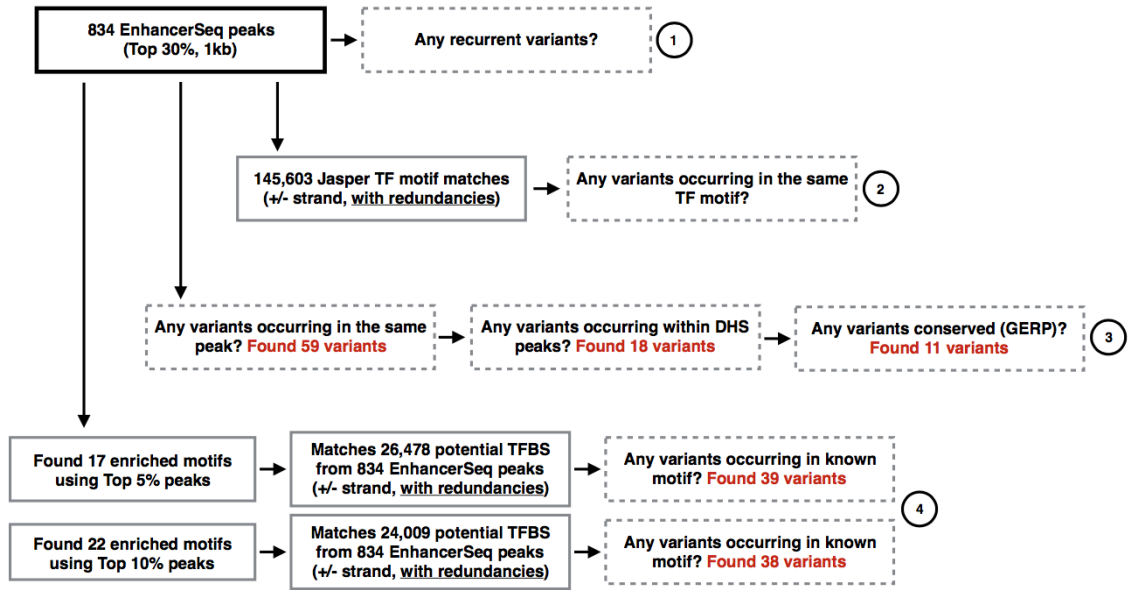
6 S (TL, ||) More details about “Step-wise prioritization scheme pinpoints deleterious SNVs in cancer” and “Small-scale validation experiments on prioritized genomic elements and variants”

The description of the regulatory network and mutation recurrence analysis provide a way to prioritize key genomic features associated with cancer. Here we proposed a step-wise scheme to prioritize the SNVs for small scale validations. First, we start by searching for key regulators that frequently rewired, locate in network hubs or on top of the network hierarchy, or significantly drive expression changes in cancer. We then prioritize functional elements that are associated with top regulators, undergo large regulatory and chromatin changes, or (most importantly) are highly mutated in tumors. Finally, on a nucleotide level, we can pinpoint impactful SNVs for small-scale functional characterization by their ability to disrupt or create specific binding sites, or which occur in positions of particularly high conservation or chromatin changes.

6.1 S (TL, †) Motif analysis using MotifTools (D-score)

To prioritize the variant within high-confidence enhancer sets, we first searched for recurrent non-coding variants or multiple non-coding variants occurring in a known TF motif. However, we could not find any somatic variants that are either recurrent or recurrent within a TF motif.

Figure S 6-1 (TL, †) Variant prioritization scheme based on STARR-seq



1. Recurrent BRCA non-coding variants within 834 EnhancerSeq peaks => **None**
2. Multiple BRCA non-coding variants occurring in a known TF motif => **None**
3. Multiple BRCA non-coding variants occurring in a EnhancerSeq peak (834) => **59 non-coding variants**
4. BRCA variants in known TF motif with motif breaking power. Same type of analysis was done for E2 induced MCF-7 as well. Combining results from “untreated” and “E2 induced”, **46 variants**

Alternatively, we prioritized somatic variants based on its motif breaking power, or D-score, where D stands for disruptive-ness or deleterious-ness. Motif disruption score was calculated based on the difference between sequence specificities of reference to alternative sequence.

$$\text{motif-score}_{\text{ref}} = -10 \cdot \log_{10}(\text{p-value}_{\text{ref}})$$

$$\text{motif-score}_{\text{alt}} = -10 \cdot \log_{10}(\text{p-value}_{\text{alt}})$$

$$\text{D-score (Disruptive-ness or Deleterious-ness)} \quad (6-1)$$

$$= \text{motif-score}_{\text{ref}} - \text{motif-score}_{\text{alt}}$$

$$= -10 \cdot \log_{10} \left(\frac{\text{p-value}_{\text{ref}}}{\text{p-value}_{\text{alt}}} \right)$$

A positive D-score denotes a variant that decreases the likelihood that a TF will bind the motif (motif-break), and negative D-score denotes a variant that increases the likelihood that a TF will bind the motif (motif-gain). For assessing D-score, uniform nucleotide background was assumed (A:C:G:T=1:1:1:1), and the p-value threshold of 1e-3 was used. For position weight matrix (PWM), JASPAR TF profiles (2016 core non-redundant vertebrates, http://jaspar.genereg.net/html/DOWNLOAD/JASPAR_CORE/pfm/nonredundant/pfm Vertebrates.txt) were used, and variants that affect multiple TF binding profiles were averaged over all D-scores. More details about the tool and code can be found at <https://github.com/hoondy/MotifTools>. Somatic variants were further prioritized using conservation score (high positive GERP score).

Figure S 6-2 (TL, †) Schematic of Motiftool output

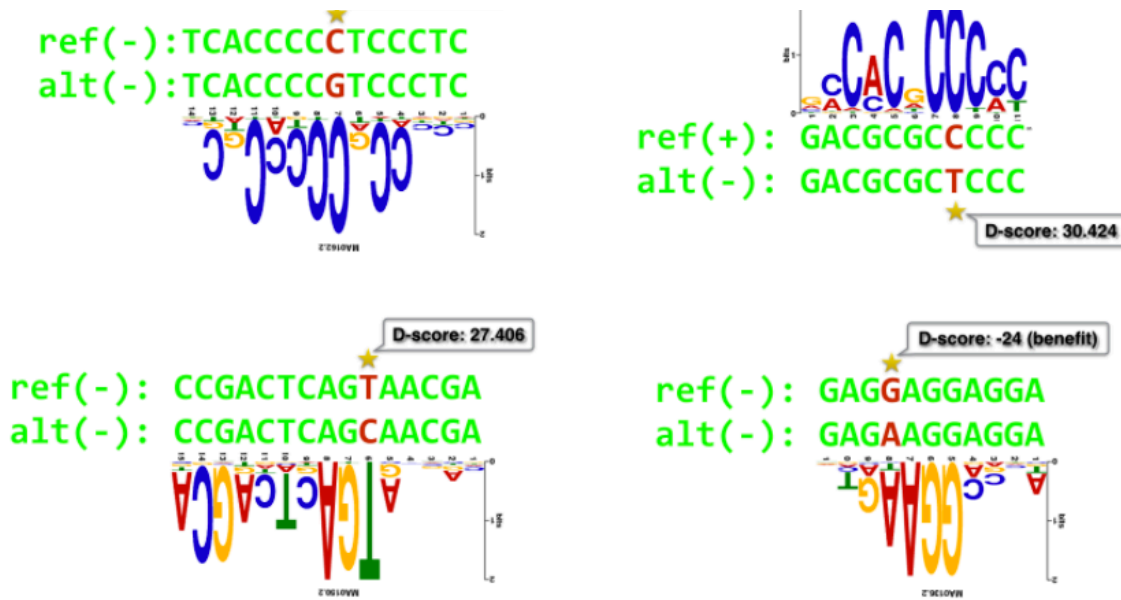


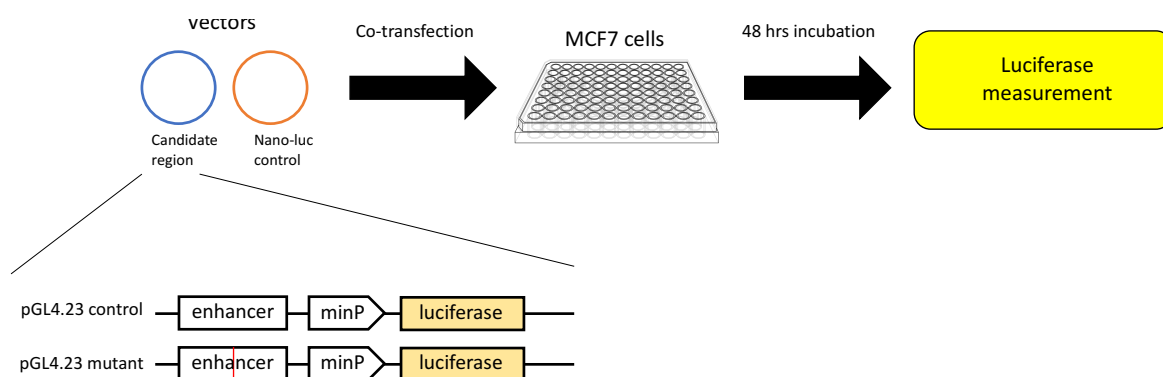
Table S 6-1 (TL, †) Validated mutations in MCF-7 and luciferase assay tested region

6.2 S (TL, ||) Experiment Details about SNV validation

SAMPLE	CHR	POS	REF	ALT	TEST_START	TEST_END	NOTE
Sample01	chr16	85604242	C	G	85603992	85604491	issue with plasmid isolation
Sample02	chr21	27541982	G	A	27541732	27542231	
Sample03	chr8	21541726	A	G	21541476	21541975	issue with plasmid isolation
Sample04	chr17	38474408	C	G	38474158	38474657	
Sample05	chr20	43971343	G	C	43971093	43971592	
Sample06	chr7	1598567	C	T	1598317	1598816	
Sample07	chr20	58563412	C	T	58563162	58563661	
Sample08	chr7	150759483	C	G	150759233	150759732	
Sample09	chr7	5596005	T	G	5595755	5596254	
Sample10	chr6	134700462	G	T	134700212	134700711	

Each regulatory region (both wild and mutant types) was separately synthesized. Enhancer regions were designed in such a fashion where based on the candidate SNV site, 250bp upstream and 250bp downstream was included for each enhancer region. These regions were then cloned into the pGL4.23[luc2/minP] vector (Promega, Cat# E841A). Each candidate region was placed upstream of the minP promoter to determine the effect of each putative enhancer region on luciferase expression. 100ng of each candidate construct and 100ng of Nano-luc control was co-transfected into MCF-7 cells (5,000 cells per well in DMEM media containing 10% FBS and 1% Penicillin-Streptomycin antibiotic) using the Lipofectamine 3000 reagent (Thermo Fisher, Cat# L3000001) according to manufacturer's instructions. Cells were incubated for 48 hrs before reading the luciferase signal using Promega Nano-Glo luciferase kit (Promega, Cat# N1521) according to manufacturer's instructions.

Figure S 6-3 (TL, ||) Schematic of SNV validation



The raw data of the experiment have been listed in Table S 6-2 and Table S 6-3.

Table S 6-2 (TL, ||) Details of SNV replication technical replicate 1

	Normal Rep 1	Normal Rep 2	Normal Rep 3	Mutant Rep 1	Mutant Rep 2	Mutant Rep 3
Background	831	388	416	2623	1296	1065
2	7698	5193	6893	161889	132344	179837
4	587863	778963	603304	465322	408546	460135
5	10281	16083	17192	40103	63770	48912
6	39090	20019	23419	7614	6760	4959
7	15039	18873	13468	57945	47666	59931
8	117702	115358	150245	189131	295907	247173
9	26775	30804	34042	58424	104433	27587
10	21705	22249	17162	107077	31005	76174
Empty	61423	87225	46835	774	789	1111
Background	562	1461	748	4582	967	473
Background	238	500	395	857	635	921

Table S 6-3 (TL, ||) Details of SNV replication technical replicate 2

	Mutant Rep 1	Mutant Rep 2	Mutant Rep 3	Normal Rep 1	Normal Rep 2	Normal Rep 3
Background	11852	13823	14402	15111	13245	9858
2	1922952	1854116	1882977	2326518	1637299	1927383
4	1969924	1947206	2088052	1606057	1133593	1246025
5	1396532	1408962	1879464	2110566	1890350	1594218

6	1756884	1798060	1859447	1825321	1597249	1658538
7	1884514	2197614	2393865	2124074	1385636	1888050
8	1695866	1711603	1488882	2405882	1487463	1516048
9	1715909	1943040	1916404	2058790	1385673	1241105
10	1771446	1498757	2030086	1736458	985080	1237019
Empty	2575562	2699389	2494020	22537	10758	6625
Background	12437	14855	12235	7338	4629	2613
Background	3835	4041	4182	2990	1698	1009

6.3 S (TL, ||) Details about siRNA RNA-Seq experiments

MCF-7 cells were seeded at an initial density of 2×10^5 cells at basal media conditions (DMEM media supplemented with 10% FBS and 1% penicillin/streptomycin). After 24 hours, cells were transfected with siRNA control (Santa Cruz, Cat#: sc-37007) or siRNA targeting MYC (Santa Cruz, Cat# sc-29226) using the Viafect reagent (Promega, Cat#: E4981) in biological triplicate according to manufacturer's instructions. Cells were harvested 72 hours later using Trizol Reagent (Thermo Fisher, Cat#: 15596026) and RNA was isolated using the Direct-zol RNA Miniprep Plus kit (Zymo Research, Cat#: R2072). RNA-seq libraries were prepared using the TruSeq Stranded Total RNA Library Prep Kit (Illumina, Cat#: RS-122-2201). RNA-seq library quality was assessed using Bioanalyzer and Qubit analysis before subjected to deep sequencing on the HiSeq 4000.

We used RNA-STAR (version 2.3.0) to map the reads to hg19 genome with gencode v19 as annotation input for junction mapping. Default settings were used for the read mapping. After mapping, we used Cufflinks (version 2.0.2) for the gene and transcription level quantifications for both knockdown and control experiments.

7 S (TL, #) EN-CODEC resource accessibility

All of EN-CODEC resources are available to download as flat files or tarballs from our website <http://encodec.encodeproject.org>. All resource files follow the uniform naming convention as follows:

EC-XXX-YYY.fileDescription

Table S 7-1 (TL, #) Naming convention - primary category

XXX	description
001	Data Provision
002	Annotation
003	Processed Data (Analysis)
004	Experimental Validation
005	Software

Table S 7-2 (TL, #) Naming convention - secondary category

YYY	description
MET	Meta information (data summary)
CRE	Cis-regulatory elements (enhancer, promoter)

DBP	DNA-binding proteins (TF, histone) related
RBP	RNA-binding proteins (RBP) related
BMR	Background mutation rate (BMR) related
NET	Network related
EXT	Extended gene
COH	Cohort
ETC	Others

7.1 S (TL, †) Data Provision

7.1.1 S (TL,†) Deduplicated ENCODE assays

List of all EN-CODEC experiments (inc. external data)

- EC-001-MET.encodec_all_experiments.csv

TF ChIP-seq data summary (Oct 2017 freeze)

- EC-001-MET.encodec_Oct17_TF_ChIP-seq_data.csv

Deduplicated ChIP-seq list (Oct 2017 freeze)

- EC-001-MET.encodec_Oct17_deduplicated_ChIP-seq_list.csv

Decuplicated ChIP-seq matrix (Oct 2017 freeze)

- EC-001-MET.encodec_Oct17_deduplicated_ChIP-seq_matrix.csv

ENCODE key cell line ChIP-seq summary

- EC-001-MET.encode_key_cell_line_ChIP-seq_data.csv

7.1.2 S (TL, ‡) Variant calls of liver cancer patients

- EC-001-COH.LIHC-Germline.txt
- EC-001-COH.LIHC-Somatic.txt

7.1.3 S (TL, ‡) Normalized cancer patient expression data

- EC-001-COH.TCGA_data_2016_01_28.tar.gz

7.2 S (TL, ‡) Annotation

7.2.1 S (TL, ‡) ENCODE cancer annotations

ENCODE cancer sample summary

- EC-002-MET.encode_cancer_cell_type_summary.csv
- EC-002-MET.encode_cancer_cell_line_summary.csv

7.2.2 S (TL, ‡) TF and RBP annotations

K562 vs GM12878 common TF summary

- EC-002-MET.encodec_KG_common_TF_summary.csv

K562 vs GM12878 common TF classification

- EC-002-MET.encodec_KG_common_TF_class.csv

TF annotations

- EC-002-DBP.TF_annotation.txt

RBP annotations

- EC-002-RBP-RBP_annotation.txt

7.2.3 S (TL, ‡) Extended Gene

List of all extended gene definitions in major cell types

- EC-002-EXT.merge.post.extendedGene.K562.txt

- EC-002-EXT.merge.post.extendedGene.MCF-7.txt
- EC-002-EXT.merge.post.extendedGene.HepG2.txt

7.3 S (TL, #) Processed Data (Analysis)

7.3.1 S (TL, #) Cis-regulatory element related

7.3.1.1 S (TL, #) CASPER

List of all CASPER results in major cell types

- EC-003-CRE.CASPER_K562.bed
- EC-003-CRE.CASPER_HepG2.bed
- EC-003-CRE.CASPER_GM12878.bed
- EC-003-CRE.CASPER_MCF-7.bed
- EC-003-CRE.CASPER_A549.bed
- EC-003-CRE.CASPER_HeLa-S3.bed
- EC-003-CRE.CASPER_H1-hESC.bed
- EC-003-CRE.CASPER-merged_K562.bed
- EC-003-CRE.CASPER-merged_HepG2.bed
- EC-003-CRE.CASPER-merged_GM12878.bed
- EC-003-CRE.CASPER-merged_MCF-7.bed
- EC-003-CRE.CASPER-merged_A549.bed
- EC-003-CRE.CASPER-merged_HeLa-S3.bed
- EC-003-CRE.CASPER-merged_H1-hESC.bed

7.3.1.2 S (TL, #) ESCAPE

List of all ESCAPE results in major cell types

- EC-003-CRE.ESCAPE_K562.bed
- EC-003-CRE.ESCAPE_GM12878.bed
- EC-003-CRE.ESCAPE_MCF-7.bed

7.3.1.3 S (TL, #) JEME (enhancer target gene prediction)

List of all JEME results of CASPER predictions in major cell types

- EC-003-CRE.JEME_of_CASPER_K562.bed
- EC-003-CRE.JEME_of_CASPER_HepG2.bed
- EC-003-CRE.JEME_of_CASPER_GM12878.bed
- EC-003-CRE.JEME_of_CASPER_MCF-7.bed
- EC-003-CRE.JEME_of_CASPER_A549.bed
- EC-003-CRE.JEME_of_CASPER_HeLa-S3.bed
- EC-003-CRE.JEME_of_CASPER_H1-hESC.bed

7.3.1.4 S (TL, #) CRE integration and compact annotation

Integrative enhancer annotation with the encyclopedia cRE accession

- EC-003-CRE.CASPERxESCAPE_GM12878.bed
- EC-003-CRE.CASPERxESCAPE_K562.bed

List of all Hi-C filtered JEME predictions in major cell types

- EC-003-CRE.JEME_of_CASPER_K562_FitHiC.bed
- EC-003-CRE.JEME_of_CASPER_GM12878_FitHiC.bed
- EC-003-CRE.CASPERxESCAPExJEME-
targetGene_FitHiC_GM12878_merged.bed
- EC-003-CRE.CASPERxESCAPExJEME-
targetGene_FitHiC_K562_merged.bed

Integrative “compact” enhancer annotation

- EC-003-CRE.hg19-cRExCASPERxJEME_Hi-C_GM12878_merged.bed
- EC-003-CRE.hg19-cRExCASPERxJEME_Hi-C_K562_merged.bed

7.3.2 S (TL, #) BMR related

7.3.2.1 S (TL, #) Covariate matrix

- EC-003-BMR.covariate_region_1mb.txt
- EC-003-BMR.covariate_region_100kb.txt
- EC-003-BMR.blacklist_region.txt
- EC-003-BMR.feature_details.txt

7.3.2.2 S (TL, #) BMR estimation

- EC-003-BMR.LiverCan_mu_nb.txt
- EC-003-BMR.LiverCan_theta_nb.txt
- EC-003-BMR.LiverCan_mu_pois.txt
- EC-003-BMR.LiverCan_dispersion.txt
- EC-003-BMR.BreastCan_mu_nb.txt
- EC-003-BMR.BreastCan_theta_nb.txt
- EC-003-BMR.BreastCan_mu_pois.txt
- EC-003-BMR.BreastCan_dispersion.txt
- EC-003-BMR.BloodCan_mu_nb.txt
- EC-003-BMR.BloodCan_theta_nb.txt
- EC-003-BMR.BloodCan_mu_pois.txt
- EC-003-BMR.BloodCan_dispersion.txt
- EC-003-BMR.LungCan_mu_nb.txt
- EC-003-BMR.LungCan_theta_nb.txt
- EC-003-BMR.LungCan_mu_pois.txt
- EC-003-BMR.LungCan_dispersion.txt
- EC-003-BMR.README.txt

7.3.2.3 S (TL, #) P-values for extended genes

- EC-003-EXT.pval_K562.tar.gz
- EC-003-EXT.pval_MCF-7.txt

- EC-003-EXT.pval_HepG2.txt
- EC-003-EXT.pval_A549.txt

7.3.3 S (TL, #) Network related

7.3.3.1 S (TL, #) Cell-type specific network

Proximal TIP-based network

- EC-003-NET.ENCODE_TIP_Profiles_693.txt
- EC-003-NET.edgeList_TIP_GM12878.tsv
- EC-003-NET.edgeList_TIP_K562.tsv

Proximal TSS-based network, using all TSS annotations

- EC-003-NET.edgeList_TSS_GM12878.tsv
- EC-003-NET.edgeList_TSS_K562.tsv

Proximal TSS-based network, using 1 TSS annotation per gene

- EC-003-NET.edgeList_uniqTSS2500_A549.tsv
- EC-003-NET.edgeList_uniqTSS2500_GM12878.tsv
- EC-003-NET.edgeList_uniqTSS2500_H1-hESC.tsv
- EC-003-NET.edgeList_uniqTSS2500_HeLa-S3.tsv
- EC-003-NET.edgeList_uniqTSS2500_HepG2.tsv
- EC-003-NET.edgeList_uniqTSS2500_IMR-90.tsv
- EC-003-NET.edgeList_uniqTSS2500_K562.tsv
- EC-003-NET.edgeList_uniqTSS2500_MCF-10A.tsv
- EC-003-NET.edgeList_uniqTSS2500_MCF-7.tsv
- EC-003-NET.edgeList_uniqTSS2500_liver.tsv
- EC-003-NET.edgeList_uniqTSS2500_lung.tsv

Distal enhancer-based network

- EC-003-NET.edgeList_ENH_GM12878.tsv
- EC-003-NET.edgeList_ENH_K562.tsv

Probability-based network

- EC-003-NET.probNet_README.txt
- EC-003-NET.probNet_TF.txt
- EC-003-NET.probNet_RBP.txt

7.3.3.2 S (TL, #) Reconciled merged network

Proximal TSS-based merged network

- EC-003-NET.mergedNet_uniqTSS2500_ALL.tsv

Proximal TIP-based merged network

- EC-003-NET.mergedNet_TIP_FDR_0.1.tsv

7.3.3.3 S (TL, #) Network hierachy

- EC-003-NET.hierarchy_mergedNet_README.txt
- EC-003-NET.hierarchy_mergedNet_TFss.merged.TIP.network.txt
- EC-003-NET.hierarchy_mergedNet_tval.mean.across.patients.txt
- EC-003-NET.hierarchy_cellTypeSpecNet_README.txt
- EC-003-NET.hierarchy_cellTypeSpecNet_GM12878.tfcom.ss.txt
- EC-003-NET.hierarchy_cellTypeSpecNet_K562.tfcom.ss.txt
- EC-003-NET.hierarchy_cellTypeSpecNet_node.properties.txt

7.3.4 S (TL, #) TF & RBP regulatory score in multiple cancer types

- EC-003-DBP.regulatoryScore_README.txt
- EC-003-DBP.regulatoryScore.tar.gz
- EC-003-RBP_regulatoryScore.tar.gz

7.3.5 S (TL, #) Network rewiring and rewiring index

K562 vs GM12878 proximal-distal combined TF-GENE network rewiring

- EC-003-NET.KG_TIP_ENH_mnet.csv
- EC-003-NET.KG_TSS_ENH_mnet.csv

K562 vs GM12878 proximal-distal combined TF-TF network rewiring

- EC-003-NET.KG_TIP_ENH_tfnet.csv
- EC-003-NET.KG_TSS_ENH_tfnet.csv

TF attributes

- EC-003-NET.KG_TIP_ENH_TFattrib.csv
- EC-003-NET.KG_TSS_ENH_TFattrib.csv

GENE attributes

- EC-003-NET.KG_TIP_ENH_GENEattrib.csv
- EC-003-NET.KG_TSS_ENH_GENEattrib.csv

K562 vs GM12878 network rewiring index

- EC-003-NET.KG_rewiringIndex_TIP+ENH.csv
- EC-003-NET.KG_rewiringIndex_TSS+ENH.csv
- EC-003-NET.KG_rewiringIndex-geneCommunity_TFrاند_mixedM_median_cubicroot.txt
- EC-003-NET.KG_rewiringIndex-geneCommunity_TFrاند_mixedM_median.txt

7.4 S (TL, †) Experimental Validation

7.4.1 S (TL, †) Luciferase assay related

Details about the validation regions and the results

- EC-004-CRE.luciferase_raw.csv
- EC-004-CRE.luciferase_normalized.csv

7.4.2 S (TL, †) MYC knockdown experiments

Details about the knockdown experiments

- EC-004-DBP.README.txt
- EC-004-DBP.MYC-KD_geneFPKM_target.txt
- EC-004-DBP.MYC-KD_geneFPKM_knockdown.txt

7.5 S (TL, †) Code Release

- EC-005-MET.README.txt
- EC-005-BMR.BMR_related.tar.gz
- EC-005-CRE.ESCAPE_related.tar.gz
- EC-005-NET.Rewiring_directConnection_related.tar.gz
- EC-005-NET.Rewiring_geneCommunity_related.tar.gz

References

- 1 Greenbaum, D., Rozowsky, J., Stodden, V. & Gerstein, M. Structuring supplemental materials in support of reproducibility. *Genome Biol* **18**, 64, doi:10.1186/s13059-017-1205-3 (2017).
- 2 Bamford, S. *et al.* The COSMIC (Catalogue of Somatic Mutations in Cancer) database and website. *Br J Cancer* **91**, 355-358, doi:10.1038/sj.bjc.6601894 (2004).
- 3 Vogelstein, B. *et al.* Cancer genome landscapes. *Science* **339**, 1546-1558, doi:10.1126/science.1235122 (2013).
- 4 Masoudi-Nejad, A., Goto, S., Endo, T. R. & Kanehisa, M. KEGG bioinformatics resource for plant genomics research. *Methods Mol Biol* **406**, 437-458 (2007).
- 5 Grosveld, G. *et al.* The chronic myelocytic cell line K562 contains a breakpoint in bcr and produces a chimeric bcr/c-abl transcript. *Mol Cell Biol* **6**, 607-616 (1986).
- 6 Salesse, S. & Verfaillie, C. M. BCR/ABL: from molecular mechanisms of leukemia induction to treatment of chronic myelogenous leukemia. *Oncogene* **21**, 8547-8559, doi:10.1038/sj.onc.1206082 (2002).
- 7 Lee, A. V., Oesterreich, S. & Davidson, N. E. MCF-7 cells--changing the course of breast cancer research and care for 45 years. *J Natl Cancer Inst* **107**, doi:10.1093/jnci/djv073 (2015).
- 8 Soule, H. D., Vazquez, J., Long, A., Albert, S. & Brennan, M. A human cell line from a pleural effusion derived from a breast carcinoma. *J Natl Cancer Inst* **51**, 1409-1416 (1973).
- 9 Keydar, I. *et al.* Establishment and characterization of a cell line of human breast carcinoma origin. *Eur J Cancer* **15**, 659-670 (1979).
- 10 Wosikowski, K. *et al.* Normal p53 status and function despite the development of drug resistance in human breast cancer cells. *Cell Growth Differ* **6**, 1395-1403 (1995).
- 11 Qu, Y. *et al.* Evaluation of MCF10A as a Reliable Model for Normal Human Mammary Epithelial Cells. *PLoS One* **10**, e0131285, doi:10.1371/journal.pone.0131285 (2015).
- 12 Soule, H. D. *et al.* Isolation and characterization of a spontaneously immortalized human breast epithelial cell line, MCF-10. *Cancer Res* **50**, 6075-6086 (1990).
- 13 Geltmeier, A. *et al.* Characterization of Dynamic Behaviour of MCF7 and MCF10A Cells in Ultrasonic Field Using Modal and Harmonic Analyses. *PLoS One* **10**, e0134999, doi:10.1371/journal.pone.0134999 (2015).
- 14 Thompson, E. A. *et al.* Differential response of MCF7, MDA-MB-231, and MCF 10A cells to hyperthermia, silver nanoparticles and silver nanoparticle-induced photothermal therapy. *Int J Hyperthermia* **30**, 312-323, doi:10.3109/02656736.2014.936051 (2014).
- 15 Tarangelo, A. & Dixon, S. J. Nanomedicine: An iron age for cancer therapy. *Nat Nanotechnol* **11**, 921-922, doi:10.1038/nnano.2016.199 (2016).

- 16 Savanur, M. A. *et al.* Sclerotium rolfsii lectin induces stronger inhibition of proliferation in human breast cancer cells than normal human mammary epithelial cells by induction of cell apoptosis. *PLoS One* **9**, e110107, doi:10.1371/journal.pone.0110107 (2014).
- 17 Bertram, C. & Hass, R. MMP-7 is involved in the aging of primary human mammary epithelial cells (HMEC). *Exp Gerontol* **43**, 209-217, doi:10.1016/j.exger.2007.11.007 (2008).
- 18 Dutta, S., Warshall, C., Bandyopadhyay, C., Dutta, D. & Chandran, B. Interactions between exosomes from breast cancer cells and primary mammary epithelial cells leads to generation of reactive oxygen species which induce DNA damage response, stabilization of p53 and autophagy in epithelial cells. *PLoS One* **9**, e97580, doi:10.1371/journal.pone.0097580 (2014).
- 19 Foster, K. A., Oster, C. G., Mayer, M. M., Avery, M. L. & Audus, K. L. Characterization of the A549 cell line as a type II pulmonary epithelial cell model for drug metabolism. *Exp Cell Res* **243**, 359-366, doi:10.1006/excr.1998.4172 (1998).
- 20 Nichols, W. W. *et al.* Characterization of a new human diploid cell strain, IMR-90. *Science* **196**, 60-63 (1977).
- 21 Fischer, K. R. *et al.* Epithelial-to-mesenchymal transition is not required for lung metastasis but contributes to chemoresistance. *Nature* **527**, 472-476, doi:10.1038/nature15748 (2015).
- 22 Thiery, J. P. Epithelial-mesenchymal transitions in tumour progression. *Nat Rev Cancer* **2**, 442-454, doi:10.1038/nrc822 (2002).
- 23 Horster, M. F., Braun, G. S. & Huber, S. M. Embryonic renal epithelia: induction, nephrogenesis, and cell differentiation. *Physiol Rev* **79**, 1157-1191 (1999).
- 24 Aokage, K. *et al.* Dynamic molecular changes associated with epithelial-mesenchymal transition and subsequent mesenchymal-epithelial transition in the early phase of metastatic tumor formation. *Int J Cancer* **128**, 1585-1595, doi:10.1002/ijc.25500 (2011).
- 25 Gregory, P. A. *et al.* The miR-200 family and miR-205 regulate epithelial to mesenchymal transition by targeting ZEB1 and SIP1. *Nat Cell Biol* **10**, 593-601, doi:10.1038/ncb1722 (2008).
- 26 Gibbons, D. L. *et al.* Contextual extracellular cues promote tumor cell EMT and metastasis by regulating miR-200 family expression. *Genes Dev* **23**, 2140-2151, doi:10.1101/gad.1820209 (2009).
- 27 Soltermann, A. *et al.* Prognostic significance of epithelial-mesenchymal and mesenchymal-epithelial transition protein expression in non-small cell lung cancer. *Clin Cancer Res* **14**, 7430-7437, doi:10.1158/1078-0432.CCR-08-0935 (2008).
- 28 Rho, J. K. *et al.* Epithelial to mesenchymal transition derived from repeated exposure to gefitinib determines the sensitivity to EGFR inhibitors in A549, a non-small cell lung cancer cell line. *Lung Cancer* **63**, 219-226, doi:10.1016/j.lungcan.2008.05.017 (2009).
- 29 Zavadil, J. & Bottinger, E. P. TGF-beta and epithelial-to-mesenchymal transitions. *Oncogene* **24**, 5764-5774, doi:10.1038/sj.onc.1208927 (2005).

- 30 Kang, J. H. *et al.* Aldehyde dehydrogenase is used by cancer cells for energy metabolism. *Exp Mol Med* **48**, e272, doi:10.1038/emm.2016.103 (2016).
- 31 Lee, J. S. *et al.* Dual targeting of glutaminase 1 and thymidylate synthase elicits death synergistically in NSCLC. *Cell Death Dis* **7**, e2511, doi:10.1038/cddis.2016.404 (2016).
- 32 Chuprin, A. *et al.* Cell fusion induced by ERVWE1 or measles virus causes cellular senescence. *Genes Dev* **27**, 2356-2366, doi:10.1101/gad.227512.113 (2013).
- 33 Li, J. *et al.* Inhibition of non-small cell lung cancer (NSCLC) growth by a novel small molecular inhibitor of EGFR. *Oncotarget* **6**, 6749-6761, doi:10.18632/oncotarget.3155 (2015).
- 34 Kim, J. J. *et al.* WSB1 overcomes oncogene-induced senescence by targeting ATM for degradation. *Cell Res* **27**, 274-293, doi:10.1038/cr.2016.148 (2017).
- 35 Mahale, J., Smagurauskaitė, G., Brown, K., Thomas, A. & Howells, L. M. The role of stromal fibroblasts in lung carcinogenesis: A target for chemoprevention? *Int J Cancer* **138**, 30-44, doi:10.1002/ijc.29447 (2016).
- 36 Sacco, O. *et al.* Epithelial cells and fibroblasts: structural repair and remodelling in the airways. *Paediatr Respir Rev* **5 Suppl A**, S35-40 (2004).
- 37 Sima, J. & Gilbert, D. M. Complex correlations: replication timing and mutational landscapes during cancer and genome evolution. *Curr Opin Genet Dev* **25**, 93-100, doi:10.1016/j.gde.2013.11.022 (2014).
- 38 Suzuki, M. *et al.* Late-replicating heterochromatin is characterized by decreased cytosine methylation in the human genome. *Genome Res* **21**, 1833-1840, doi:10.1101/gr.116509.110 (2011).
- 39 Suzuki, M. *et al.* Optimized design and data analysis of tag-based cytosine methylation assays. *Genome Biol* **11**, R36, doi:10.1186/gb-2010-11-4-r36 (2010).
- 40 Kan, Z. *et al.* Whole-genome sequencing identifies recurrent mutations in hepatocellular carcinoma. *Genome Res* **23**, 1422-1433, doi:10.1101/gr.154492.113 (2013).
- 41 Lawrence, M. S. *et al.* Mutational heterogeneity in cancer and the search for new cancer-associated genes. *Nature* **499**, 214-218, doi:10.1038/nature12213 (2013).
- 42 Lochovsky, L., Zhang, J., Fu, Y., Khurana, E. & Gerstein, M. LARVA: an integrative framework for large-scale analysis of recurrent variants in noncoding annotations. *Nucleic Acids Res* **43**, 8123-8134, doi:10.1093/nar/gkv803 (2015).
- 43 Manton, K. G., Woodbury, M. A. & Stallard, E. A variance components approach to categorical data models with heterogeneous cell populations: analysis of spatial gradients in lung cancer mortality rates in North Carolina counties. *Biometrics* **37**, 259-269 (1981).
- 44 Cameron, A. Regression-based tests for overdispersion in the Poisson model. *Journal of Econometrics* **46**, 347-364 (1990).
- 45 Lawrence, M. S. *et al.* Discovery and saturation analysis of cancer genes across 21 tumour types. *Nature* **505**, 495-501, doi:10.1038/nature12912 (2014).

- 46 Rheinbay, E. *et al.* Recurrent and functional regulatory mutations in breast cancer. *Nature* **547**, 55-60, doi:10.1038/nature22992 (2017).
- 47 Ernst, J. & Kellis, M. ChromHMM: automating chromatin-state discovery and characterization. *Nat Methods* **9**, 215-216, doi:10.1038/nmeth.1906 (2012).
- 48 Inoue, F. & Ahituv, N. Decoding enhancers using massively parallel reporter assays. *Genomics* **106**, 159-164, doi:10.1016/j.ygeno.2015.06.005 (2015).
- 49 Arnold, C. D. *et al.* Genome-wide quantitative enhancer activity maps identified by STARR-seq. *Science* **339**, 1074-1077, doi:10.1126/science.1232542 (2013).
- 50 Vanhille, L. *et al.* High-throughput and quantitative assessment of enhancer activity in mammals by CapStarr-seq. *Nat Commun* **6**, 6905, doi:10.1038/ncomms7905 (2015).
- 51 Li, H. & Durbin, R. Fast and accurate short read alignment with Burrows-Wheeler transform. *Bioinformatics* **25**, 1754-1760, doi:10.1093/bioinformatics/btp324 (2009).
- 52 Genomes Project, C. *et al.* A map of human genome variation from population-scale sequencing. *Nature* **467**, 1061-1073, doi:10.1038/nature09534 (2010).
- 53 Harmanci, A., Rozowsky, J. & Gerstein, M. MUSIC: identification of enriched regions in ChIP-Seq experiments using a mappability-corrected multiscale signal processing framework. *Genome Biol* **15**, 474, doi:10.1186/s13059-014-0474-3 (2014).
- 54 Rao, S. S. *et al.* A 3D map of the human genome at kilobase resolution reveals principles of chromatin looping. *Cell* **159**, 1665-1680, doi:10.1016/j.cell.2014.11.021 (2014).
- 55 Barutcu, A. R. *et al.* Chromatin interaction analysis reveals changes in small chromosome and telomere clustering between epithelial and breast cancer cells. *Genome Biol* **16**, 214, doi:10.1186/s13059-015-0768-0 (2015).
- 56 Ay, F., Bailey, T. L. & Noble, W. S. Statistical confidence estimation for Hi-C data reveals regulatory chromatin contacts. *Genome Res* **24**, 999-1011, doi:10.1101/gr.160374.113 (2014).
- 57 Cheng, C., Min, R. & Gerstein, M. TIP: a probabilistic method for identifying transcription factor target genes from ChIP-seq binding profiles. *Bioinformatics* **27**, 3221-3227, doi:10.1093/bioinformatics/btr552 (2011).
- 58 Hartigan, J. A. a. W., M. A. Algorithm AS 136: A K-Means Clustering Algorithm. *Journal of the Royal Statistical Society. Series C (Applied Statistics)* **28**, 100-108 (1979).
- 59 David M. Blei, A. Y. N., Michael I. Jordan. Latent Dirichlet Allocation. *The Journal of Machine Learning Research* **3**, 993-1022 (2003).
- 60 Zhu, M., Liu, C. C. & Cheng, C. REACTIN: regulatory activity inference of transcription factors underlying human diseases with application to breast cancer. *BMC Genomics* **14**, 504, doi:10.1186/1471-2164-14-504 (2013).
- 61 Pereira, B. *et al.* The somatic mutation profiles of 2,433 breast cancers refines their genomic and transcriptomic landscapes. *Nat Commun* **7**, 11479, doi:10.1038/ncomms11479 (2016).